Magnetization of HTS and design of marine current turbine generator

メタデータ	言語: eng 出版者: 公開日: 2017-10-25 キーワード (Ja): キーワード (En): 作成者: 李, 智 メールアドレス: 所属:
URL	https://oacis.repo.nii.ac.jp/records/1468

Doctoral Dissertation

MAGNETIZATION OF HTS AND DESIGN OF MARINE CURRENT TURBINE GENERATOR

September 2017

Graduate School of Marine Science and Technology
Tokyo University of Marine Science and Technology
Doctoral Course of Applied Marine Environmental Studies

LI ZHI

CONTENTS

ABSTRACT 4

CHAPTER I
General introduction to superconductivity 6
1.1 A brief history of superconductivity 6
1.2 The basic properties of superconductors 7
    1.2.1 Zero resistance characteristic 8
    1.2.2 Complete diamagnetism – Meissner Effect 8
1.3 Critical parameters 9
    1.3.1 Critical temperature T_c: the quest for higher values 9
    1.3.2 Critical magnetic field H_c 10
    1.3.3 Critical current density J_c 11
1.4 Classification of superconductors 12
    1.4.1 The Ginzburg-Landau phenomenological theory 12
    1.4.2 Type-I superconductor and magnetization 13
    1.4.3 Type-II superconductor and magnetization 14
1.5 Magnetic properties of HTS bulks 15
    1.5.1 Flux pinning 15
    1.5.2 The Bean model 17
    1.5.3 The Kim model 20
References 21

CHAPTER II
Off-axis field cooled magnetization of GdBCO bulk 22
2.1 Magnetization techniques 22
    2.1.1 Zero field cooled magnetization and field cooled magnetization 22
    2.1.2 Pulsed field magnetization 23
2.2 Crystallographic structure and anisotropies of REBCO bulk 26
2.3 Off-axis field cooled magnetization for disk-shaped GdBCO bulk 27
    2.3.1 Trapped field results 30
2.4 Off-axis field cooled magnetization for cubic GdBCO bulk 38
    2.4.1 Trapped field results 39
2.5 Discussions 41
References 47

CHAPTER III
Marine current energy 50
3.1 Marine current characteristics 50
3.2 Marine current turbine generators sites 51
    3.2.1 Japan sites 52
3.3 Theory review 53
    3.3.1 Betz’s Law and power coefficient 54
    3.3.2 Optimal tip speed ratio 59
3.4 Research and development of marine current turbine generators 60
References 63

CHAPTER IV

Electrical design of 1 MW HTS salient-pole marine current turbine generator........ 65
4.1 Conceptual structure of HTS salient-pole generator 65
4.2 Working conditions of marine current turbine generator 68
4.3 Design and optimization of electromagnetic model.. 68
4.4 Design results of HTS generator 84
4.5 Conclusions 85
References 85

CHAPTER V

Electrical design of 1 MW PM salient-pole marine current turbine generator.......... 88
5.1 Conceptual structure of PM salient-pole generator... 88
5.2 Working conditions of marine current turbine generator 89
5.3 Design and optimization of electromagnetic model.. 89
5.4 Design results of PM generator.. 97
5.5 Conclusions 100
References 100

CHAPTER VI

Conclusions and future work.. 101
6.1 Conclusions 101
6.2 Future work 102

Acknowledgements 104

List of publications 105

List of Abbreviations

HTS	High temperature superconductor
LTS	Low temperature superconductor
FCL	Fault current limiter
SMES	Superconducting magnetic energy storage
NMR	Nuclear magnetic resonance
ρ	Resistivity
R	Resistance
T	Temperature
T_c	Critical temperature
DC	Direct current
J_c	Critical current density
WCPM	Waveform control pulse magnetization
M	Magnetization
H	Magnetic field
H_c	Critical magnetic field
H_{c1}	Lower critical magnetic field
H_{c2}	Upper critical magnetic field
GdBCO	$GdBa_2Cu_3O_{7-\delta}$
REBCO	$REBa_2Cu_3O_{7-\delta}$ (RE = rare earth element or Y)
BSCCO	Bismuth strontium calcium copper oxide
BSCCO-2223	$Bi_2Sr_2Cu_2C_3O_x$
ZFC	Zero field cooled
FCM	Field cooled magnetization
PFM	Pulsed field magnetization
B_{app}	Applied external magnetic field
B_{trap}	Maximum trapped magnetic flux density
PM	Permanent magnet
MCTG	Marine current turbine generator
3D	Three dimensional
QMG® GdBCO	GdBCO bulk fabricated using quench melt growth method by Nippon Steel & Sumitomo Metal Corporation
R&D	Research and development

ABSTRACT

Limited by the magnetic saturation of permanent magnets or the huge Joule heat in copper excitation coils as magnetic field poles, it is evitable to employ high temperature superconductors (HTS) in future large-scale megawatt (MW) electric applications thanks to the superior trapped flux performance (HTS bulks) or current-carrying ability (HTS tapes). To prompt the research and development (R&D) progress of applied HTS technology, this dissertation concentrates on the design and improvement of HTS rotating applications, including a novel magnetization geometry for HTS bulks (Part I) and a prototype marine current generator with HTS tapes in field poles (Part II).

In part I, an off-axis field cooled magnetization geometry is proposed and the trapped flux behavior of $GdBa_2Cu_3O_{7-\delta}$ QMG® samples under off-axis field cooled magnetization is studied.

Thanks to type-II superconducting properties, the melt-growth $REBa_2Cu_3O_{7-\delta}$ (RE denotes rare earth element or Y) bulk is capable of trapping magnetic flux upon cooled below T_c. Coupled with finely distributed second phases like Gd_2BaCuO_5, the trapped magnetic flux has achieved 17.6 T at 26 K under field cooled magnetization. Such superior performance can dramatically increase the torque/power density of rotating machines, igniting the global research on HTS applications using $REBa_2Cu_3O_{7-\delta}$ bulks.

Till now, the majority of magnetization study applies external magnetic field parallel to the crystallographic *c*-axis of HTS bulks. There have been no targeted efforts to magnetize HTS bulks under an off-axis magnetic field with respect to the *c*-axis and the trapped flux behaviour under such magnetization geometry has not been reported. Here, off-axis field cooled magnetization is conducted and trapped flux performance is analyzed. It is found that within finite inclination angle up to 30° ~ 45°, the sample provides superior trapped flux component parallel to the *c*-axis comparable with those obtained by the conventional on-axis field cooled magnetization. Meanwhile, the magnetization is almost parallel to the B_{app}. For large inclination angle, trapped flux lines are meaningful to understand the pinning behaviour of bulk materials in which the trapped flux behaviour is a collection of anisotropic flux pinning and the effect of microstructure on the deformed circulation of supercurrent. The off-axis magnetization geometry makes it more flexible for the design of *in-situ* magnetization systems in HTS electric machines.

In large-scale power applications, a promising solution is to employ HTS technologies. In part II, the design for marine current turbine generator is proposed with a new conceptual structure fitting the marine current energy characteristics. Moreover, two generator topologies are studied and compared at this stage, i.e., conventional PM topology and HTS topology, for the magnetic field poles. Salient-pole marine current turbine generator with iron core of rotor and stator is adopted here considering cost-performance and weight.

Analytical model and 3D magnetic field study are combined to design and optimize a 1 MW salient-pole marine current turbine generator with the following main objectives:

1. Develop suitable electrical design methods for salient-pole HTS and PM marine current turbine generators.
2. Optimize main machine parameters based on their influence on the basic performance of marine current turbine generators.
3. For HTS topology, focus on the generator performance at 77 K considering the cooling easement of the cryogenic vessel used for HTS tapes.
4. Compare the performance of HTS and PM marine current turbine generators.

In Chapter IV, a conceptual structure of 1 MW HTS salient-pole marine current turbine generators are presented, and the electrical design method is proposed and its derivation is introduced in details. Based on the initial design, 3D simulation is implemented to calculate the magnetic flux distribution. Integrated magnetic flux in three core parts is emphasized, including the field pole part, armature part and stator part. Some main parameters including the pole pitch, the stator outer diameter, the magnetic flux density in the teeth, and the electric loading of 1 MW marine current turbine generators are optimized considering their effects on the basic generator performance. Here, 77 K is decided as the working temperature for HTS tapes considering the cooling system easement. The corresponding influence on the basic performance (the generator weight, efficiency, and the required HTS length) are studied. In addition, the maximum field current and the refrigerator power required at 77 K are determined. Based on the above calculation and simulation, a suitable structure of a cryogenic vessel used for HTS field coils is proposed and various heat losses in the different positions of the cryogenic vessel are calculated. Then, the required cooling power for the refrigerator is obtained, and its volume and flow rate are calculated. In the end, it is concluded that 77 K is a promising operating temperature for 1 MW marine current turbine generator.

In Chapter V, a conceptual structure of 1 MW PM salient-pole marine current turbine generator is presented, and the electrical design method is proposed and its derivation is introduced in details. The magnetic flux simulation for single pole of PM marine current turbine generator is also performed. The determination methods of two key parameters of the field leakage coefficient and the working condition of PM field poles are presented.

Lastly, in Chapter VI, the dissertation ends with conclusions of present results and discussions for the future work.

CHAPTER I

General introduction to superconductivity

Chapter I gives a brief introduction to superconductivity, including principal terminologies of superconductors, classifications of superconductors, magnetic properties and commonly used magnetization techniques. To lay a solid foundation for the following chapters, the magnetization behavior of Type-II superconductors is emphasized including the Bean model and the Kim's model.

1.1 A brief history of superconductivity

Superconductivity, a distinctive state in which electric current can flow “freely” without resistance, is regarded as is one of most attractive discoveries in the history of physics. In 1911, Heike Kamerlingh Onnes, a Dutch physicist of Leiden University, observed mercury lost resistance suddenly when the temperature dropped below the liquid helium temperature, 4.2 K, which was lately known as superconductivity. In 1933, German scientists W. Meissner and R. Ochsenfeld discovered that the magnetic flux completely disappeared from the interior of superconductors with zero resistance when cooled to 4.2 K in magnetic field. This zero-magnetic field inside a material became known as perfect diamagnetism and is now named as Meissner effect.

The 1980's were a decade of unrivaled discovery in the field of superconductivity. An inspiring breakthrough was made in the field of superconductivity at 1986. Alex Müller and Georg Bednorz, researchers at the IBM Research Laboratory in Rüschlikon, Switzerland, fabricated a brittle ceramic compound that exhibited superconductivity at unusual high temperature of 30 K. The lanthanum, barium, copper and oxygen compound that Müller and Bednorz synthesized, behaved in a not-as-yet-understood way. The discovery of this first of the superconducting copper-oxides (cuprates) won them a Nobel Prize the following year. The 'high' of high temperature superconductor (HTS) represents the ability to supeconduct using inexpensive liquid nitrogen, providing performance advantages that did not exist with low temperature superconductor (LTS), which is normally cooled by using liquid helium.

Since the discovery of superconductivity, two parallel approaches have been adopted to apply superconductors into engineering applications. One is from the material aspects: to understand the mechanism of superconductivity and improve the performance of superconducting materials. The other is from the engineering aspects: to design and manufacture possible applications based on the existing technologies and the understanding of material electromagnetic properties. In electrical engineering field, applied superconductivity technology is active in following applications as listed in Table 1-1.

Table 1-1. Classifications of the engineering applications with superconducting technology

Classifications	Applications/Components	Main Advantages
Power techniques	Transmission electrical cable	Low loss
	Fault current limiter (FCL),	Fast response
	Superconducting Magnetic Energy Storage (SMES)	High efficiency, fast response, improved rated power
	Transformer	High power density
	Current lead	High current density
	Motor & Generator	High efficiency, high power density
Magnet techniques	Particle and nuclear accelerator	High magnetic field
	Maglev train	Novelty, high speed
	Nuclear magnetic resonance (NMR)	High magnetic field
	Flywheel bearing	High power density, low loss

As can be seen from Table 1-1, engineering applications with superconducting technology mainly focus on superconducting power technology and superconducting magnet technology. Thanks to the large current-carrying ability (HTS tapes) or superior trapped flux performance (HTS bulks), it is possible to design and manufacture applications with advantages such as compact, higher power density, lower weight and higher apparatus capacity, etc. However, superconductivity only appears at cryo-temperatures, requiring stable cryogenic technology. The eventual widespread application of superconductivity technology to engineering applications will mainly depend on reliable cryo-cooling system.

1.2 The basic properties of superconductors

In past decades, enormous researchers have been focused on the properties of superconductors including zero resistance, the Meissner effect, the Josephson effect, *etc.* [1]. When it comes to the electric rotating applications like generators and motors, two characteristics of zero resistance and the Meissner effect attract more attention.

1.2.1 Zero resistance characteristic

The zero resistance characteristic of the superconductors refers to that resistance abruptly disappears at critical temperature, T_c. Under T_c, superconductor is able to transport direct current (DC) without Joule heat dissipations. If a closed loop is formed by a superconductor in which current is induced, the induced “persistent current” will show no obvious signs of decay for years. The upper limit of resistivity measured by the “persistent current” experiment is less than 10^{-27} Ω•m, while a good conventional conductor such as copper has a resistivity of 10^{-10} Ω•m at 4.2 K, which is more than 17 orders of magnitude than that of superconductors. A typically dependence of resistivity on temperature for superconductors and norm conductors is shown in Fig. 1-1. It is emphasized that superconductors lose DC resistivity at T_c.

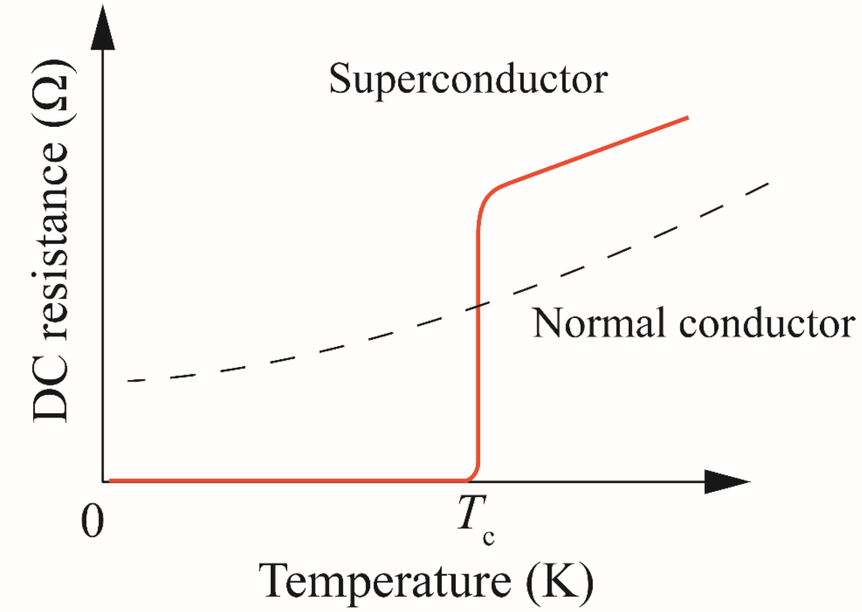

Figure 1-1. DC resistance variation as a function of temperature for superconductors and normal conductors.

1.2.2 Complete diamagnetism – Meissner Effect

In 1933, Meissner and Ochsenfeld found that below T_c, a superconductor placed in a weak external magnetic field (H) expels the magnetic field. The superconducting current at the surface of the superconductor opposes the penetration of the magnetic field. Notably, the magnetic induction (B) created in the superconductor is equal to 0 no matter the magnetic field is applied before or after the superconducting transition.

In other words, the Meissner Effect is regarded as perfect demagnetization [2]. When a superconductor under normal state is placed in an external magnetic field, the magnetic flux can totally penetrate the superconductor and the inner magnetic field is not zero as shown in Fig. 1-2 (a). While, in superconducting state, the magnetic flux will be expelled completely keeping the inner magnetic flux as zero. Namely, the superconductor is perfectly demagnetized as shown in Fig. 1-2 (b).

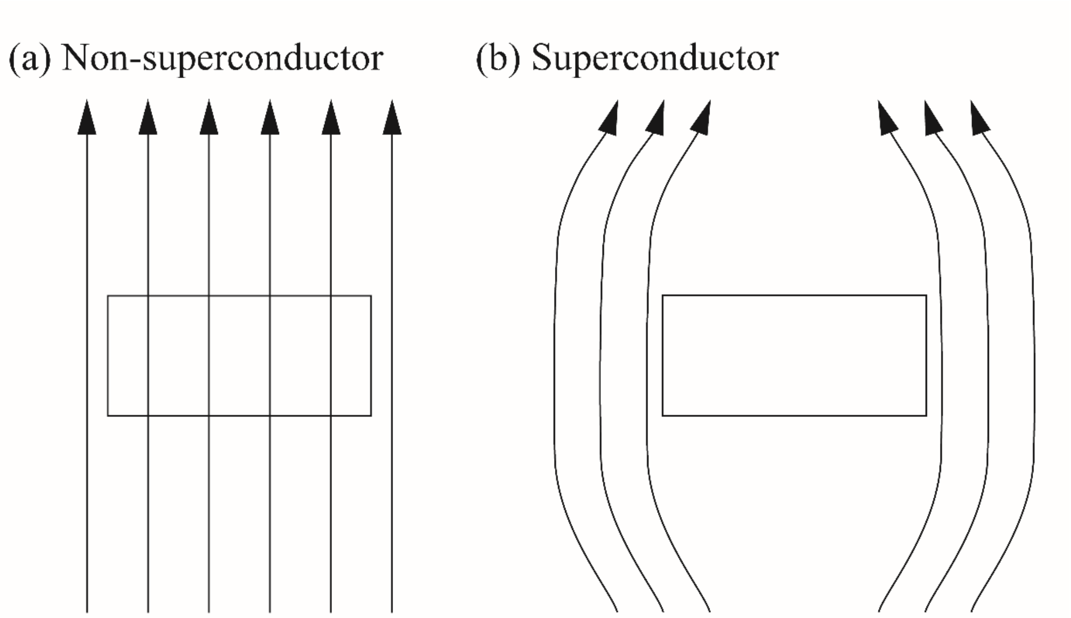

Figure 1-2. (a) When the superconductor is under normal state (or non-superconductors), the magnetic flux can totally penetrate the materials. (b) "Perfect diamagnetism": no magnetic flux within the inner of superconductors, independent of the history profile of an external magnetic field.

1.3 Critical parameters

In applied superconductivity, there are three principal critical parameters: the critical temperature T_c, the critical field H_c and the critical current density J_c.

1.3.1 Critical temperature T_c: the quest for higher values

The superconducting transition occurs in a temperature range near T_c, which is the temperature transition width ΔT_c. For HTS materials, especially, the typical value of ΔT_c is 0.5 K to 1 K, relating to the internal inhomogeneity, weak links, granularities and microscopic defects. Since the discovery of superconductivity in 1908, researchers have been pursing to find superconductors with higher T_c, which present limitations to the widespread of superconducting applications. Till now, the discovery of superconductors including elements and compounds are summarized in Fig. 1-3.

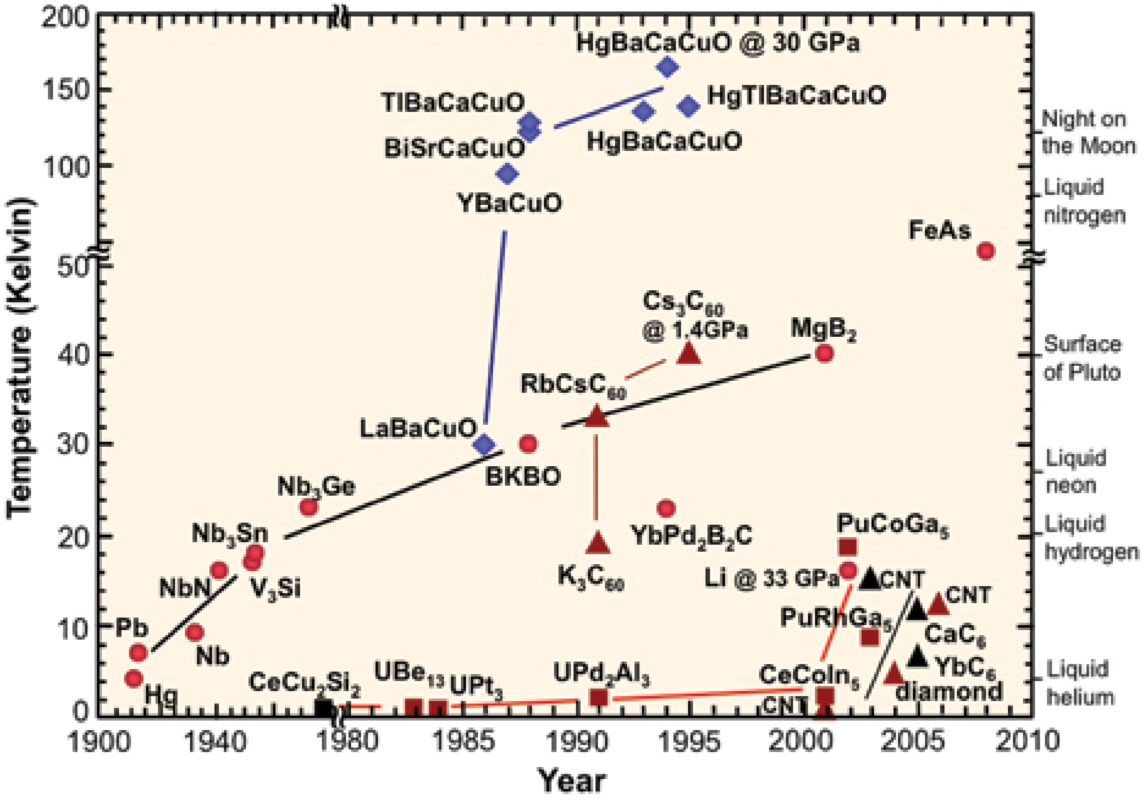

Figure 1-3. Critical temperature of superconductors versus year of discovery [3].

1.3.2 Critical magnetic field H_c

It is found that superconductors lose superconductivity when the external magnetic field exceeds a certain value, which is defined as the critical field H_c. For a specific superconductor, H_c is influenced by temperature and continuously increases with the decreasing of temperature. Like the critical temperature T_c, there is also a field transition width ΔH_c in the vicinity of H_c when the superconductor transforms from normal state to superconducting state. For a practical superconductor, there are usually two critical fields, namely the upper critical field H_{c2} and the lower critical field H_{c1}. When the magnetic field strength H is less than H_{c1}, the superconductor is in the Meissner state; when the H is higher than H_{c2}, the superconductor is in the normal state; while the field H is between H_{c1} and H_{c2}, the superconductor is in the mixed state. These properties will be discussed in more details in the next sections.

1.3.3 Critical current density J_c

Besides T_c and H_c, the magnitude of electric current also limits the performance of superconductors. Once the transport current exceeds a certain value, called the critical current I_c, superconductors will lose their superconductivity. For convenience, it is also popular to use current density J_c other than transport current I_c to describe the current carrying limitation. When the I_c increase, the transition of superconducting state to normal state does not happen suddenly. The critical current I_c refers to the maximum direct current that can flow without resistance and the criteria for this condition is normally chosen with the electric field strength E of 1 μV/cm. I_c and J_c continuously decreases with increasing of temperature T and the external magnetic field strength H.

The mentioned three critical parameters T_c, H_c and J_c show a strong interrelation among themselves. Figure 1-4 shows the useful (T, H, J) space of superconducting state for power applications [4]. Any point within the volume enclosed by the (T_c, H_c, J_c) surface and the T-H, T-J and H-J planes represents that the superconductor is in superconducting state; while, any point outside the volume represents that the superconductor transforms to the normal state, and any point on the curved (T_c, H_c, J_c) surface represents that the superconductor is at critical state.

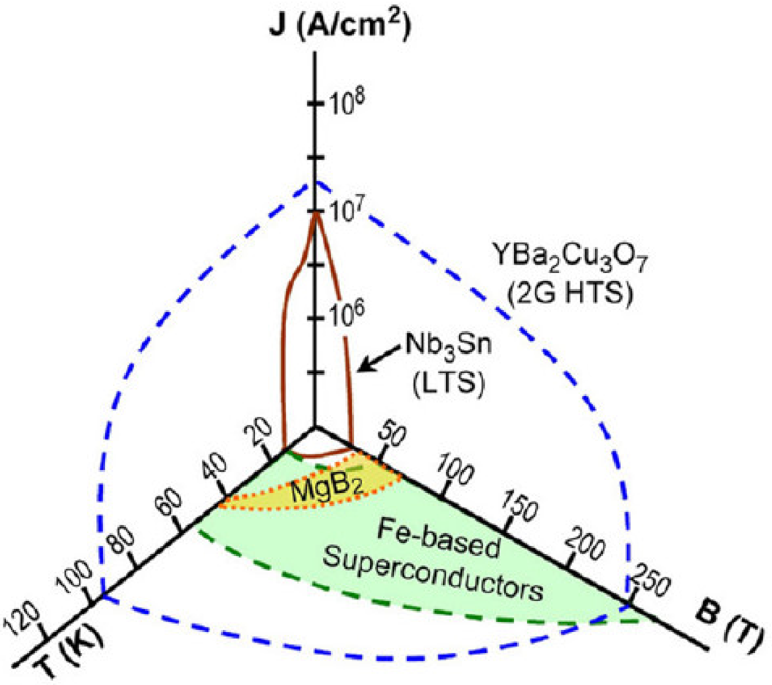

Figure 1-4. The superconducting and normal states of a superconductors, defined by the T_c, the H_c and the J_c [4].

1.4 Classification of superconductors

Superconductors can also be categorized as type I or type II superconductors depending on their response to the external magnetic field. In this study, the type II superconductors are emphasized.

1.4.1 The Ginzburg-Landau phenomenological theory

Below T_c, the superconducting state is more stable than the normal conducting state. The electron system can lower its free energy by forming Cooper pairs, which is in ordered state and known as a kind of Bose condensation. Specifically, the condensation energy can be described using the thermodynamic critical field H_c. In Meissner effect, the superconductor repels magnetic field completely, where excess energy is needed at H_c. Consequently, the condensation energy per unit volume is $G_n - G_s$ is given by from the view of Gibbs free energy $G(T, P, \mathrm{H})$, the change in free energy density of a conductor

$$G_n - G_s = \int_0^{H_c} M\,dH = \frac{1}{2}\mu_0 H_c^2 \qquad (1-1)$$

where G_s, G_n are the free energy of the superconducting state and the normal conducting state respectively, and μ_0 is the permeability of vacuum.

In 1950, Landau established Ginzburg-Landau (GL) theory after the London theory and Pippard theory. Lately, it was further developed by Abrikosov and Gor’kov. In GL theory, Landau argued that the transition from the normal conducting state to superconducting states occurred when the free energy of the superconducting phase drops below that of the normal state. He got enlightened from the fact that phase transition often depends on some order parameters. Together with Ginzburg, they proposed and introduced an order parameter $\boldsymbol{\psi}(\boldsymbol{r})$ based on the superconducting charge carrier number density n_p.

$$\int_{-\infty}^{\infty} \psi\psi^* dV = n_p \qquad (1-2)$$

where the superscript “*” indicates a complex conjugate. Meanwhile, the concept that the free energy might also depend on the derivative of $\boldsymbol{\psi}$ in space. Assuming the minimized free-energy, where α and β are functions of T, F_n is the normal state free energy, B_E is the externally applied field and ϵ is a constant,

$$F = F_n + \int_V \alpha\,\psi^*\psi + \frac{1}{2}\beta(\psi^*\psi)^2 + \epsilon\left|\nabla\psi - \frac{2e}{i\hbar}\boldsymbol{A\psi}\right|^2 dV + \int \frac{1}{2\mu_0}(B - B_E)^2 dV \quad (1-3)$$

with respect to small changes in $\boldsymbol{\psi}$ and the magnetic field the two G-L equations may be obtained. The first equation is an energy eigenvalue equation for the domain inside a superconductor:

$$\frac{1}{2m}(-i\hbar\nabla + 2e\boldsymbol{A})^2\boldsymbol{\psi} + (\alpha + \beta\psi\psi^*)\psi = 0$$

$$\frac{ie\hbar}{m}(\psi^*\nabla\psi - \psi\psi^*)^2\boldsymbol{\psi} - \frac{\boldsymbol{4e^2}}{\boldsymbol{m}}A\psi\psi^* = J_s \qquad (1-4)$$

Meanwhile, a boundary condition which confines the edges states of a superconductor:

$$-i\hbar\nabla\boldsymbol{\psi} + 2\mathrm{eA}\psi = 0 \qquad (1-5)$$

Solving equation (1-4) and (1-5), two characteristic lengths can be obtained. The G-L penetration depth, λ, is given by the following equation

$$\lambda = \sqrt{\frac{m\beta}{4\mu_0 e^2|\alpha|}} \qquad (1-6)$$

and the G-L penetration coherence length, ξ, by

$$\xi = \sqrt{\frac{\hbar^2}{2m|\alpha|}} \qquad (1-7)$$

By solving the G-L equations, Abrikosov noted that based on the values of the *G-L parameter*

$$\kappa = \frac{\lambda(T)}{\xi(T)} \qquad (1-8)$$

superconductors can be divided into two types.

1.4.2 Type-I superconductor and magnetization

When $\kappa < \frac{1}{\sqrt{2}}$, the surface interface energy of superconductor is positive and exhibits the Meissner effect. Such superconductor is classified as type I superconductors, which only has one critical magnetic field H_c. When $T < T_c$ and $H < H_c$, superconductor is in the Meissner state, namely it is perfect demagnetized under magnetic field and the induce B inside the superconductor is 0. Here, the magnitude of magnetization M is equal to magnetic field strength H and $M = -H$. When the external magnetic field increase to B_c (=$\mu_0 H_0$), the superconductor immediately turns into the normal state from the superconducting state, where H_c is a temperature dependent variant. Till now, except vanadium, niobium and technetium, all the discovered metal superconductors belong to type I superconductors. Caused by the low H_c, type I superconductors easily lose superconductivity. Also, the superconducting current merely flow on the thin layer of its surface with penetration depth λ at scale of 10^{-6} cm without superconducting current flowing through its entire body. Consequently, type I are treated with less practical meaning for high field applications.

1.4.3 Type-II superconductor and magnetization

When $\kappa > \frac{1}{\sqrt{2}}$, the surface interface energy becomes negative. Consequently, the largest normal-superconducting boundary will appear to satisfy the lowest energy state for the superconducting state. The equilibrium state consists of large number of filaments each containing one quantum flux with value of $\Phi_0 = \frac{h}{2e}$. Such materials are regarded as type II superconductors.

In type-II superconductors, the Meissner effect occurs up to the lower critical field H_{c1} and magnetic flux begins to penetrates into superconductors up to the higher critical field H_{c2} in the form of flux lines (or flux vortices) screened by induced supercurrents. With the increasing of magnetic field strength, the cores of quantum flux become overlapped and the superconductor loses its superconductors and transits to normal state at field above H_{c2}. Type II superconductors are classified into two categories: ideal Type II superconductor and non-ideal Type II superconductors [5].

1.4.3.1 Ideal Type-II Superconductor

One of the difference between type-I and type-II superconductor is that type-II superconductor possess two critical magnetic field H_{c1} and H_{c2} which are both temperature dependent. When external magnetic field strength $H<H_{c1}$, the superconductor is in the Meissner state. When $H_{c1}<H<H_{c2}$, the superconducting state and normal state coexist, which is known as a mixed state, allowing the magnetic flux penetrate the normal region of superconductors.

1.4.3.2 Non-ideal Type-II Superconductor

The non-ideal type II superconductor, also known as “dirty” superconductor, shares some similar characteristics with ideal type-II superconductors, such as both have two critical magnetic fields and possess a mixed state. Whereas, the magnetization curve of non-ideal type II superconductor is irreversible and it can trap or pin magnetic flux with remnant magnetism characteristics. When the external magnetic field is below Hc1, it remains in Meissner state with perfect diamagnetism. Simultaneously, the $M = -H$. With the increasing of H to the range of $H_{c1} < H < H_{c2}$, the superconductors will be in the mixed state and the magnetic flux can penetrate the superconductor.

The non-linear B-H curve is irreversible. When the external magnetic field strength H continuously increase until $H > H_{c2}$, the superconductor loses superconductivity and recover to norm state.

1.5 Magnetic properties of HTS bulks

Since the discovery of HTS materials in 1986, which enables the possibility of superconducting materials working under the boiling point of liquid nitrogen (77 K), studies on such materials have attracted a lot of attention.

Generally, there are mainly three forms of HTS materials, including films, wires and bulks. The focus of this study is HTS bulks. Most of the well-known HTS materials are complex metal-oxide cuprates. They belong to the type II superconductors and are characterized by CuO_2 layers in their crystal structures [6]. In the most widely studied HTS material, GdBCO, the main elements that comprise this particular superconductor can be represented in the form $GdBa_2Cu_3O_{7-\delta}$. The whole set of materials in this family are usually referred to as the REBaCuO (RE = rare earth element or Y) system.

1.5.1 Flux pinning

The trapped field in the bulk HTS due to flux pinning, achieved by introduction of pinning centres into the sample, such as Gd-211 phase [7]. The basic and classical models used to estimate the trapped field for a specific sample will be also covered, such as Bean's model and Kim's model. It's notable that the present modelling only focus on the magnetization properties when the applied magnetic field is parallel to the crystallographic *c*-axis, which inspires the present off-axis field cool magnetization.

With a magnetic field "trapped" or "pinned" in a bulk superconductor via an appropriate magnetization method, bulks can work as "permanent magnets". However, in order to trap high magnetic flux, the introduction of inhomogeneities and defects into their microstructure is of utmost important to work as pinning centre to pin magnetic flux lines. Without the contribution of flux pinning centres, when the external applied field is above H_{c1}, the material enters its mixed state and the flux lines are free to move freely throughout the interior of the sample. Finally, they will be uniformly distributed into a particular lattice, called a regular Abrikosov lattice. Based on Bean's model, which will be fully discussed in

Section 1.5.2, the uniform distribution of trapped field corresponds to a zero-magnetic field gradient. This means that no current ($J = 0$) would flow in the bulk of superconductor, which is just confined in the surface. During the removal of the external applied field, these unpinned flux lines are now free to escape from the sample. Considering that no superconducting current flows within the sample during the magnetisation process, and no flux lines remain, there would be no remnant magnetic field left behind. On the other hand, if the pinning centres are introduced during the fabrication process, these impurities and other kind of inhomogeneities would pin the flux lines during the magnetisation, and a certain gradient of field distribution will be established ($J \neq 0$).

Consequently, after the removal of the externally applied field, a portion of the entire eddy currents would reverse, and thus the sample is effectively magnetized [8]. However, when the magnitude of external applied field exceeds a certain value, which is referred to as the 'irreversibility field', the pinning centres cannot work effectively anymore and the flux lines are able to release themselves from the pinning centres and are free to move again. The motion of a flux line is driven by the Lorentz force, F_L, which can be expressed by the following equation [9]:

$$F_L \propto J \times B \tag{1-9}$$

As the externally applied field increases, the corresponding Lorentz force also increases accordingly. When the Lorentz force exceeds the pining force F_{Pin}, magnetic flux won't be pinned anymore and will flow. As a result, the magnetization of the material is irreversible. As the name 'irreversibility field', suggests, when the applied field is over this point, the materials will transfer from an "irreversible" state to a "reversible" state.

A comparison of typical irreversible and reversible magnetization *M-H* curves is shown in Fig. 1-5, where the reversible part of the magnetization is illustrated as a thin line in Fig. 1-5 (b). When sample is in the Meissner state ($H_a < H_{c1}$), a superconducting current will be induced on the surface, which screens the externally applied field. Therefore, the magnetic field inside of the sample is zero regardless of the existence of pinning centres. Without the introduction of pinning centres, when the superconductor enters into mixed state between H_{c1} and H_{c2}, the size of the superconducting region shrinks due to more flux lines penetrating into the sample. Hence, the *M-H* loop of a defect-free sample is reversible, and after the external applied field decreases to zero, no magnetic field is trapped within the material. In the case of impurities within the HTS material, such as precipitates and non-magnetic oxides, which interact with the penetrating flux lines, the *M-H* curve is highly irreversible, as shown in Fig. 1-5 (b). Therefore, when $H_a > H_{c1}$, the flux lines cannot penetrate into the sample freely and concentrate at the surface. Meanwhile, M continues to decrease until the external field approaches to a certain magnitude, which is when the first flux line just reaches to the center of HTS sample (also covered in Bean's model). At $H = H_p$, the magnetization has its maximum diamagnetic value. However, with a continued increase of external field, the number of flux lines immobilized by pinning centres reaches its full capability and the field at the centre will increase from zero to the same value of the external applied field. Therefore, the field gradient drops in return. M starts to increase accordingly. During the process of decreasing the applied field from H_{irr} to zero, the pinning centres will still hinder the movement of the flux lines out of the material, and M continues increasing to positive values. Thus, a field is trapped within the sample. The gradient of the field profile is determined by the critical current density of the specific material, based on Bean's model. Therefore, the difference between two segments of the bold curve in Fig. 1-5 at a specific field H can be used to estimate the current density.

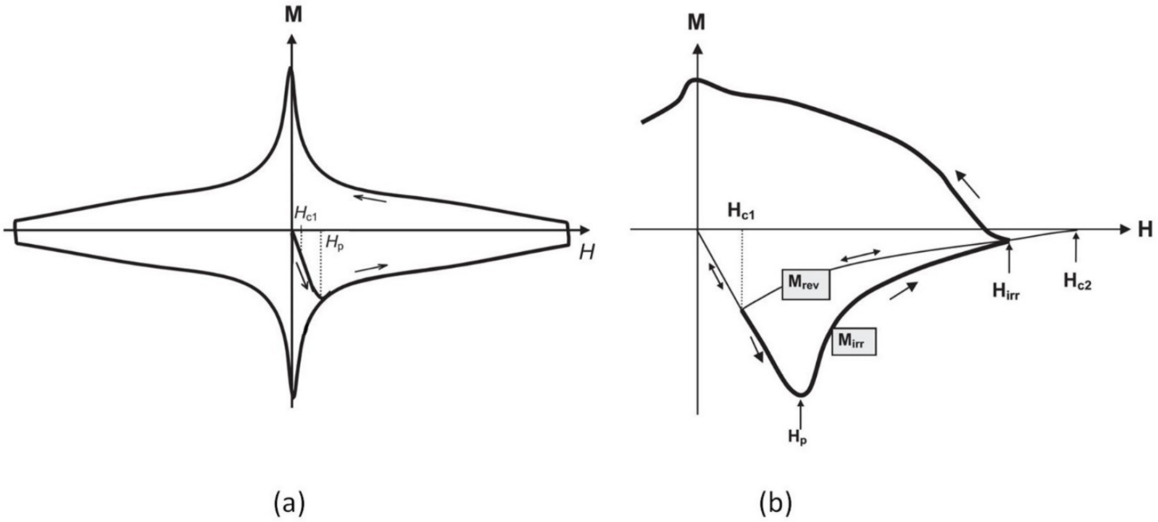

(a)

(b)

Figure 1-5. Summary of irreversible and reversible *M-H* curves of bulk HTS materials. (a) full magnetisation loop, (b) partial magnetisation curve [8].

1.5.2 The Bean model

Since 1962, the Bean model has been proposed and modified by C. P. Bean [10,11], with the purpose of giving a macroscopic explanation of the irreversible magnetisation behaviour of hard type-II superconductors. There are several underlying assumptions for the scope of Bean's model:

a) the relative permeability of type II superconductor, μ_r, is 1 in the mixed state;

b) any electromotive force in the region penetrated by external flux lines, however small, will induce the critical current, J_c, to flow in the superconductor and the current remains zero in the area without penetration;

c) there is no field dependence of the critical current density. In other words, with the sample in its mixed state, where the flux lines penetrate $J = J_c$ (J_c is the critical current density, over which the material will transfer from its superconducting sate to normal state);

d) in the areas of the sample without external field penetration, the current is $J = 0$.

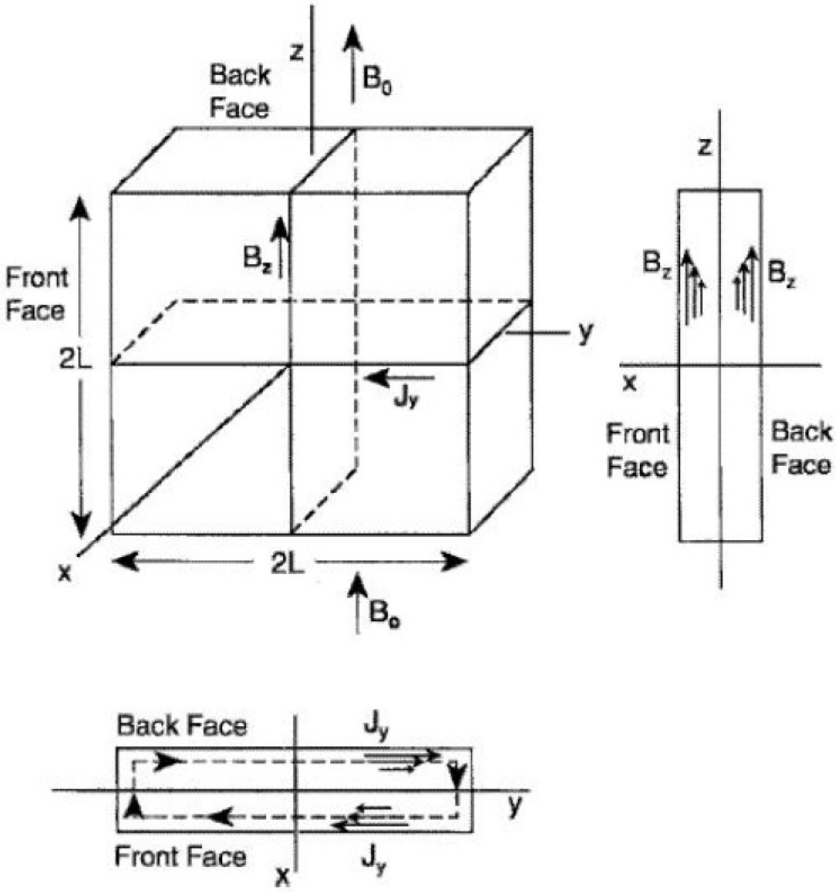

Figure 1-6. Illustration of the Bean model in a thin HTS slab with infinite length in the y-z plane [4].

Based on Ampere's law and the above assumptions, the magnetisation can be described by equation:

$$\nabla \times \boldsymbol{B} = \mu_0 J_c \qquad (1-9)$$

Bean's model is based on the geometry of a thin HTS slab of width 2L oriented in the y-z plane with its plane parallel to the uniform external field, B_0, increased from zero as shown in Fig. 1-6. An induced eddy current flows over the slab in the direction illustrated. Since it is assumed that only currents flowing along the y-axis are considered, which generates a magnetic field only along the *z*-axis, *B* now is simplified as a one-dimensional field gradient as described by equation:

$$\nabla\times\boldsymbol{B} = -\frac{\partial B}{\partial x}\boldsymbol{j} = \mu_0 J_c \qquad (1-10)$$

By integrating this equation, the value of the magnetic field can be calculated numerically. In particular, the characteristic field, B_p, which is also defined as the full penetration field, can be calculated by the following equation:

$$\boldsymbol{B_p} = \mu_0 J_c a \qquad (1-11)$$

where μ_0 is the permeability of free space, a is the half-width of the slab, and J_c is the critical current density of the material.

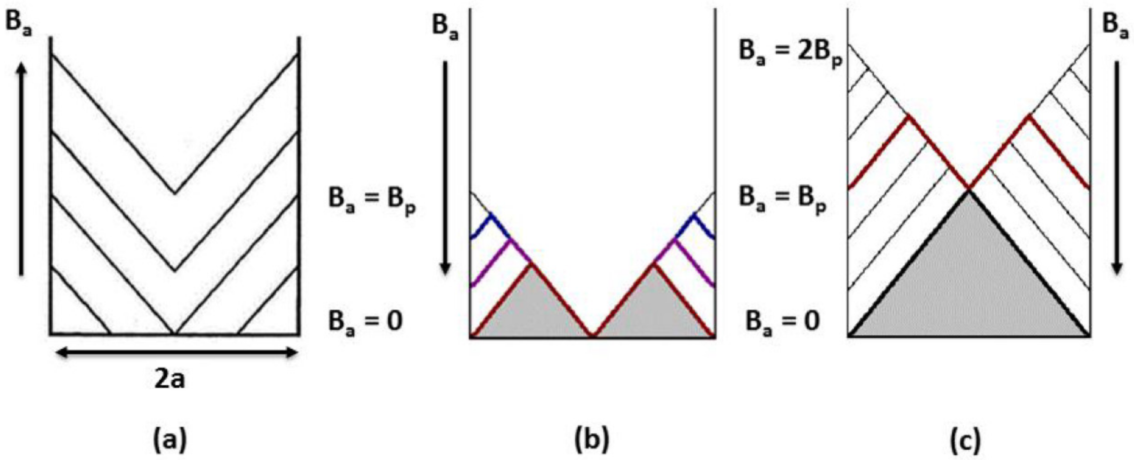

Figure 1-7. Distribution of the magnetic fields across the width of a slab during the application and removal of a slowly varying, external magnetic field.

Fig. 1-7 (a) shows the response of type-II superconductor for the application of a slowly varying external magnetic field increased from 0 to $2B_p$, without the pre-existence of any magnetic field, and the field distribution during the removal of external applied field. When the magnetisation field increases from 0 to B_p, the flux lines penetrate the sample from the edge to the centre with a constant gradient, which means that current flows over the penetrated area with a constant value, J_c. During the removal of B_a, if the bulk sample is not fully penetrated ($B_a < 2B_p$, as shown in Fig. 1-7 (b)), the trapped field in the sample has two peaks. Whereas if the sample is magnetized with an external field equal to or greater than $2B_p$, the trapped field has one clearly defined peak, as shown in Fig. 1-7 (c). In conclusion, the Bean model implies that the maximum trapped field is obtained with an external magnetic field of at least twice its characteristic value ($B_a \geq 2B_p$). The Bean model is the simplest way to provide a straightforward picture of the magnetic response of an HTS material during its magnetisation process based on several relatively simple assumptions.

1.5.2.1 Bean’s model applied to superconductors of finite thickness

The analysis of field distributions across the width of a HTS slab with infinite geometry can be equally applied to the cross-section of a cylindrical bulk sample of finite thickness; however, a correction factor is required to account for this finite thickness. The peak trapped field value is given by the following equation:

$$B_{\text{trapped}} = k\mu_0 J_c a \qquad (1-12)$$

where B_{trapped} is the trapped field calculated at the centre of the top surface of a single-grain bulk superconductor. *k* can be modified with the application of the Biot-Savart law as [15]:

$$k = \frac{t}{2a} ln\left(\frac{a}{t} + \sqrt{1 + \left(\frac{a}{t}\right)^2}\right) \qquad (1-13)$$

The analytical field distribution above the bulk sample along the *c*-axis can be derived from the following equation [12]. In the next equation, *a* and *t* are the radius and thickness of the bulk sample, respectively.

$$B_z(z) = \frac{1}{2}\mu_0 J_c \left\{(z+t)ln\left(\frac{a + \sqrt{a^2 + (z+t)^2}}{z+t}\right) - zln\left(\frac{a + \sqrt{a^2 + z^2}}{z}\right)\right\} \qquad (1-14)$$

where z is the elevation from the centre of superconductor's top surface.

1.5.3 The Kim model

With appropriate assumptions, the Bean model can effectively estimate the response of a type-II material in its mixed state. However, some of these assumptions are limited in practical cases. For instance, J_c is assumed as constant and independent of any externally applied field. Based on experimental results, the superconducting state is defined by three parameters: T_c, H_c and J_c, as shown in Fig. 1.2, and J_c is actually a function of *T* and *H*. Inspired by the Bean model, the Kim model was extended by Kim, Hempstead and Strnad in 1962 [13], and is summarized as equation (1.8) to include the in-field dependence of J_c.

$$J_c = \frac{J_{c0}}{1 + \frac{B}{B_0}} \qquad (1-15)$$

where J_{c0} represents critical current density without an external applied field, i.e., $B_a = 0$ T, and B_0 is the magnetic field when J_c reduces to half of J_{c0}. J_{c0} and B_0 are constant values and sensitive to the microstructure of the material and ambient temperature. The performance of a superconducting material is sensitive to ambient temperature change, so the Kim model can be modified with temperature considerations, shown as:

$$J_c(B,T) = \frac{J_{c0}(T)}{\left(1 + \frac{B}{B_0}\right)^{\beta}} \qquad (1-16)$$

Here, the ambient temperature is defined by T and β is a material-dependent constant that can vary with temperature.

The Bean model makes a simplifying assumption about the way of magnetic penetration, which qualitatively agrees well with the experimental observations. However, it cannot explain that with an increase of the sample size, the maximum trapped field cannot increase infinitely. In addition, it cannot give a good explanation for the trapped flux when the applied magnetic field is not parallel to the *c*-axis, which is the main target of the following study.

References

[1] F. Lodon, and H. London, *Proceedings of the Royal Society of London*, **1935**, A149, 71-88.

[2] W. Meissner and R. Ochsenfeld, *Naturwissenschaften*, **1933**, 21, 787-788.

[3] “Properties, History, and Challenges”, [Online] Available from: http://www.ccas-web.org/superconductivity/, Last accessed: **2017/08/06**.

[4] D. Wei, 'Solid State Physics (2nd ed.)' **2007** Tsinghua University Press.

[5] “Superconductivity”, R.D. Parks, **1969**, Volume 1.

[6] C. P. Poole, “Superconductivity, 2nd”, **2007** Elsevier Ltd 23.

[7] A.-M. Hu, C.-X. Xu C, M. Izumi, I. Hirabayshi, M. Ichihara, *Appl. Phys. Lett.* **2006**, 89**,** 192508.

[8] G. Krabbes, G. Fuchs, W. R. Canders, H. May and R. Palka “High Temperature Superconductors Bulk Materials”, **2006** Wiley-VCH Verlag GmbH & Co. KGaA.

[9] C. Oatley, “Electric and Magnetic Fields: An Introduction”, **1981**, Cambridge University Press.

[10] C. P. Bean, *Phys. Rev. Lett.* **1962**, 8, 250.

[11] C. P. Bean “Magnetisation of high-field superconductors”, *Rev. Mod. Phys.*, **1964**, 36.

[12] M. D. Ainslie and H. Fujishiro, “Modelling of bulk superconductor magnetisation”, *Supercond. Sci. Technol.*, **2015**, 28 053002

[13] Y. B. Kim, C. F. Hempstead, and A. R. Strnad, “Critical persistent currents in hard superconductors”, *Phys. Rev. Lett.*, **1963**, vol. 9, no. 7, pp. 306–309.

CHAPTER II

Off-axis field cooled magnetization of GdBCO bulk

To supply the superior magnetic flux source, HTS bulks must be magnetized upon external magnetic field. In this chapter, popular magnetization techniques to magnetize HTS bulks are introduced including zero field cooled (ZFC) magnetization, field cooled magnetization (FCM) and pulsed field magnetization (PFM). Meanwhile, recent attractive progress in PFM techniques is emphasized. Then, a novel magnetization geometry, off-axis field cooled magnetization, is studied for disk-shaped and cubic $GdBa_2Cu_3O_{7-\delta}$ (GdBCO) samples and the trapped flux behavior is analyzed.

2.1 Magnetization techniques

2.1.1 Zero field cooled magnetization and field cooled magnetization

For the measurement of trapped magnetic flux performance of HTS bulks, ZFC magnetization and FCM are commonly used, with the main difference in the sequence of cooling and the application of external magnetic field. In ZFC, the bulk is cooled below its T_c prior to excitation with an external magnetic field. In FCM, the bulk is placed under the external magnetic field B_{app} before cooling below T_c.

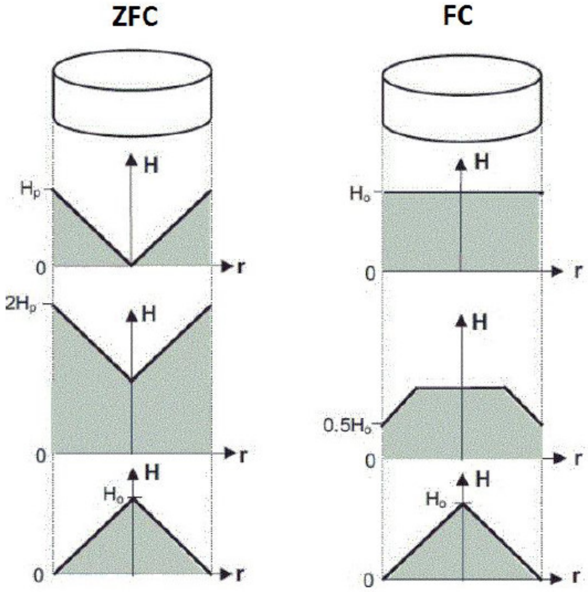

Figure 2-1. Comparison of zero field cooled (ZFC) and field cooled (FC) magnetization techniques for bulk superconductor using the Bean model [1]. In ZFC, to fully magnetize the HTS bulk at magnetic field strength H_0, at least $2H_0$ should be applied. While, in FC, only H_0 is needed.

In HTS applications, the required B_{app} should be confirmed including the waveform, magnitude, etc. As shown in Fig. 2-1, to achieve the maximum trapped magnetic flux B_{trap}, the external magnetic field should be applied at least twice of B_{trap} in ZFC and the same of B_{trap} in FC based on the Bean model. As mentioned in Chapter I, Bean model is set up based on several assumptions limiting its accuracy. Ongoing researches in PFM has indicated the limitations of Bean model in practical applicability. The recent related researches are introduced in the following parts.

2.1.2 Pulsed field magnetization

In ZFC and FC magnetization, large magnetizing coils and long magnetization time are needed which are impractical for most HTS electric applications. Another magnetization method, PFM has been developed and studied.

In 1996, Y. Itoh et al. first reported results of PFM applied to some YBCO large single grain samples [2]. The PFM technique is similar to ZFC, except that magnetic field is applied via a pulse/multi pulses on the order of milliseconds, rather than ramped up and down slowly over a period of many minutes or even hours. Consequently, a smaller and more compact magnetization fixture can be employed and the time scale for the magnetization process is much shorter. Several groups have successfully employed HTS bulks and pulse magnetization technology into electric applications such as Tokyo University of Marine Science and Technology as shown in Fig. 2-2.

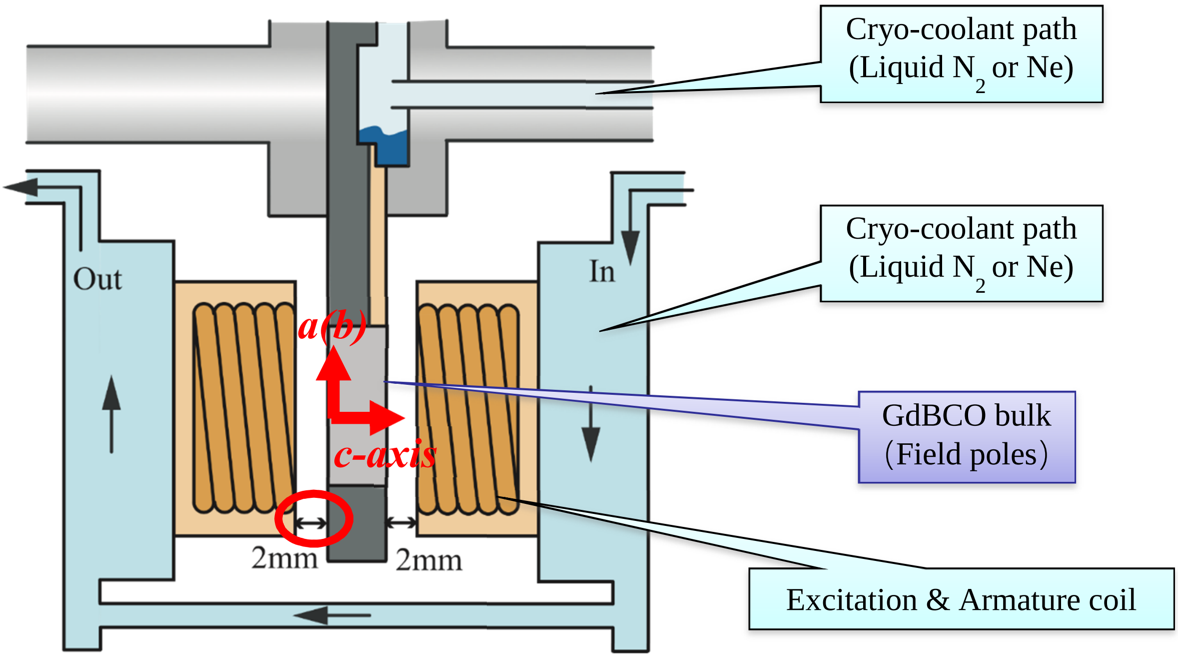

Figure 2-2. Inner structure of axial-gap synchronous generator with HTS bulks. The generated magnetization field by excitation coils is parallel to the crystallographic *c*-axis (@TUMSAT).

Two key techniques for the *in-situ* magnetization of HTS bulks are the suitable arrangement of HTS bulks and magnetizing coils in limited space and the elimination of the heat generation during magnetization to achieve higher trapped flux density. As shown in Fig. 2-2, magnetizing coils are arranged close to the HTS bulk surface at the level of 2 mm. Suitable cryo-coolant path should be designed for both HTS bulks and magnetization coils. It is notable that the external magnetic field is parallel to the crystallographic *c*-axis of the HTS bulk. On the other hand, due to the large temperature rise associated with the rapid dynamic movement of external magnetic flux into the sample during the PFM process, a significant amount of heating is generated within the superconductor, resulting in a large decrease in J_c, and thus a lower trapped field [3]. Therefore, the trapped field with PFM is generally much smaller than that of FC magnetization. To achieve an optimum trapped field profile for PFM, it is crucial to understand the flux movement within a bulk sample during this magnetisation process. In the study of PFM, there are many considerations and parameters to modify the trapped field profile in the sample, including the pulse magnitude, shape and duration, the numbers of pulses, the temperature rises during the process and the type of magnetisation coils (solenoid, split or vortex coils) [4].

Another interesting phenomenon is named as “flux jump” which is closely related to the heat generation during the penetration of magnetic flux into the bulks. As reported in [4] and shown in Fig. 2-3, the bulk is fully magnetized at 4.86 T and 51 K. Namely, the HTS bulk can be also fully magnetized using PFM techniques without the twice magnitude of maximum trapped flux for external field as indicated by Bean model. This can be explained, during the magnetic flux penetration, that the local heat degrades the local J_c resulting a small shielding current to resist the magnetic flux penetration. At specific applied magnetic field, the magnetic flux is relatively easy to penetrate the whole sample. However, the mentioned specific magnetic field varied with the quality of the HTS bulks. To take advantage of such mechanism into HTS electric applications, the required minimum applied magnetic field should be confirmed prior to the assembling of HTS electric applications, which would take plenty of time.

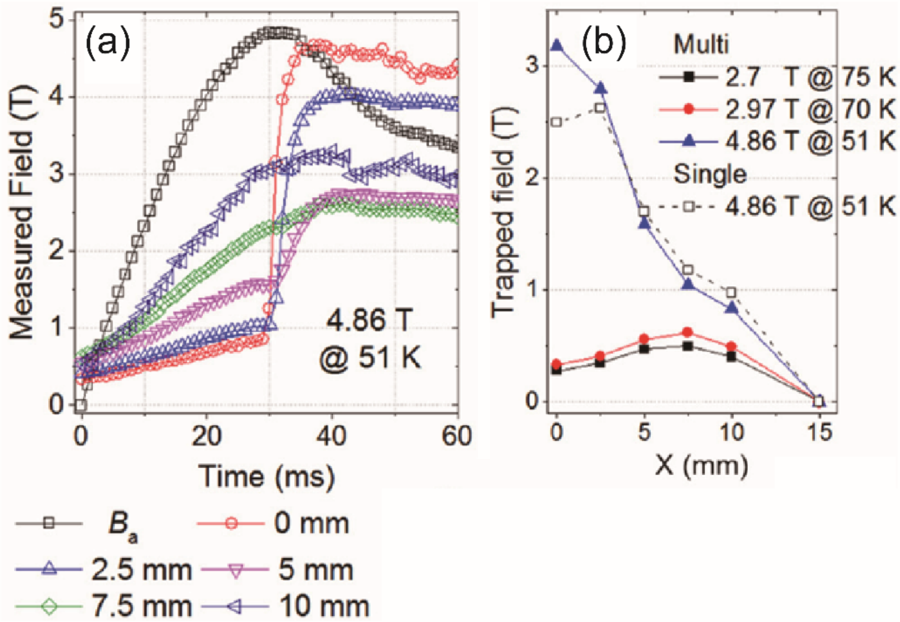

Figure 2-3. (a) Magnetic fields measured dynamically at the top surface of the GdBCO bulk sample during the rise of the final pulse at 51 K with B_{app} of 4.86 T. (b) Comparison of the trapped field profiles achieved from single and multi-step (multi-pulse, multi-temperature) PFM processes (2.7 T @ 75 K → 2.97 T @ 70 K → 4.86 T @ 51 K). Partial magnetization of the sample is achieved at the pre-magnetization stage. [4]

Recently, waveform control pulse magnetization (WCPM) is also reported to be able to magnetize the HTS sample effectively [3]. Using WCPM, it is possible to generate any pulsed magnetic field waveform by appropriately changing the duty ratio of the pulse width modulation. Through chopping, it is able to apply the pulsed magnetic field with time period at 1 millsecond level, making it possible to control the rise time of the pulse. Consequently, the magnetic flux motion can be suppressed, increasing the efficiency of magnetization. It is reported that, at 77 K, a GdBCO sample with 45 mm diameter and 19 mm thickness can trap a magnetic field of 1.63 T using PFM, which is more than 90% of that by FC magnetization.

Combing the study of [4] and [3], it can be concluded that effective magnetization of HTS bulks can be achieved in PFM. Thus, PFM can provide a promising solution for HTS applications using bulks. It is notable that WCPM method shows superiorities and is practical important and promising for electric applications. Compared with the passive magnetization method as used in [4], WCPM enables to magnetize the HTS bulks with similar performance achieved in FC magnetization. Considering the required small magnetization coils, it would further improve the power density of HTS applications and would be a better choice for applications.

2.2 Crystallographic structure and anisotropies of REBCO bulk

Before staring the study for off-axis FCM, a brief introduction of the crystal structure of $REBa_2Cu_3O_{7-\delta}$ (REBCO, where RE = rare earth element or Y) concerning the crystal anisotropies is given here.

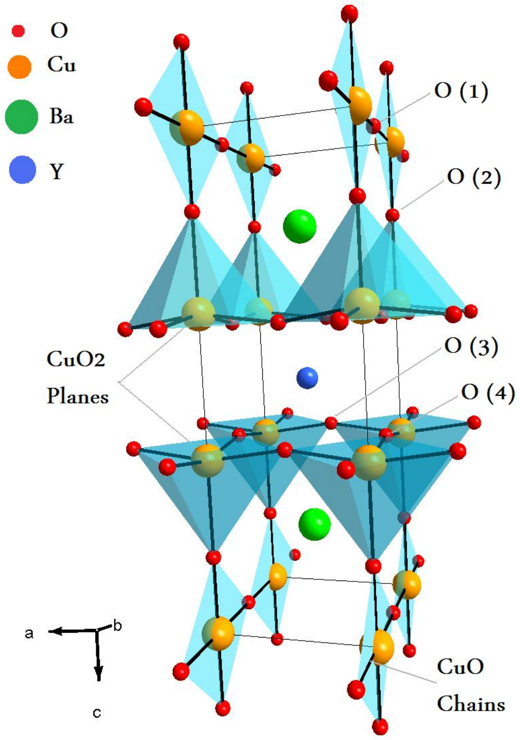

Figure 2-4. Hypoxia perovskite structure of an $YBa_2Cu_3O_7$ cell [5]

It can be seen from Fig. 2-4 that the REBCO type bulk material is a layered oxygen deficient perovskite structure, since the oxygen atoms at the top and bottom faces O(1) is prone to lose. With further losing of oxygen atoms, the formula changes to $YBa_2Cu_3O_{7-\delta}$. Meanwhile, a change of orthogonal (a ≠ b) to tetragonal (a = b) structure occurs when oxygen atom decrease to 6. It has the highest T_c when δ is 0.07, and becomes insulator when δ is larger than 0.6. Consequently, the anisotropic crystal structure results in anisotropic characteristics for REBCO family. The main anisotropies are summarized in Table 2-1. The influence by the anisotropies on the trapped flux behavior will be studied in the following parts.

Table 2-1. Main superconducting parameters anisotropies of GdBCO crystals.

Superconducting parameters	in the *a*-*b* plane	along the *c*-axis	Ratio $P_{a\text{-}b} / P_c$
Magnetic penetration depth (λ)	130 ~ 180 nm	500 ~ 800 nm	~ 0.25
Coherence length (ξ)	1.2 ~ 1.6 nm	0.15 ~ 0.3 nm	~ 6
Lower critical field (H_{c1})	50 ~ 70 mT	230 ~ 310 mT	~ 0.2

2.3 Off-axis field cooled magnetization for disk-shaped GdBCO bulk

The effective immobilization of magnetic flux is an important issue in power applications using high-temperature superconductor bulk cryomagnets as sources of superior magnetic fields. To achieve this, attention has turned to the trapped flux performance of large single-grain GdBCO. Till now, most magnetization studies focused on the magnetization along the crystallographic *c*-axis. Here, a novel magnetization approach at liquid nitrogen temperature is described that uses an external magnetic field B_{app} that is not parallel to the crystallographic *c*-axis normal to the Cu-O planes, i.e., an off-axis geometry. The results show that the trapped flux is almost polarized along the applied field as expected. This tendency remains up to a high off-axis angle θ around 60°. It is worth mentioning that, with θ of 30°, the maximum trapped flux component $B_{//\mathrm{max}}$ parallel to the *c*-axis significantly remains more than 96 % of 1.6 T which occurs under on-axis magnetization. Meanwhile, the angular dependence of the *c*-axis parallel component exhibits that observed flux density is higher than that expected value from $1.6\cos\theta$. In addition, to visualize the flux line upon magnetization at θ of 90°, we successfully demonstrate the continuous flux line trace using steel wires; different trapped flux behaviour appears when applied field penetrates the bulk through the growth sectors centre and along the growth sector boundary, respectively. We interpret these results may come from the microstructure as a result of melt growth. It is highly emphasized that the off-axis magnetization with the finite inclination angle is quite useful to be introduced into the design of HTS applications.

HTS REBCO bulk cryomagnets sustain an extremely high magnetic flux density magnetized below the superconductivity critical temperature, T_{c}, making them attractive for power applications. The magnetic flux trapping potential of this functional ceramic cryomagnet has been reported as 17 T at 29 K, 11 T at 47 K, and 3 T at the temperature of liquid nitrogen, using a cooling process under FCM [6-8]. In these cases, the external magnetic field B_{app} was applied normal to the Cu-O plane, which is parallel to the crystallographic *c*-axis of the REBCO bulk. With this superior feature, various prototype HTS machines and components using bulk cryomagnets have been designed and manufactured, including superconducting bearings, reluctance motors, and synchronous rotating machines [9-12]. The high magnetic flux density provided by HTS cryomagnets, which is superior to that with conventional permanent magnets (PM), can dramatically increase the torque/power density, enabling HTS electric machines that are smaller and lighter than conventional devices having the same rating [13]. Thus, effective trapped flux immobilization in HTS bulk cryomagnets is crucial in engineering applications, increasing the need for a complete understanding of trapped flux behavior and practical magnetization techniques.

Attempts have been made to obtain a satisfactory trapped flux density and homogenous critical current distribution using both material preparation and magnetization techniques [14-20]. Commonly used magnetization techniques to activate HTS bulk cryomagnets have included ZFC magnetization, FCM, and PFM. In ZFC, the bulk is cooled below its T_c prior to excitation with an external magnetic field. In FCM, the bulk is placed under the external magnetic field B_{app} before cooling below T_c. In PFM, the applied magnetic field is not static but momentarily applied within the order of milliseconds. For practical reasons, HTS applications demand lower magnetization power without compromising the trapped flux performance. Until now, uncertainties exist regarding the magnitude of the desired applied field and waveform of the transient B_{app} as a function of time that are needed to fully magnetize the bulk [21]. The main obstacle is that the trapped field using PFM is smaller than that using FCM, due to the transient heat caused by flux motion or flux jump [22]. Notably, in past studies the polarization of the applied magnetic field has been parallel to the *c*-axis of the bulk with the above magnetization procedures.

In recent years, researchers have begun to use experimental results integrated with a numerical simulation analysis of the J_c distribution on the *a-b* plane of HTS bulk cryomagnets in order to reproduce the trapped flux distribution and understand their exact performance to be applied to HTS bulk machines [23]. A key consideration and obstacle is the suitable definition of the J_c spatial distribution, caused by the inhomogeneities of the HTS bulks. Consequently, numerous experimental results are needed to provide a reference for the proper modeling of the HTS bulks. Generally, the superconductivity properties of large, single grain HTS bulk cryomagnets vary with their relative positions, thus making it difficult to perfectly define the current distribution. Current studies using numerical simulation - for example, in PFM - may provide information only in the case when the externally applied field B_{app} is parallel to the *c*-axis upon magnetization. In both experimental and numerical studies, there have been no targeted efforts to magnetize these bulks under an external field B_{app} at inclined angles to the *c*-axis.

Although the global behavior of the magnetic flux in single crystal materials has been much studied, the interactions between the vortex and the various structural defects present in large-sized single-grain bulk materials have more practical relevance. The flux pinning mechanism becomes more complex when the defect structures and anisotropy characteristics interact during the process of magnetization, because pinning is not simply additive [24,25]. As a result, power applications using GdBCO cryomagnets have been severely restricted and remain confined to the prototype stage, although they have superior performance in sustaining strong magnetic fields thanks to the addition of the second phases like

Gd_2BaCuO_5 [26,27].

To our knowledge, for the first time, it opens the possibility to study the trapped flux behaviour when the bulk experience inclined applied field during magnetization. Moreover, tiny steel wires are adopted to detect the trapped flux distribution visually, which provide compensated information for the spatial distribution of trapped flux. In the present study, we exhibit that the trapped flux of GdBCO under off-axis FCM geometry with θ up to at least 30° retains a comparable amount with that occurring under on-axis magnetization. It may benefit future machine designs if the off-axis magnetization is effective and provides the equivalent flux trapping of conventional on-axis magnetization. Meanwhile, the experiment results provide the basis for a deeper understanding of the anisotropic characteristics of bulk cryomagnets.

A GdBCO-QMG®[28] sample of 60 mm in diameter and 20 mm in thickness prepared by Nippon Steel & Sumitomo Metal Corporation was employed to investigate the trapped flux behaviour using off-axis FCM as shown in Fig. 2-5(a). To apply the magnetizing field, we employed a 5 T superconducting magnet with a 300-mm room temperature bore (JMTD–5T 300M–PC, Japan Magnet Technology, Inc.) by Japan Magnet Technology. In the application and removal processes of B_{app}, the field sweep rate was set at 1.39 mT/s. The bulk was mounted on a self-designed sample holder to keep the angle θ with respect to the *c*-axis of the bulk at 30°, 45°, 60°, 75° and 90° and was cooled down by immersing into a liquid N_2 bath under 3 T (B_{app}) gradually. Considering the influence of anisotropic characteristics on fluxing pinning performances within growth sectors (GSs) and growth sector boundaries (GSBs), two magnetization arrangements were chosen for θ equal to 90°. Fig. 2-5 (b) shows that B_{app} is applied along the centre of the growth sector (GS) and Fig. 2-5 (c) exhibits B_{app} is parallel to the GSB during FCM. Once temperature stability was achieved, the applied field was removed. After the removal of the external field, the trapped flux measurement by using Hall sensor (F. W. BELL, model BHT-921) was started after 75 minutes to eliminate the major flux creep. The active area of the sensor was 0.51 mm in diameter.

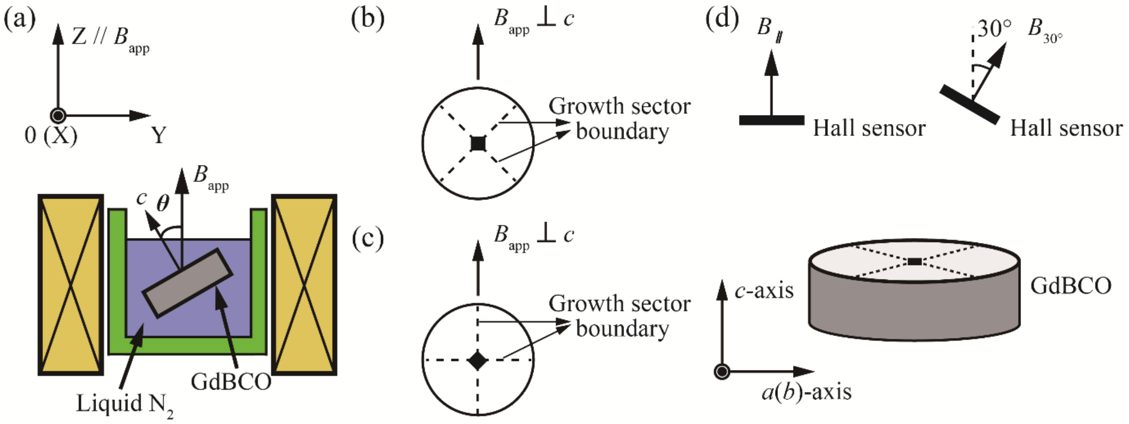

Figure 2-5. (a) Field cooled magnetization (FCM) with applied magnetic field B_{app} which keeps an off-axis angle θ from the crystallographic *c*-axis of the bulk. Magnetic field B_{app} is parallel to Z axis and θ is defined within the Y-Z plane. (b) FCM with misaligned GSB in which B_{app} is applied along the centre of the growth sector (GS). (c) FCM with aligned GSB in which Bapp is applied parallel to GSB. (d) Two measurement configurations with Hall sensor. Left: Hall sensor is parallel to the bulk surface and we measure the trapped field $B_{//}$ parallel to the *c*-axis. Right: Hall sensor keeps a 30° inclination from the surface and we measure B30° along inclined direction of 30° with respect to the *c*-axis direction. The gaps between the Hall sensor sensing area and the bulk surface are 0.5 mm and 1.6 mm for $B_{//}$ and B30°, respectively.

To evaluate the trapped flux performance in off-axis FCM, magnetic flux density was measured using two different Hall sensor geometries as shown in Fig. 2-5 (d). The trapped flux density $B_{//}$ parallel to the *c*-axis of the bulk and the trapped flux density $B_{30°}$ along inclined direction of 30° with respect to the *c*-axis direction are obtained. In the measurement of $B_{//}$, the sensing area of Hall sensor maintains a 0.5 mm gap to the bulk surface. The trapped magnetic flux density was measured at every 1 mm grid step. The Hall sensor is mounted on an X-Y-Z movable platform and the measurement range is 70×70 mm^2 over the top surface. $B_{//}$ and $B_{30°}$ were measured and well confirmed with the reproducibility. The integrated flux Φ was calculated by using the trapped flux density $B_{//}$ as described above.

2.3.1 Trapped field results

Here, the results of FCM experiments on the high-T_c ceramic superconductor GdBCO are displayed. Specifically, we measured the longitudinal component as a function of field orientation, i.e., parallel component to the *c*-axis of the remnant magnetization after the external magnetic field was removed. The observed phenomena include (1) a quite gradual variation in the maximum trapped field density B_{max} and the integrated trapped flux Φ from 0° to 30°, as well as an obvious reduction from 60° to 75°; and (2) distinctive trapped field behaviors for two different magnetization polarization configurations, in which B_{app} is applied in the crystallographic *a-b* plane, parallel to the growth sector boundary (GSB) and in the growth sector (GS) at the liquid nitrogen temperature and a high angle. We verified the feasibility of this novel magnetization geometry considering the magnitude of trapped flux density and the orientation of the trapped flux.

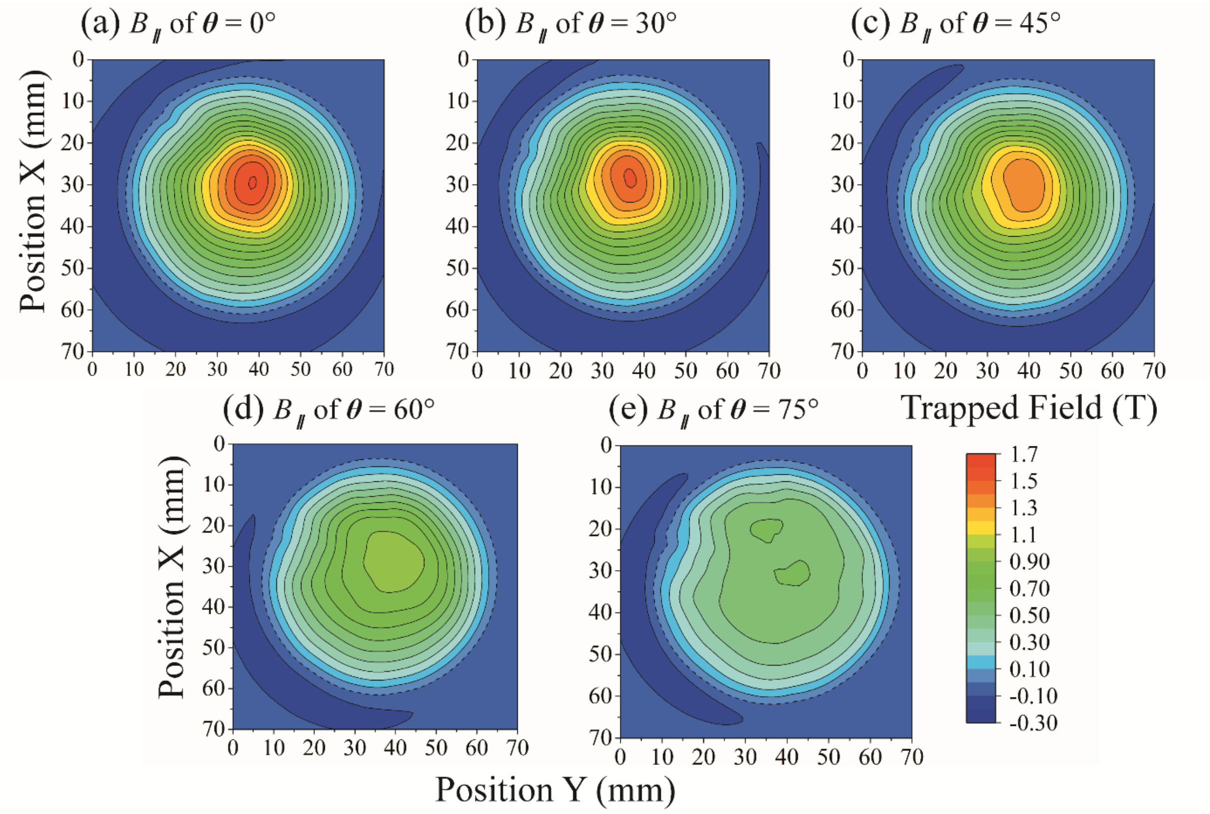

Figure 2-6. Trapped flux distribution measured after FCM, in which Hall sensor is parallel to the bulk surface. (a), (b), (c), (d) and (e) represent the $B_{//}$ distributions under on and off-axis FCM with θ of 0°, 30°, 45°, 60° and 75°, respectively.

Figs. 2-6 (a) to 2-6 (e) show the $B_{//}$ distributions with θ of 0°, 30°, 45°, 60° and 75° under off-axis FCM, respectively. The sample is arranged in the centre of the scanning area of 70 mm × 70 mm, keeping bulk centre at 35mm both in X and Y direction. Fig. 2-6 (a) shows the maximum $B_{//}$ under on-axis FCM is 1.6 T as mentioned above and has been chosen as a reference for the following analysis. With increasing θ, $B_{//\mathrm{max}}$ decreased monotonously as shown in Figs. 2-6 (a) to 2-6 (e). Table 2-2 exhibits that the observed $B_{//\mathrm{max}}$ decreases from 1.6 T to 0.55 T as a function of θ. It is noted that $B_{//\mathrm{max}}$ of 1.54 T achieved when θ is 30° retains 96 % of that when θ is 0°, which confirms the useful performance of GdBCO bulk under off-axis FCM with θ up to 30°.

In these results, all the 2D trapped flux profiles under on-axis FCM exhibit a quasi-concentric pattern, showing that the induced current is nearly unimpeded and circulates freely at the scale of the *a*-*b* plane of the sample. Thus, this sample can be considered a high quality “single grain” perovskite material from an electromagnetic point of view. Meanwhile, the area of trapped flux density over zero maintains a quasi-perfect circle shape with a diameter of 60 mm, which coincides with the geometric dimension of the bulk sample for all FCM conditions. These results show that the trapped flux maintains the same orientation parallel to the *c*-axis, at least on the periphery of the bulk under off-axis FCM. The trapped flux orientations in the vicinity of the crystal seed are discussed later.

Under off-axis FCM and at each measuring angle, the trapped field remains at a corresponding maximum value B_{max} in the central part after the external magnetic field is removed. The B_{max} tends to shift toward the periphery when θ is 75°. This motion of the B_{max} can be explained in two ways: that the maximum trapped flux moves after flux creep, and that the trapped flux is inclined leading to the displacement of B_{max}. Specifically, distortion begins in the trapped flux distribution by an anisotropic characteristic, which is obvious in the center part shown in Figs. 2-6 (d) and 2-6 (e). The maximum trapped field B_{max} and integrated trapped flux Φ under the off-axis FCM are summarized in Table 2-2. The differences in B_{max} and Φ are listed to compare the trapped flux performance under off-axis and on-axis FCM. A particularly high B_{max} is achieved at 0° with a saturation value of 1.6 T at a liquid nitrogen temperature. The maximum trapped field values in the other four cases are 96%, 86%, 67%, and 35% of the B_{max} value when $\theta = 0°$. These proportions are larger than the longitudinal component of B_{max} under the inclined applied field, which shows that the trapped flux behaviors cannot be simply explained by a vector decomposition scheme.

In isotropic homogeneous materials, the magnetization M is generally along the applied magnetizing field direction. For simplicity, we may presume that the values of $B_{//\mathrm{max}}$ obey the formula 1.6cosθ as a function of θ as shown in Table 1. However, the observed $B_{//\mathrm{max}}$ is larger than 1.6cosθ up to 75°, which may be ascribed to the anisotropy and/or the shape effect of the sample. Meanwhile, with increasing θ, the distortion of $B_{//}$ distribution becomes obvious. The remnant trapped flux distribution for θ equals 60° and 75° shows that the peak area shifts from the centre to the periphery of the bulk. It attracts our attention in the discussion, for the bulk, whether it tends to sustain trapped flux which is parallel to the *c*-axis and irrespective of the orientation of applied field, although the trapped flux is almost polarized along the applied field as expected.

Table 2-2. Maximum trapped flux component $B_{//\mathrm{max}}$ and integrated trapped flux Φ of $B_{//}$ under FCM and maximum trapped flux component $B_{30°}$.

θ [°]	$B_{//}$ [T] (0.5mm gap)			$B_{30°}$ [T] (1.6 mm)
	$B_{//\mathrm{max}}$	$1.60\cos\theta$	Φ [mWb]	$B_{30°\mathrm{max}}$ [T]
0	1.60	1.60	1.46	1.22
30	1.54	1.39	1.42	1.26
45	1.37	1.13	1.40	1.04
60	1.07	0.80	1.31	0.910
75	0.55	0.41	0.811	0.531

On the other hand, the integrated trapped flux shows a relatively moderate rate of decrease compared with B_{max}, which reveals that the maximum trapped field can be influenced easier by increasing the inclination angle. The maximum value of the integrated trapped flux reaches 1.46 mWb when the applied field B_{app} is parallel with the *c*-axis. With increasing inclination angle, it decreases to 1.42 mWb, 1.40 mWb, 1.31 mWb, and 0.811 mWb, which are 97%, 96%, 90%, and 56% of the maximum value at 0°. Comparing the trapped field density for off-axis and on-axis FCM, the results demonstrate the feasibility of the off-axis FCM for activating the GdBCO cryomagnet from 0° to 30°. Notably, when θ =45°, the performance of the integrated trapped flux is also acceptable.

Compared with the results of the off-axis FCM, the obtained trapped flux profiles under the on-axis FCM reveal more homogenous and higher trapped field performance. These profiles show slight differences in the maximum trapped field and almost the same trapped flux distribution pattern from 0° to 45°. For angles over 45°, the trapped flux density profiles show obvious differences regarding the flux distribution and maximum trapped field performance, especially in the center part.

While we cannot yet identify the precise spatial distribution of trapped flux under off-axis applied field, the approximate inclination tendency can be detected by adjusting the Hall sensor with respect to the bulk surface. Using the specially prepared holder of Hall sensor as shown in Fig. 2-5 (d), we can measure the $B_{30°}$, which is the trapped flux density along the direction enclosing a 30° angle with respect to the *c*-axis. Since $\nabla\cdot B = 0$ and effect of probable inclination of the magnetization due to off-axis FCM, larger scanning area of B30° over 0 is expected. Thus, scanning area is enlarged to 70 mm (*x*-direction) × 90 mm (*y*-direction) for $B_{30°}$ measurement, while keeping the bulk centre in the same position as in $B_{//}$ measurement, *i.e.*, 35 mm both in X and Y direction. It is obvious that the intensified peak area of trapped flux shifts to the periphery of the bulk, which confirms that trapped flux is inclined under off-axis FCM as shown in Figs. 2-7 (a) to 2-7 (e). Notably, when θ is 30°, the $B_{30° max}$ of 1.26 T was detected, which is higher than 1.22 T occurring in on-axis FCM (θ is 0°). It indicates the bulk can still sustain full trapped flux potential in off-axis FCM. This result supports the feasibility of off-axis FCM under finite angle inclination.

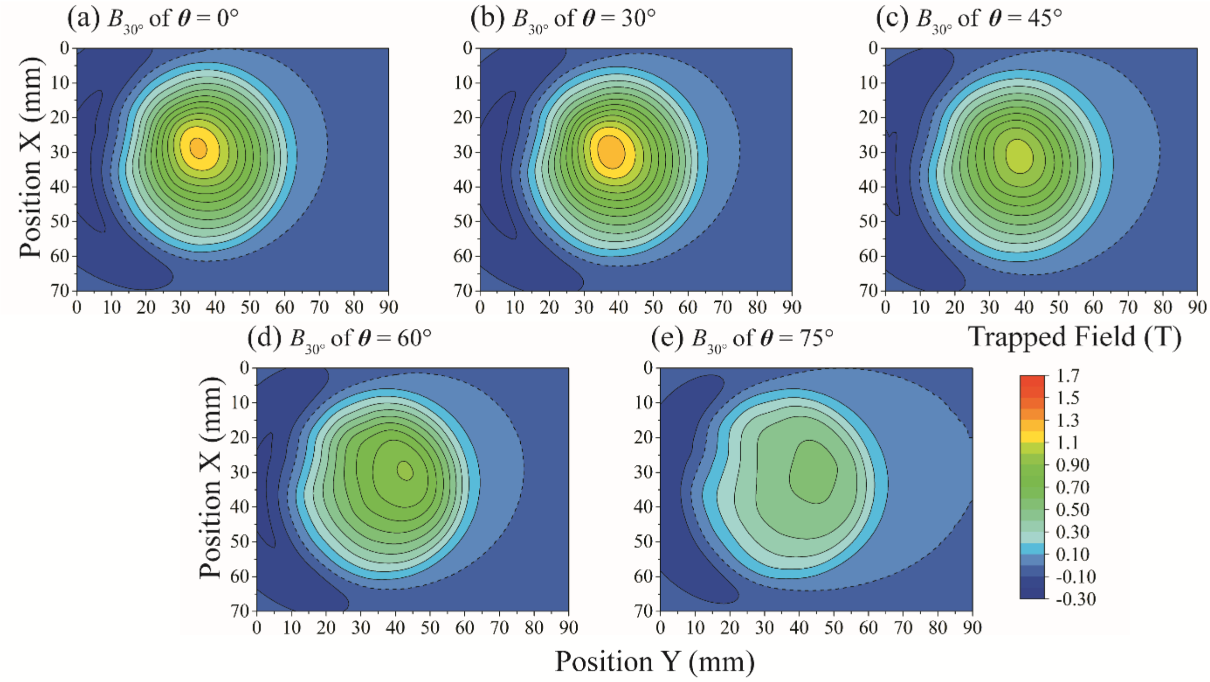

Figure 2-7. Trapped flux distribution measured after FCM, in which Hall sensor is inclined to the bulk surface. (a), (b), (c), (d) and (e) represent the $B_{30°}$ distributions under on and off-axis FCM with θ of 0°, 30°, 45°, 60° and 75°, respectively.

Considering the probable anisotropic flux pinning and J_c distribution in the growth sector (GS) and growth sector boundary (GSB) in the *a*-*b* plane, we have performed FCM with two different polarization configurations for θ at 90° as shown in Figs. 2-5 (b) and 2-5 (c). To confirm the homogeneity of QMG sample, two QMG bulks fabricated in the same process were sliced along aligned GSB direction and misaligned GSB direction respectively as shown in figures 4(a) and 4(b). In Figs. 2-8 (c) and 2-8 (d), a region of 12 mm in *a(b)*-axis direction and 8.5 mm in the *c*-axis direction was investigated to compare the homogeneity along *a(b)*-axis and *c*-axis direction. These results confirm the high quality of the single grain QMG sample for the following characterization.

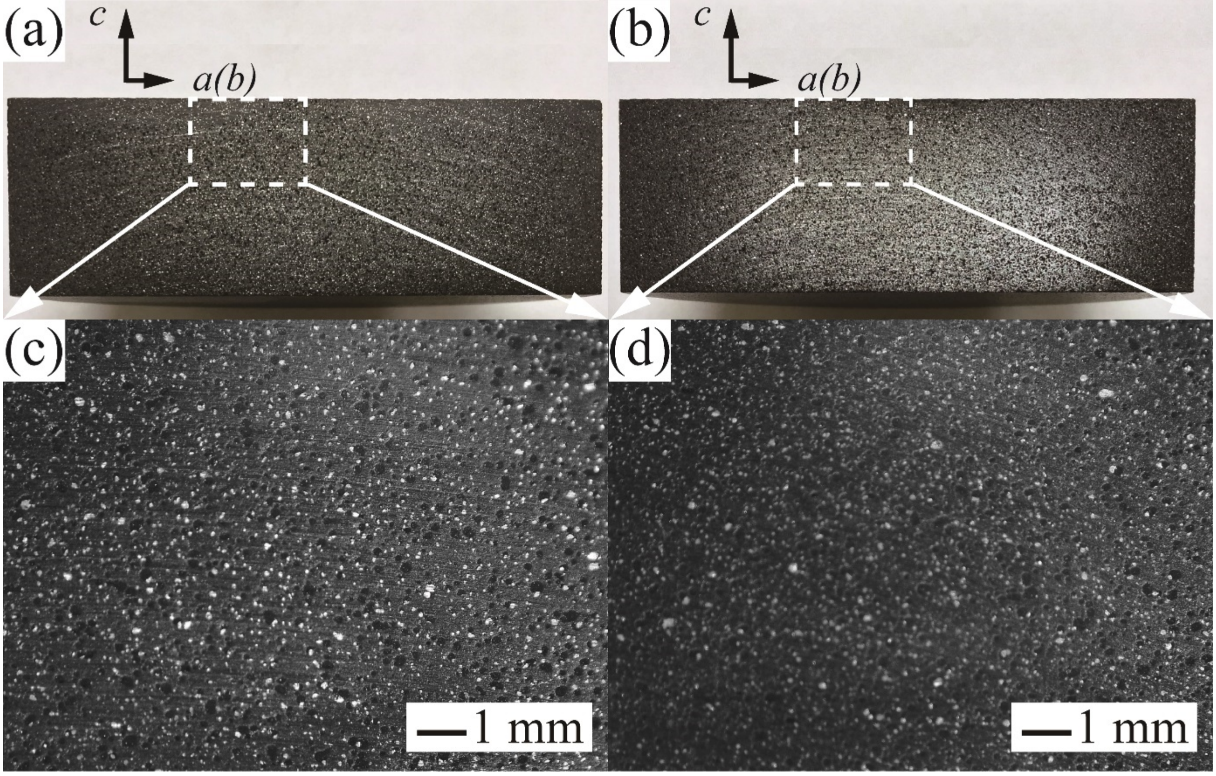

Figure 2-8. (a) Cross section of QMG bulk along the central plane of growth sectors (misaligned GSB). (b) Cross section of QMG bulk along growth sector boundaries (aligned GSB). (c) and (d) represent the micrographs for the misaligned GSB and aligned GSB cross section respectively. Positions of the selected 12 mm × 8.5 mm regions are noted by white marks.

Tiny Zn alloy steel wires of 0.3 mm in diameter and 1 to 2 mm in length are employed to observe trapped flux distribution around the bulk sample. After the stabilization of trapped flux, wires are put into a plastic box over the bulk surface keeping the bulk immersed in liquid N_2. The thickness of plastic box is 2 mm. As shown in Figs. 2-8 (a) and 2-8 (b), the trapped flux comes out of the bulk surface and re-enter the bulk from the bottom as expected. In Figs. 2-8 (c) and 2-8 (d), the magnetic flux lines are symmetrically distributed along the B_{app} orientation after FCM with misaligned GSB. The magnetic flux is mainly trapped along the *a*-*b* plane of the layered perovskite structures. However, in the results of FCM with aligned GSB, the trapped magnetic flux seems to be inclined to the *a*-*b* plane and escape from the periphery of the bulk as shown in Figs. 2-8 (e) and 2-8 (f). A possible interpretation on the different trapped flux distributions under $\theta = 90°$ might be the following: around GSB of melt-growth GdBCO bulk, part of the grains which are disoriented with the prevailing crystal structures which may lead to minute *c*-axis component of magnetic field associating with superconducting current even when the applied field is perpendicular to the *c*-axis during FCM.

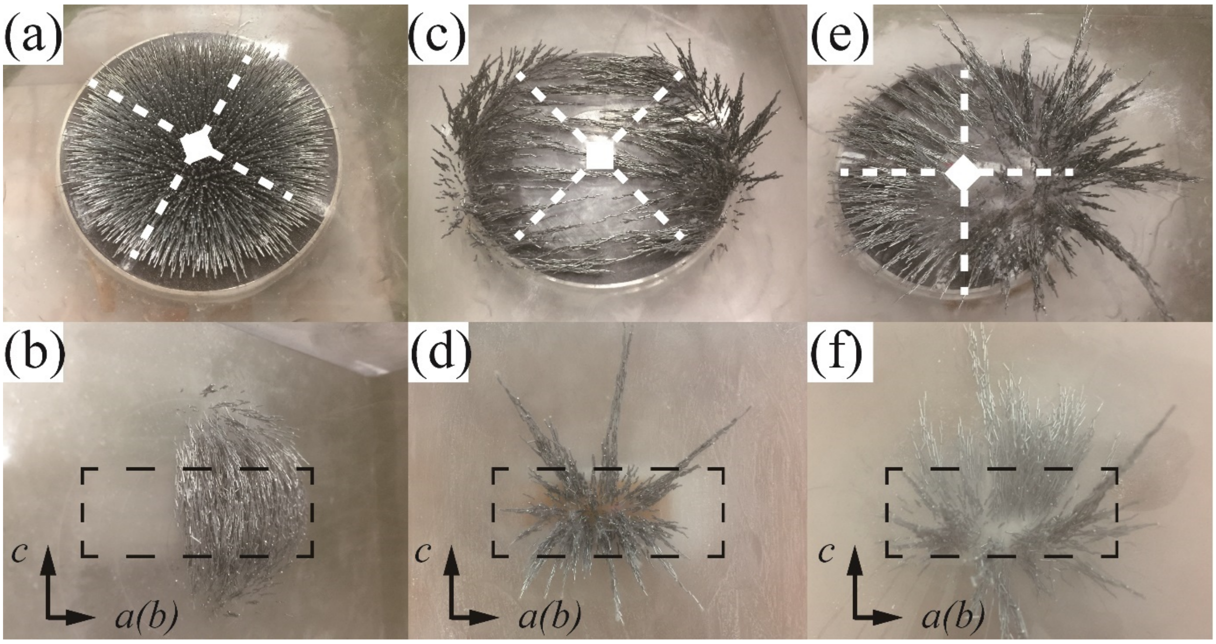

Figure 2-9. (a) and (b) represent trapped flux distribution on the bulk surface and lateral flux distribution after on-axis FCM respectively. (c) and (d) represent trapped flux distribution on the bulk surface and lateral flux distribution after FCM with misaligned GSB. (e) and (f) represent trapped flux distribution of bulk surface and lateral flux distribution after FCM with aligned GSB. In (a), (c) and (e), growth sector boundaries are emphasized. Broken lines in (b), (d) and (f) indicate the QMG sample immersed in liquid N_2.

In Fig. 2-10, the experiment results are summarized, the maximum trapped flux $B_{//\max}$, the trapped flux integrated on the surface of the bulk Φ are shown as a function of off-axis angle in FCM. In addition, $1.6\cos\theta$ is plotted as the reference of the angular dependence of magnetization as expected with a constant magnetization value of 1.6 T. With increasing θ, the integrated trapped flux decreases moderately compared with $B_{//\max}$. For θ = 90°, the trapped flux over the bulk surface is near 0. It is worth to note that $B_{//\max}$ is larger than $1.6\cos\theta$ in the range of $0° < \theta < 90°$. While we cannot identify the exact cause of the $B_{//\max}$ larger than $1.6\cos\theta$, we figure out the following speculations which might appear attractive.

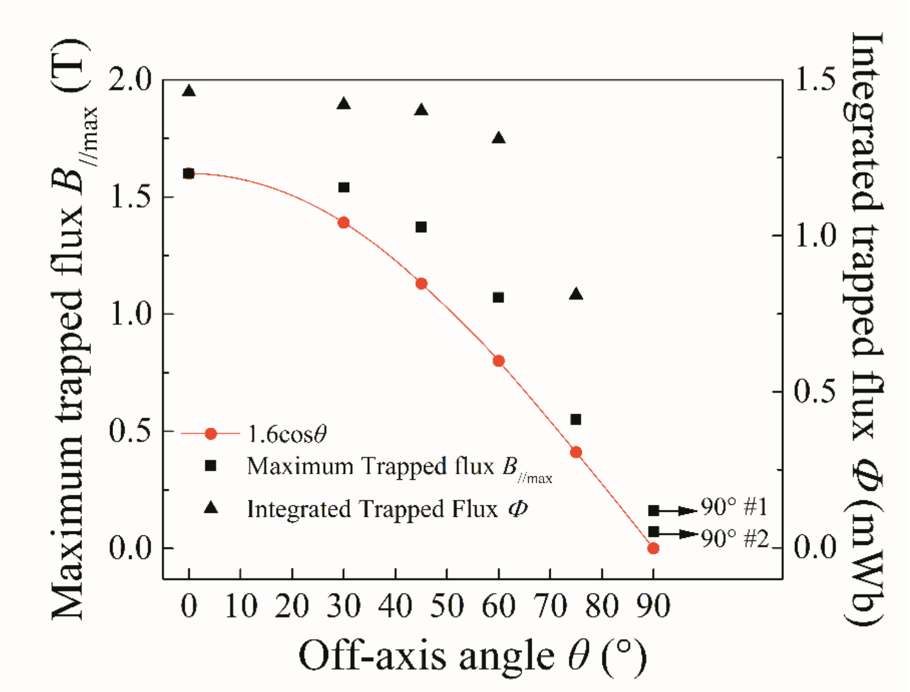

Figure 2-10. Angular dependence of trapped flux under on and off axis FCM with θ of 0°, 30°, 45°, 60°, 75° and 90°. 90° #1 and 90° #2 represent aligned growth sector boundary and misaligned growth sector boundary off-axis FCM geometry when $\theta = 90°$, respectively.

During on-axis FCM, the sample is totally penetrated with the thickness along the *c*-axis. While, under off-axis FCM, the penetration thickness in the centre of the bulk is enhanced to h/cosθ along the direction of B_{app}. This increase h (1/cosθ -1) may cause the $B_{//max}$ larger than 1.6cosθ. In this case, inside the bulk after off-axis FCM, the superconducting current circulation may not be remaining in the planes perpendicular to B_{app}. With the existence of B_{app}, superconducting current circulates in planes perpendicular to B_{app}, as shown in Fig. 2-11 (a).

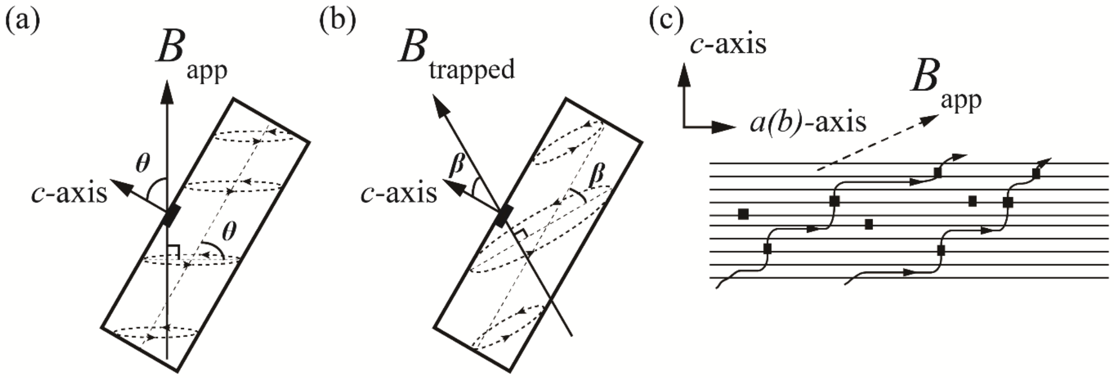

Figure 2-11. (a) The dash planes represent the circulation of superconducting current in off-axis FCM with B_{app}, which is perpendicular to the *c*-axis. (b) After the removal of B_{app}, superconducting current tends to circulate in the plane, which encloses an angle of β ($\beta < \theta$) with the *a*-*b* plane and causes the trapped flux $B_{trapped}$ has the tendency to realigned to the *c*-axis. (c) Kinked flux lines under off-axis magnetic field, which partially align to the *c*-axis trapped by pinning centres in the *a*-*b* plane and connected by Josephson strings.

However, according to material anisotropy together with the existence of Cu-O plane, the supercurrent may have a tendency to circulate in the *a*-*b* planes. After the removal of B_{app}, the supercurrent circulation forced in the plane perpendicular to B_{app} may be preferably reoriented from θ to β ($\beta < \theta$) with the *c*-axis as shown in Fig. 2-11 (b). We suggest the overall effect is to turn the flux line counterclockwise to some extent, which means part of the remnant trapped flux line B_{max} will be rearranged to parallel to the *c*-axis and the rest still remains parallel to the B_{app} as shown in Fig. 2-11 (c). Consequently, the $B_{//\mathrm{max}}$ is larger than $1.6\cos\theta$. Till now, the coexistence of different orientations of the flux lattice has been found in $Bi_2Sr_2CaCu_2O_{8+d}$ superconductors, where the horizontal component of the field induces Josephson vortices and the vertical component induces pancake vortices that coexist separately [29]. This phenomenon may be applicable to GdBCO bulk. However, the exact ratio of the inclined trapped flux to the flux normal to the *a*-*b* plane is unknown, and more investigations are needed into the properties of the material and the interactions with other directional pinning centres.

2.4 Off-axis field cooled magnetization for cubic GdBCO bulk

Generally, the shape of sample may influence the spatial flowing path of superconducting current within the sample. Consequently, the trapped flux would be affected. Here, a same series QMG GdBCO bulk with the previous disk-shaped sample was polished to cubic shape (20 × 20 × 20 mm^3). Then, off-axis FCM was performed using the same procedures as introduced in the section 2.3 as shown in Fig. 2-12 (a). After off-axis FCM, trapped flux distribution for each 6 faces was measured for comparison as shown in Fig. 2-12.

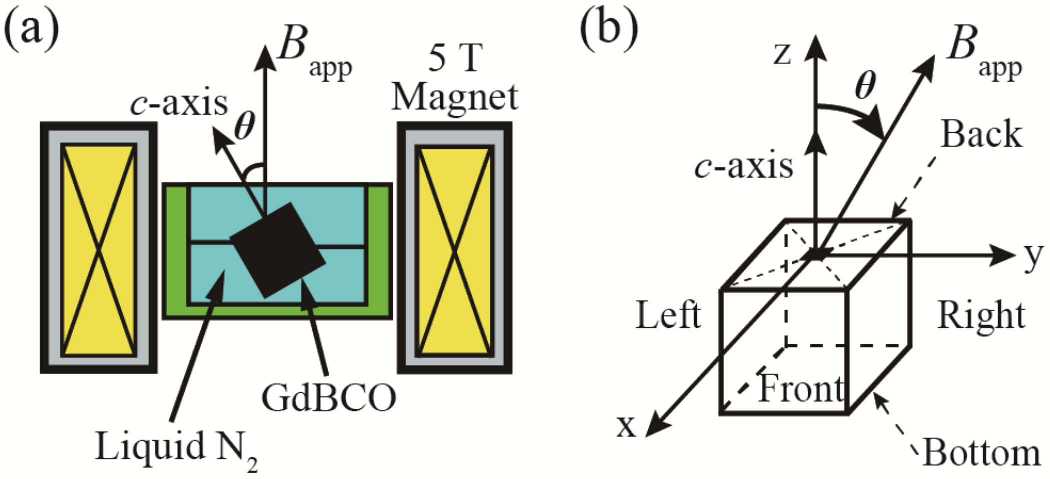

Figure 2-12. (a) Field cooled magnetization (FCM) experiment setup, in which the applied magnetic field B_{app} encloses an off-axis angle θ with the crystallographic *c*-axis of the sample. (b) The coordinate system, x-y-z, used to define the angle between the B_{app} and the sample. The *c*-axis is parallel to the z axis and the θ is defined in the y-z plane. The broken lines on the top surface represent the growth sector boundaries. When θ is 90º, the B_{app} is applied along the x axis, y axis and growth sector boundary, respectively.

2.4.1 Trapped field results

To evaluate the trapped flux performance of cubic sample in off-axis FCM, it was measured at every 1 mm grid step and a 30 × 30 mm^2 range. In every measurement, the bulk is placed in the center of scanning area, namely, the bulk center is at the position of (15 mm, 15mm). The scanning results of FCM experiments for the cubic sample is shown in Fig. 2-13.

Figs. 2-13 (a) to 2-6 (e) show the $B_{//}$ distributions with θ of 0°, 10°, 20°, 30°, 45°, 60° and 75° under off-axis FCM, respectively. Specifically, we measured the longitudinal component as a function of field orientation, i.e., parallel component to the *c*-axis of the remnant magnetization after the external magnetic field was removed. The observed phenomena include (1) a gradual variation in the maximum trapped field density B_{max} and the integrated trapped flux Φ from 0° to 75°; and (2) Since $\nabla \cdot B = 0$ and an enlarged large $B < 0$ area is detected as shown in the Figs. 2-13 (c), (d), (e), (f) and (g). It is obvious that trapped flux is inclined for cubic sample under the off-axis FCM.

Fig. 2-13 (a) shows the maximum trapped flux $B_{//\mathrm{max}}$ under on-axis FCM is 0.546 T and is chosen as a reference for the following analysis. With increasing θ, $B_{//\mathrm{max}}$ decreased monotonously as shown in Figs. 2-13 (a) to 2-13 (g). Table 2-3 exhibits that the observed $B_{//\mathrm{max}}$ decreases from 0.546 T to 0.158 T as a function of θ. It is noted that $B_{//\mathrm{max}}$ of 0.477 T achieved when θ is 30° retains 87 % of that when θ is 0°, which confirms the useful performance of GdBCO bulk under off-axis FCM with θ up to 30°.

Table 2-3. Maximum trapped flux $B_{//}$ for top surface under off-axis FCM from 0° to 75°.

Off axis θ [°]	$B_{//}$ [T] (0.5 mm gap)	0.546cos θ [T]	Φ [mWb]
0	0.546	0.546	0.0918
10	0.537	0.538	0.0910
20	0.514	0.513	0.0899
30	0.477	0.473	0.0871
45	0.409	0.386	0.0820
60	0.299	0.273	0.0684
75	0.158	0.141	0.0451

It is notable that the trapped flux performance almost follows the relationship of 0.546cosθ, where 0.546 stands for the maximum trapped flux value achieved when θ is 0°. It can be concluded that the cubic GdBCO shows isotropic trapped flux performance, which will be given in more details in the discussion part.

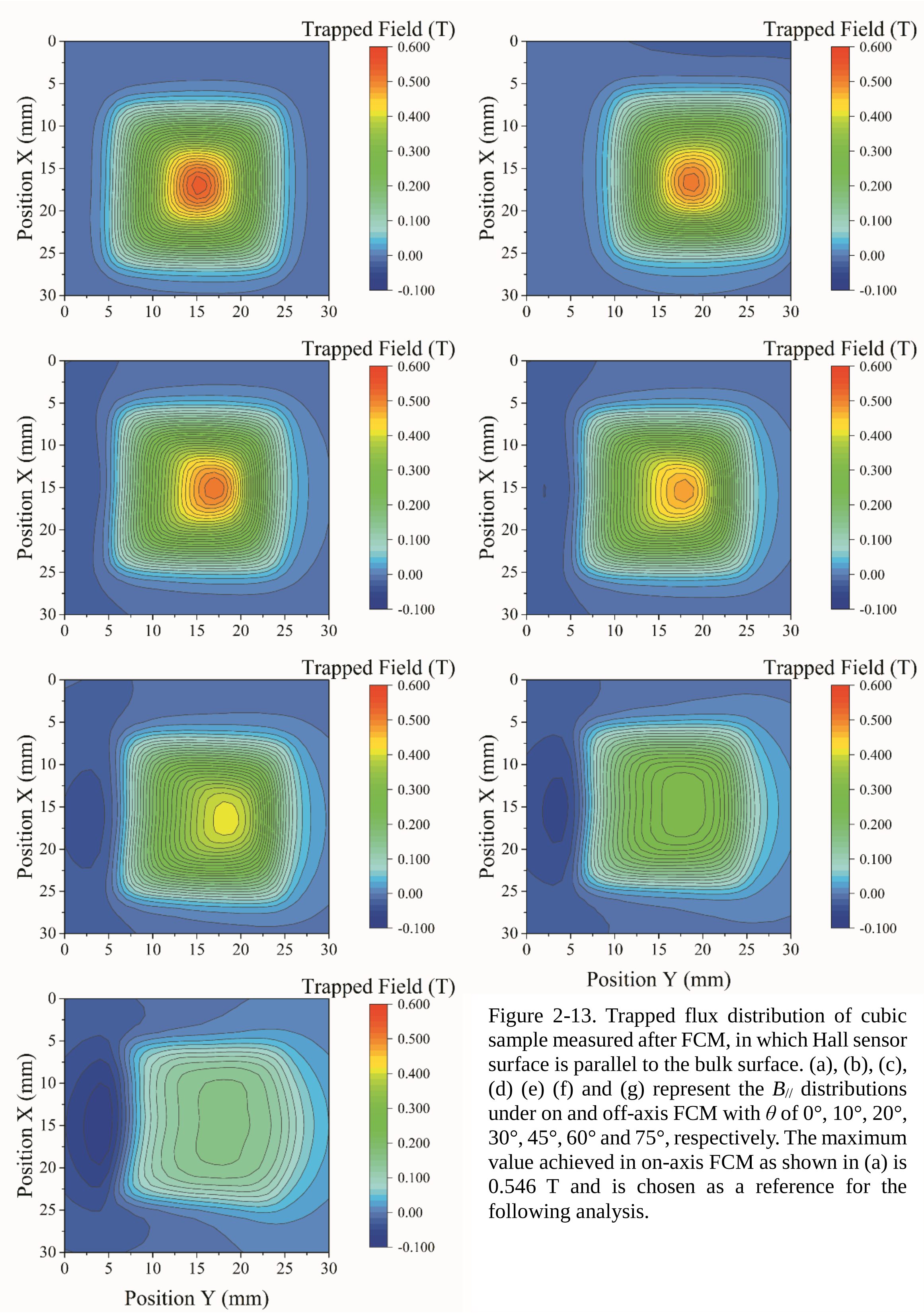

Figure 2-13. Trapped flux distribution of cubic sample measured after FCM, in which Hall sensor surface is parallel to the bulk surface. (a), (b), (c), (d) (e) (f) and (g) represent the $B_{//}$ distributions under on and off-axis FCM with θ of 0°, 10°, 20°, 30°, 45°, 60° and 75°, respectively. The maximum value achieved in on-axis FCM as shown in (a) is 0.546 T and is chosen as a reference for the following analysis.

In Fig. 2-14, the experiment results are summarized, the maximum trapped flux $B_{//\mathrm{max}}$, the trapped flux integrated on the surface of the bulk Φ are shown as a function of off-axis angle in FCM. In addition, 0.546cosθ is plotted as the reference of the angular dependence of magnetization as expected with a maximum magnetization value of 0.546 T. With increasing θ, the integrated trapped flux decreases moderately compared with $B_{//\max}$. For θ = 90°, the trapped flux over the bulk surface is near 1/3 of the maximum value. It is worth to note that $B_{//\max}$ almost follows 0.546cosθ in the range of $0° < \theta < 90°$. While for the integrated trapped flux, the bulk can sustain over 90% of the value achieved in on-axis FCM, which is practical important.

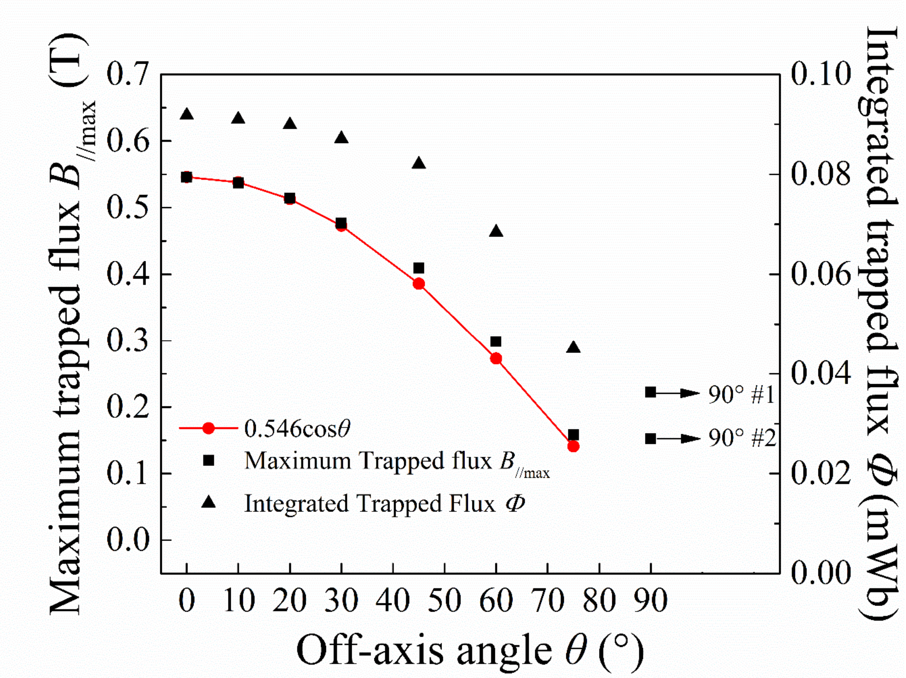

Figure 2-14. Angular dependence of trapped flux under on and off axis FCM with θ of 0°, 30°, 45°, 60°, 75° and 90°. 90° #1 and #2 represent aligned growth sector boundary and misaligned growth sector boundary off-axis FCM geometry when θ = 90°, respectively.

2.5 Discussions

In general, a quantitative understanding of the trapped field behaviour involves flux pinning, flux creep, thermal fluctuation and the effects of unit-cell anisotropy with the triple-layered perovskite structure of GdBCO [30]. Flux vortices are partially pinned between the CuO_2 planes with segments penetrating them which can be regarded as kinks [31]. Also, “pancake” vortices have been assessed in the angular geometry [31,32]. The interaction between the material defects and the trapped flux forms the basis of the flux pinning mechanism and the pinning force of one individual defect depends on its dimension. It is more perplexing when we consider all types of potential pinning centres in a bulk superconductor, because the pinning is directional and dimensionally anisotropic.

Based on the above results, we find that the trapped flux behavior of GdBCO in FCM is angularly dependent and nearly follows the $B_{//\max}\cos\theta$ relationship when the magnetic field is inclined with respect to the *c*-axis of the bulk. The interaction between the material defects and the trapped flux forms the basis of the flux pinning mechanism, and the pinning force of one individual defect depends on its dimension. Also, the thermal fluctuation does not only affect the pinning potentials, but also changes the trapped flux dynamics, which increases the complexity for interpreting this scenario [33]. Much effort has been devoted to studying the motion of magnetic flux in single crystals. It is more perplexing when we consider all types of potential pinning centers in a bulk superconductor, because the pinning is directional and dimensionally anisotropic. Here, we discuss possible inclination of trapped flux with consideration including the superconducting current distribution, columnar defects, layered structures, twin boundaries, and growth sector boundaries within the bulk.

Current Distribution

During the removal of the magnetic field, a superconducting current is induced and the flux lines experience the so-called Lorentz force, F_L, and a pinning force, F_P. When the external field is perpendicular to the *c*-axis, the flux lines are parallel to the Cu-O planes and are driven across these planes by the F_L toward the bulk seed surface or the bottom surface, depending on the current direction as shown in Fig. 2-15 (a). When the external field is parallel to the *c*-axis, the flux lines are driven by F_L toward the periphery of the bulk, as illustrated in Fig. 2-15 (b). One possible mechanism might be responsible for the partly inclined trapped flux, considering the current circulation pattern within the range of $0° < \theta < 90°$. During the removal of the magnetic field, a superconducting current is induced in planes exactly perpendicular to the external field. The current circulates in opposite directions in the two halves of each plane. As shown in Fig. 2-11 (5), the direction of the circulating supercurrent in the area of 1, 3, and 5 has an opposite sign to the direction in the area of 2, 4, and 6. According to crystal anisotropy, by the existence of Cu-O plane, the supercurrent may have a tendency to circulate inner planes, as shown in Fig. 2-15 (d). Therefore, we speculate the overall effect is to turn the flux line counterclockwise, which means the trapped flux line $B_{\max}$ will be rearranged to align in the direction parallel to the *c*-axis.

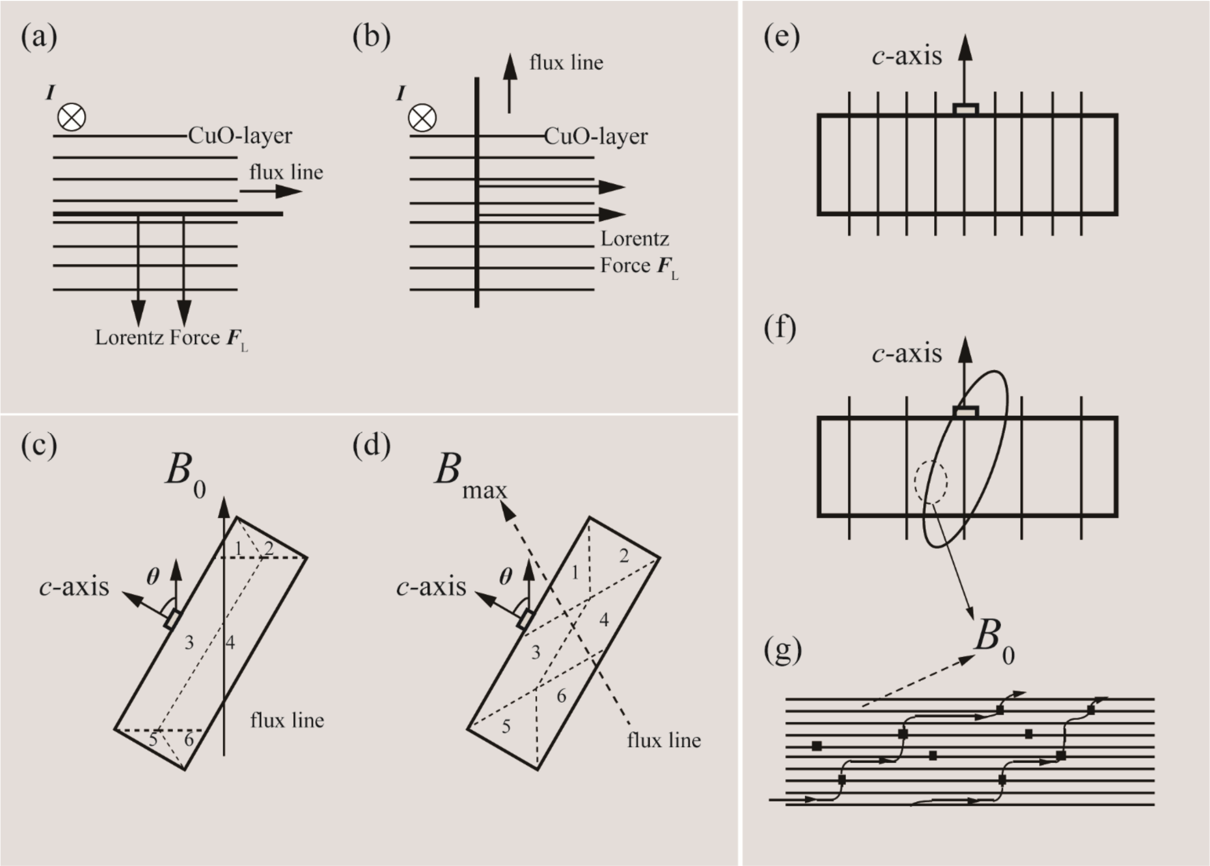

Figure 2-15. (a) Direction of the Lorentz force when $\theta = 90°$. (b) Direction of the Lorentz force when $\theta = 0°$. (c) Schematic portion of superconducting current within the bulk: regions 1, 3, and 5 have the same direction of current, which is opposite to that in regions 2, 4, and 6. (d) Flux line has a tendency to realign to the *c*-axis under the effect of F_L. (e) Trapped flux distribution under on-axis FCM. (f) Trapped flux distribution under off-axis FCM with inclined trapped flux in the vicinity of the crystal seed. (g) Kinked flux lines under an inclined applied field which partially align to the *c*-axis trapped by pinning centers in the *a*-*b* plane and connected by Josephson strings.

In off-axis FCM for disk-shaped sample, the maximum trapped field reaches 0.55 T for θ less than 75°. If all the trapped flux lines are inclined to the *c*-axis, the vector sum of the local magnetic density will surpass 1.6 T, which is unreasonable. Considering the above reformation tendency by F_L, we argue that only a part of the magnetic flux remains inclined to the *c*-axis and the rest is rearranged to align with the *c*-axis. Figs. 2-15 (e) and (f) illustrate this trapped flux distribution for off-axis and on-axis conditions. The vertical lines represent the flux parallel to the *c*-axis. In Fig. 2-15 (f), the closed inclined ellipse represents the remaining inclined trapped flux. The coexistence of different orientations of the flux lattice has been found in BSCCO superconductors, where the horizontal component of the field induces Josephson vortices and the vertical component induces pancake vortices that coexist separately [30]. However, the exact ratio of the inclined trapped flux to the flux normal to the *a*-*b* plane is unknown, and more investigations are needed into the properties of the material and the interactions with other directional pinning centers.

Columnar defects

Columnar defects exhibit a strong pinning effect when the magnetic field aligns the orientation of the vortices to the defects [31]. In a broader definition, linear defects with a certain amount of splay can be included in the correlated category. Specifically, it has been theoretically predicted [32] and experimentally demonstrated [33, 34] that a certain amount of splay improves pinning by keeping the double-kink flux line from escaping. However, the current research mainly focuses on single crystal materials with a controllable orientation of columnar defects. When it comes to bulk materials, the orientation of all columnar defects may only be aligned during fabrication to some extent. Hence, under off-axis FCM, the inclined flux lines will be trapped by proper columnar defects with a tilt angle to the *c*-axis.

Twin boundaries

As another correlated defect, twin boundaries lie in the (1, 1, 0) or (1, -1, 0) planes that are aligned with the *c*-axis. Their trapping flux mechanism is rather complex and yet completely understood. This mechanism has been confirmed as being able to influence the direction of flux lines. According to the report [35], a single twin boundary creates an easy channel for vortex entrance. The vortices penetrate and fill the channel, and then the boundary starts to repel other vortices. At this moment, the boundary becomes an obstacle to transverse magnetic flux motion and only movement along the twin planes proceeds relatively easily. As a result, an additional in-plane anisotropy is introduced that leads to a spatial redistribution of the screening current [36]. For the trapped behavior at $\theta = 90°$, the results show a magnetic flux which mostly escapes from the twin planes and locates perpendicularly to the twin planes in the aligned GSB magnetization geometry, while the flux lines are only slightly inclined to the twin planes. Hence, twin boundaries present a possible mechanism for the inclined flux distribution behavior when the magnetic field is inclined to the *c*-axis.

Layered structure

The triple perovskite layered unit-cell structure of these REBCO oxides introduces additional features in bulk cryomagnets, such as a layer decoupling transition, and modifies the mechanism of pinning and creep in various ways. The layered structure causes two novel phenomena: pancake vortices and Josephson strings, as shown in Fig. 2-11 (g). Kinked flux lines occur in a layered superconductor which consists of point vortices connected by Josephson strings [37]. When the magnetic field B is aligned parallel to the *a*-*b* plane, the vortex lattice will accommodate itself to the layer structure so that the vortex cores lie between the strongly superconducting CuO planes. The current flowing in the planes perpendicular to the *a*-*b* plane will exert a F_L on the vortices. Under this condition, the motion along the *c*-axis will be more difficult compared to that along the *a*(*b*) axis, which is caused by the intrinsic pinning barriers of the superconducting layers. This mechanism will also lead to the inclined flux distribution, especially when $\theta = 90°$.

Fully magnetization achieved in off-axis FCM

Since the superconducting Cu-O layer is perpendicular to the *c*-axis, it is normally accepted that bulks can be only fully magnetized when the magnetizing field *B* is applied parallel to the *c*-axis inducing the superconducting current flowing in the Cu-O plane. Here, based on the results of trapped flux in Figs. 2-10 and 2-14 for disked-shape and cubic GdBCO under off-axis FCM, it can be concluded that fully magnetization can be achieved even if the magnetizing field *B* is not parallel to the *c*-axis as shown in Fig. 2-16. This may come from the interaction between the bundle flux vortex and anisotropic pinning characteristics.

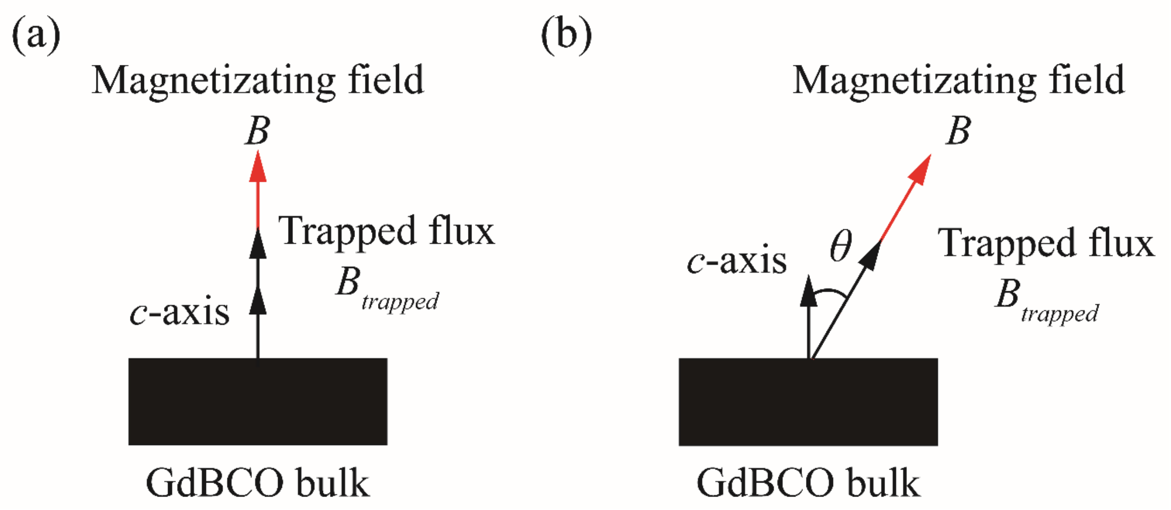

Figure 2-16. Comparison of trapped flux orientation under on-axis FCM and off-axis FCM. (a) In on-axis FCM, the magnetizing field *B* is parallel to the *c*-axis. Since the discovery of REBCO materials, it is normally accepted that it can only be fully magnetized when the magnetizing field is parallel to the *c*-axis due to the existence of Cu-O superconducting layer. (b) In off-axis FCM, the magnetizing field B is applied with an inclined angle θ between the *c*-axis and *B*. In this study, it is confirmed GdBCO bulks can be fully magnetized even the *B* is not parallel to the *c*-axis. Thus, under finite θ, the trapped flux vector component long the *c*-axis direction sustains a high level, which can be effectively utilized in HTS applications.

Such magnetization geometry is practical important for HTS power application, since it offers more freedom for the arrangement of HTS bulks for the *in-situ* magnetization, which will be introduced in Fig. 2-17.

Possible HTS bulks arrangement thanks to off-axis field cooled magnetization

Thanks to the full magnetization under off-axis magnetization geometry achieved in experiments, it makes them highly interesting from the technical view of application design and some technical potential can be immediately explored for the magnetic pole structure as shown in Fig. 2-17. Presently, the magnetization filed *B* is applied parallel to the crystallographic *c*-axis as shown in Figs. 2-17 (a) and 2-17 (c).

With the increasing output power to MW level, single HTS bulk per pole cannot satisfy the required magnetomotive force, which will be explained in more details in Chapters V and VI. Consequently, multiple HTS bulks are urgently needed. For the arrangement of multi HTS bulks, off-axis magnetization will be especially useful as shown in Figs. 2-17 (b) and 2-17 (d). By varying the orientation of HTS bulks leading to off-axis, the distance between HTS bulks and magnetization coils can be reduced, which helps to improve the magnetic flux density in the air gap region.

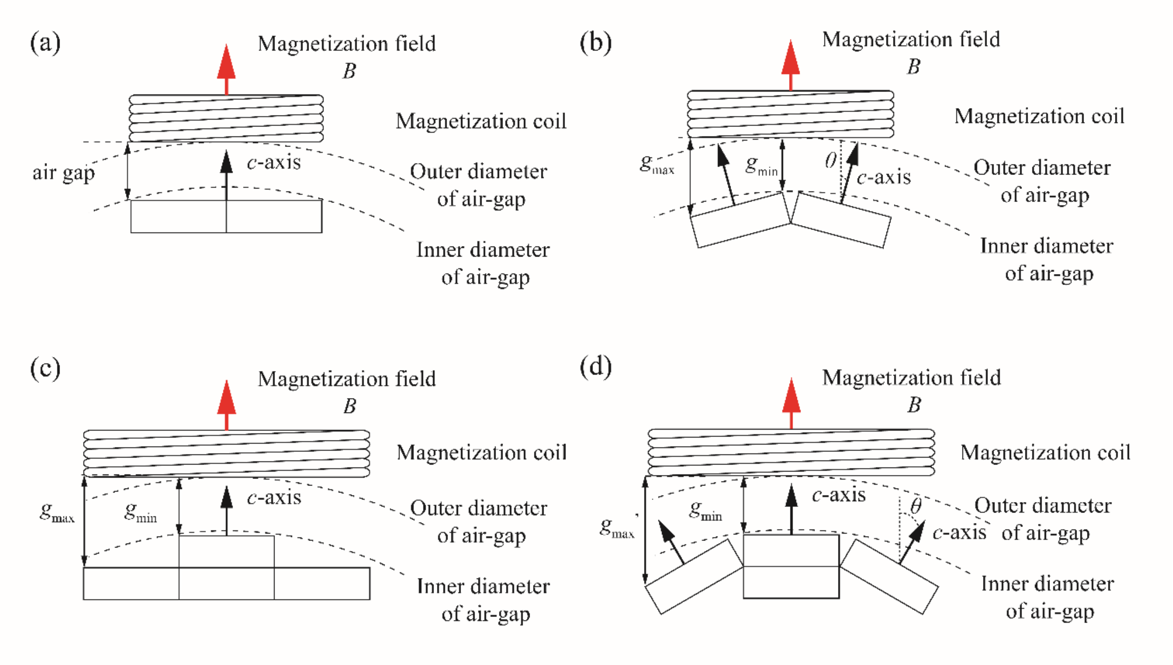

Figure 2-17. Realization of off-axis HTS bulks arrangements with multiple bulks (one layer or two layers), which can be utilized to optimize the air-gap distance. Thanks to the off-axis magnetization, the magnetization field *B* can be applied with an inclined angle θ with respect to the crystallographic *c*-axis. (a) On-axis arrangement of two HTS bulks. (b) Off-axis HTS bulks arrangement, which can reduce the distance between the bulks and magnetization coils. It is notable that the minimum air-gap, $g_{\min}$, can be smaller than the air gap as shown in (a). (c) On-axis arrangement of two-layer HTS bulks. (d) Off-axis HTS bulks arrangement with varied inclined angle θ. With varied inner diameter of air-gap, the inclined angle θ can be adjusted to get a smaller maximum air-gap, $g_{\max}$’, compared with $g_{\max}$ as shown in (c).

Previously, it has been believed that it is totally impossible to effectively magnetize HTS bulks under off-axis FCM. Since the discovery of HTS, everyone believed full magnetization should be done parallel to the *c*-axis due to the existence of superconducting Cu-O plane in HTS REBCO bulks. Thus, the bulk arrangement like Figs. 2-17 (a) and 2-17 (b) are mainly considered for machine design. In this work, it has become clear that the HTS bulks can be fully magnetized under *B* (even if the B is not parallel to the *c*-axis). The reason may come from behavior of flux and vortex kinks in anisotropic REBCO superconductors.

2.6 Conclusions

Nowadays, HTS electrical machines using field poles with BSCCO-2223/1G or REBCO/2G wires are more developed than those using HTS bulks. Thus, researches on HTS bulks are in highly demand to support the design and manufacture of electric machines in their power applications. HTS bulks are continuous medium of superconductor and provide potentially high flux density larger than HTS coils with the same dimension. In this paper, we focused on the off-axis FCM for HTS bulk superconductor GdBCO and experimentally investigated the trapped flux distribution using 2D scanning by Hall sensor and 3D viewer with steel wires at liquid N_2 temperature. With the inclination angle increase up to 30° - 45°, the sample provides superior trapped flux component parallel to the *c*-axis comparable with those obtained by the on-axis FCM. As well, the magnetization after FCM is almost parallel to the applied external field B_{app}. For large inclination angle, trapped flux lines are meaningful to understand the pinning behaviour of bulk materials in which the trapped flux behaviour is a collection of anisotropic flux pinning and the effect of microstructure on the deformed circulation of supercurrent.

Here, off-axis field cooled magnetization is proposed for the first time to our knowledge. Under off-axis angle applied external field, the HTS bulk sustains almost full trapped flux performance. One possible interpretation is that the one body superconductor property has eliminated the anisotropies coming from the crystal structure, making the trapped flux behaviors almost display isotropic characteristics, namely following the $B_{//\mathrm{max}}\cos\theta$ relationship.

Based on the experimental results, the observed off-axis magnetization geometry can be immediately employed into HTS super machine design. Thanks to the effective off-axis magnetization, it provides more freedom of machine design. The off-axis FCM may open up the possibility of future designs with *in-situ* magnetization systems in HTS electric machines.

References

[1] G. Krabbes G, G. Fuchs, W-R Canders, H. May and R. Palka, *High Temperature Superconductor Bulk Materials* (Weinheim: Wiley), **2006**, pp. 106.

[2] Y. Itoh *et al.*, *Advances in Superconductivity* VIII, **1996**, 21996, 707.

[3] T. Ida, K. Shigeuchi, S. Okuda, M. Watasaki and M. Izumi, *Journal of Physics: Conference Series* 695, **2016**, 012009.

[4] D-F Zhou, M. D. Ainslie1, Y-H Shi, A. R. Dennis1, K. Huang, J. R. Hull, D. A. Cardwell and J. H. Durrell, *Appl. Phys. Lett.*, **2017**, 110, 062601.

[5] Available online: http://cesur.en.ankara.edu.tr/low-high-temperature-superconductivity/, Last accessed: **06/08/2017**.

[6] M. Tomita, M. Murakami, *Nature* **2003**, 421, 517-520.

[7] S. Gruss, G. Fuchs, G. Krabbes, P. Verges, G. Stöver, K.-H. Müller, J. Fink, L. Schultz, *Appl. Phys. Lett.* **2001**, 79, 3131.

[8] S. Nariki, N. Sakai, M. Murakami, *Supercond. Sci. Technol.* **2005**, 18, S126.

[9] K. Matsunaga, M. Tomita, N. Yamachi, K. Iida, J. Yoshioka, M. Murakami, *Supercond. Sci. Technol.* **2002**, 15, 842.

[10] L. K. Kovalev, K. V. Ilushin, V. T. Penkin, K. L. Kovalev, A. E. Larionoff, S. M-A Koneev, K. A. Modestov, S. A. Larionoff, V. N. Poltavets, I. I. Akimov, V. V. Alexandrov, W. Gawalek, B. Oswald, G. Krabbes, *Supercond. Sci. Technol.* **2002**, 15, 817.

[11] M. Miki, S. Tokura, H. Hayakawa, H. Inami, M. Kitano, H. Matsuzaki, Y. Kimura, I. Ohtani, E. Morita, H. Gata, M. Izumi, H. Sugimoto and T. Ida, *Supercond. Sci. Technol.* **2006**, 19, S494.

[12] H. Matsuzaki, Y. Kimura, I. Ohtani, M. Izumi, T. Ida, Y. Akita, H. Sugimoto, M. Miki and M. Kitano, *IEEE Trans. Appl. Supercond.* **2005**, 15, 2222.

[13] D.-F. Zhou, M. Izumi, M. Miki, B. Felder, T. Ida, M. Kitano, *Supercond. Sci. Technol.* **2012**, 25, 103001.

[14] C.-X. Xu, A.-M. Hu, M. Ichihara, M. Izumi, Y. Xu, N. Sakai, I. Hirabayashi, *Japan. J. Appl. Phys.* **2009**, 48, 023002.

[15] Y. Xu, M. Izumi, K. Tsuzuki, Y.-F. Zhang, C.-X. Xu, M. Murakami, N. Sakai, I. Hirabayashi, *Supercond. Sci. Technol.* **2009**, 22, 095009.

[16] D.-F. Zhou, K. Xu, S. Hara, B.-Z. Li, Z.-G. Deng, K. Tsuzuki, M. Izumi, *Supercond. Sci. Technol.* **2012**, 25, 205022.

[17] Y.-F. Zhang, D.-F. Zhou, T. Ida, M. Miki, M. Izumi, *Supercond. Sci. Technol.* **2016**, 29, 044005.

[18] T. Ida, H. Matsuzaki, Y. Akita, M. Izumi, H. Sugimoto, Y. Hondou, Y. Kimura, N. Sakai, S. Nariki, I. Hirabayashi, M. Miki, M. Murakami, M. Kitano, *Physica C* **2004**, 412-414, 638.

[19] T. Ida, Z. Li, D.-F. Zhou, M. Miki, Y.-F. Zhang, M. Izumi, *Supercond. Sci. Technol.* **2016**, 29, 054005.

[20] H. Fujishiro, M. Kaneyama, T. Tateiwa, T. Oka, *Japan. J. Appl. Phys.* **2005**, 44, L1221.

[21] R. Weinstein, D. Parks, Ravi-Persad Swah, K. Carpenter, K. Davey, *Appl. Phys. Lett.* **2015**, 107, 152601.

[22] M. Sander, U. Sutter, M. Adam, M. Klaser, *Supercond. Sci. Technol.* **2002**, 15, 748-753.

[23] M. D. Ainslie, H. Fujishiro, *Supercond. Sci. Technol.* **2015**, 28, 053002.

[24] S. R. Foltyn, L. Civale, J. L. Macmanus-Driscoll, Q.-X. Jia, B. Maiorov, H. Wang, M. Maley, *Nat. Mater.* **2007**, 6, 631.

[25] A. Llordes, A. Palau, J. Gazquez, M. Coll, R. Vlad, A. Pomar, J. Arbiol, R. Guzman, S.

Ye, V. Rouco, F. Sandiumenge, S. Ricart, T. Puig, M. Varela, D. Chateigner, J. Vanacken, J. Gutierrez, V. Moshchalkov, G. Deutscher, C. Magen, X. Obradors, *Nat. Mater.* **2012**, 11, 329.

[26] A.-M. Hu, C.-X. Xu C, M. Izumi, I. Hirabayshi, M. Ichihara, *Appl. Phys. Lett.* **2006**, 89**,** 192508.

[27] B.-Z Li, D.-F. Zhou, K. Xu, K. Tsuzuki, J. Zhang, M. Izumi, *Physica C* **2014**, 496, 28.

[28] S. Nariki, H. Teshima and M. Morita, *Supercond. Sci. Technol.* **29**, 034002.

[29] G. Blatter, M. V. Feigel'man, V. B. Geshkenbein, A. I. Larkin, V. M. Vinokur, *Rev. Mod. Phys.* **1994**, 66, 1125.

[30] J.C. Loudon, P.A. Midgley, *Ultramicroscopy* **2009**, 109, 700-729.

[31] H. Ishiharaa, H. Ikuta, Y. Itoh, Y. Yanagi, M. Yoshikawa, T. Oka, U. Mizutani, *Physica C* **2001**, 357-360, 763.

[32] E. H. Brandt, *Rep. Prog. Phys.* **1995**, 58, 1465-1594.

[33] A. E. Koshelev, *Phys. Rev. Lett.* **1999**, 83, 187.

[34] L. Civale, A. D. Marwick, T. K. Worthington, M. A. Kirk, J. R. Thompson, L. Krusin-Elbaum, Y. Sun, J.R. Clem, F. Holtzberg, *Phys. Rev Lett.* **1991**, 67, 648.

[35] T. Hwa, P. Le Doussal, D. R. Nelson, V. M. Vinokur, *Phys. Rev. Lett.* **1993**, 71, 3545.

[36] L. Civale, L. Krusin-Elbaum, J. R. Thompson, R. Wheeler, A. D. Marwick, M.A. Kirk, Y. R. Sun, F. Holtzberg, C. Feild, *Phys. Rev. B* **1994**, 50, 4102.

[37] M. Jirsa, M. R. Koblischka, T. Higuchi, M. Murakami, *Phys. Rev.* B **1998**, 58, R14771.

CHAPTER III

Marine current energy

In this chapter, a brief introduction to the marine current as a renewable energy resource is given, concerning its characteristics and influence on generator design parameters. Then, it gives a look at the marine current resource in Japan waters. Lastly, a theoretical background is presented to demonstrate the relationships between the marine current energy and the generator design conditions.

3.1 Marine current characteristics

The ocean, covering over 70% of our earth, is regarded as possessing enormous energy potential. Driven by the pressure from energy crisis, it is paramount to explore natural and sustainable resources to satisfy the consumption of energy. In general, the sustainable marine energy mainly refers to ocean waves, tides, salinity gradient energy and ocean thermal energy [1]. Thanks to the great accomplishment achieved in wind power utilization during the past decades, the tidal currents are being recognized as another promising sustainable energy to be exploited for the electrical power generation in the coming years [2].

The tides are one of the most reliable phenomena in the world. When the sun rises in the east and the stars come out at night, the ocean waters will regularly rise and fall along the shores. The following figures shows the movement of flood current and ebb currents, with different directions. For the horizontal movement of marine current, general, it accompanies the rising and falling movement as shown in Fig. 3-1. The incoming tide along the coast and into the bays and estuaries is called a flood current; the outgoing tide is called an ebb current. The strongest flood and ebb currents usually occur before or near the time of the high and low tides. The weakest currents occur between the flood and ebb currents and are called slack tides.

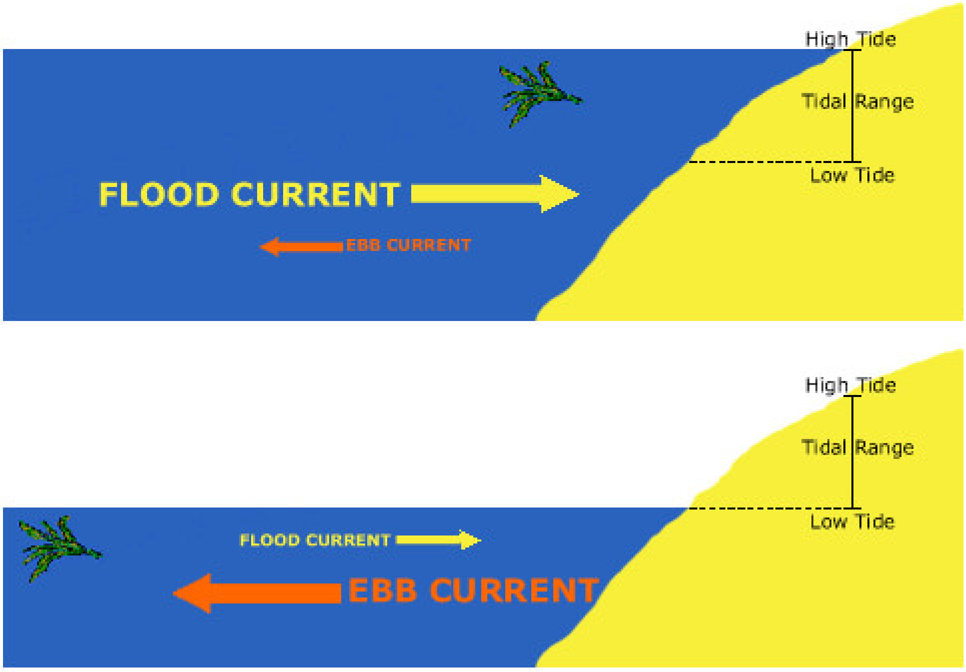

Figure 3-1. The movement of marine currents. The tidal range is also emphasized in the figure.

3.2 Marine current turbine generators sites

In the open ocean, the movement of marine current are relatively weak. However, in the range of 30 to 40 km off-shore including near estuary entrances, narrow straits and inlets, the speed of tidal currents can reach up to 1~8 m/s, which are regarded as the promising marine current sites. Nowadays, research and development (R&D) of marine current energy turbine generator are being busily carried out in countries especially with long coastlines such as China, Japan, UK and France [3].

As long as one imagines a single turbine at a site with a cross section much large than that of a turbine, one would be tempted to draw comparisons with wind power where the theoretically derived maximum for energy extraction, known as the Betz limit, is 59% of the kinetic energy in the free flow. However, at a good wind site there is usually nothing that would block the flow on the sides of the turbine or above it. This means that one can expect a wind turbine to have a relatively small effect on the overall wind conditions and the wind speed is likely to recuperate a certain distance behind the turbine. For a marine current turbine place in a narrow channel on the other hand, the flow will be restricted by the sides of the cannel as well as by the open boundary at the surface. Thus, the assumptions made by Betz in deriving the theoretical value for a wind turbine is most likely not suitable in the case of a marine current turbine in a restricted channel. For instance, if too many turbines are placed in a narrow strait between two islands, the blockage effect would decrease the upstream velocity significantly or divert parts of the flow around the other side of the island instead of past the turbines, A different situation would occur if the turbine were to be placed in a river where the flow is constricted and more or less forced to flow past the turbines.

In any case, it should be clear that the fraction of the kinetic energy that can be extracted is site dependent. This makes it difficult to perform/evaluate general resource assessment for marine current energy that try to take many sites into account by applying the same method for all the sites. One could of course, try to characterize all the sites and put them into different categories, but at present the necessary data and methods to this are often not readily available. The difference in velocity before and after the turbines are deployed should also most likely be incorporated into the design process of the actual marine current turbine generator. As has been shown for a site close to a headland, the velocity in the simulated

There are several characteristics of marine current that make them attractive as an energy source. Marine currents, especially tidal currents are to a large extent predictable and less intermittent than for instance the wind and the sun. As an energy source, they also offer a potentially high degree of utilization, something which could have a strong impact on the economic viability of any renewable energy project [4]. Hence the predictable nature of the resource combined with a limited power of each device could be beneficial for management power delivery in the case of a large scale MCTG farm. In some places, the tide is phase shifted along the coastline, which means that several MCTG farms could be geographically located to even out the aggregated output over the tidal cycle. This has for instance been shown to be the case around the British Isles [5].

A MCTG should be emission free during normal operation. The total emissions during the life cycle of a MCTG are expected to be at a similar level as that of a wind turbine or a wave energy converter [6]. As an example, the carbon intensity of the SeaGen marine current turbine has been found to be comparable to that of a wind turbine in a life cycle assessment [7]. This is of course also technology dependent; for instance, choice of materials, production methods and deployment and decommissioning techniques will affect the emission level during different states of the turbine’s life cycle.

3.2.1 Japan sites

The map showing the marine current resource around the Japan in terms of speeds during one day is displayed in Fig. 3-2 as below:

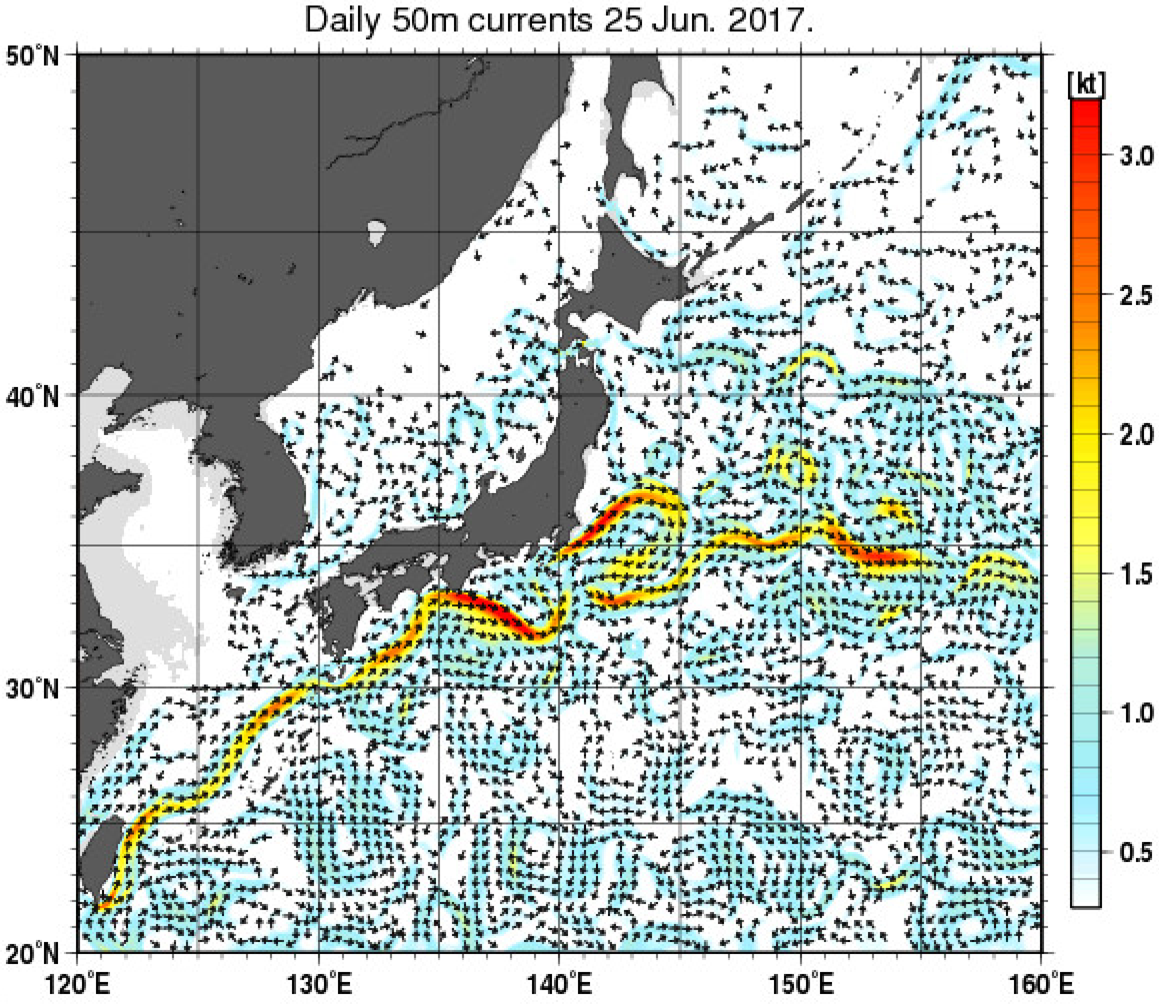

Figure 3-2 The marine current speed around Japan on 25th, July 2017. (1 kt is around 0.514m/s)

As it can be seen from the map, the potential of the marine current energy in Japan is quite significant. The peak speed is around 3.2 kt, namely, 1.6 m/s. Normally, for a 1-MW marine current turbine generator, the cut-in speed and rated speed is 0.75 m/s and 2 m/s [8]. Thus, it is feasible to install MCTGs around the Japan shore [9].

3.3 Theory review

Since the movement of tidal current is the caused by the gravitational effects of the planetary motion of the Earth, the Moon and the Sun, it is high predictable up to 98% accuracy for decades [10]. Meanwhile, sea water is about 800 times the density of air. Hence, compared with other renewable energy techniques like wind and solar energy, marine current energy is promising to yield long-term energy output and reduce the pettiness for energy planning [11].

The conversion of marine current energy aims to utilize the kinetic energy carried by the flowing current. This differentiates marine current energy conversion from traditional hydro power where the amount of energy extracted from a river is dependent on the gravity head potential between the reservoir and the water level below the dam as shown in Fig. 3-3. A similar approach can in fact be used for tidal power in areas with high tides. In that case, a barrage can be constructed in a narrow bay or estuary to utilize the head between low and high water.

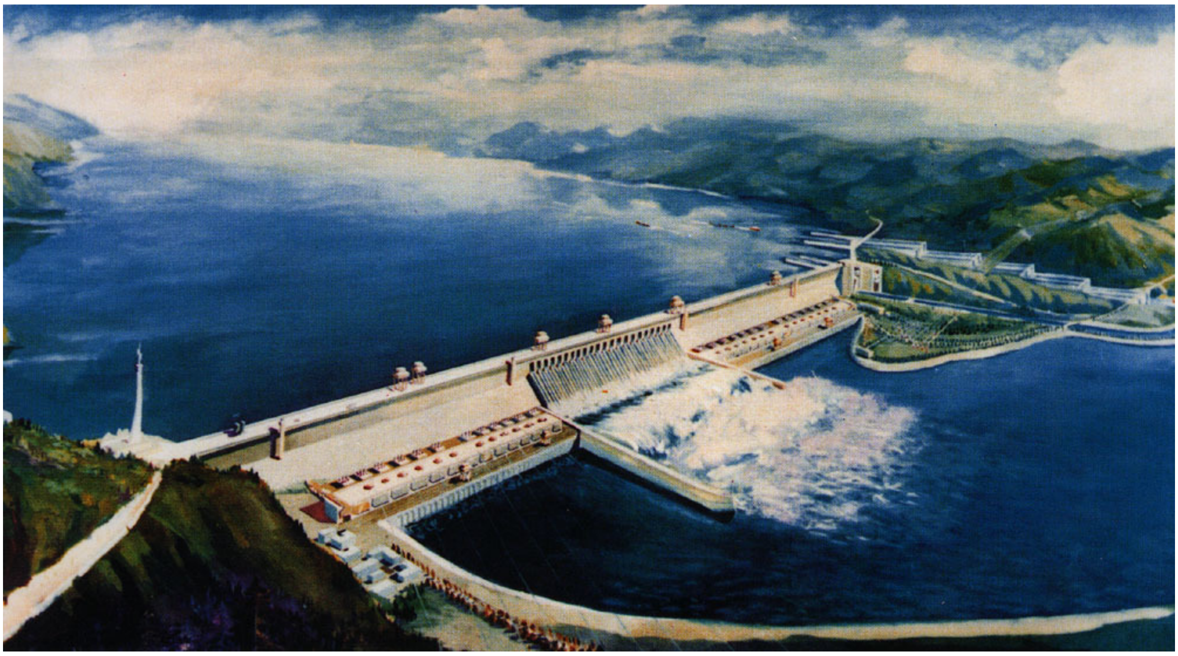

Figure 3-3. The Three Gorges Dam Project in China, which utilize the gravity head potential to generate electricity [12].

Another way to generate electricity from water would then be to convert the kinetic energy of the flowing water which is similar to the way a wind turbine would extract energy from the wind. In that case, a dam or reservoir is not necessary; rather one would be looking for sites where the currents are strong, such as a narrow sound, strait, estuary, around a headland or in a river. In the present study, such topology is adopted and studied in the following sections.

3.3.1 Betz's Law and power coefficient

In the beginning to utilize the marine current energy, the extractable energy for a specific marine current turbine generator should be decided. Generally, in wind energy converter field, Betz's law is employed to determine the maximum extractable energy of a wind turbine generator. Due to the similarities of such flowing medium, air and sea water, it can also be utilized to determine the maximum extractable kinetic energy for a marine current turbine generator. In this section, the fundamental theory of design and operation of the turbines is described. Meanwhile, a detailed derivation of the Betz's equation is presented.

In 1919, the German engineer Alber Betz introduced the fundamental equation for wind energy utilization in his book "Wind energie und ihre Ausnutzung durch Windmuhlen". Here, the theory can be also applied to horizontal marine current turbine generator.

The Betz Equation starts from the marine current speed upstream of the turbine V_1 and the downstream current speed V_2. The limited efficiency of a marine current turbine generator is caused by braking of the wind from its upstream speed V_1 to its downstream V_2, while allowing a continuation of the flow regime. In practical marine current turbine generator, the additional losses are caused by the viscous and pressure drag on the turbine blades, the swirl imparted to the current flow by the turbine, and the power losses in the off-shore transmission and electrical system.

When we treat a marine current turbine generator as an ideal energy converter, the flowing assumption are necessary.

1. The MCTG has infinite number of rotating blades, which do not result in any drag resistance to the marine current through them.

2. The marine current is treated as uniform flowing medium when they pass through the turbine blades, namely same speed and same directions.

Considering the ideal energy converter as shown in Fig. 3-4, the cross-sectional area swept by the rotating blades is defined as S, with the upstream from the MCTG as S_1 and the downstream as S_2.

The current speed passing through the blades is treated as uniform V, with its value of upstream V_1 and downstream V_2 at a distance from the MCTG. The conversion of mechanical energy occurs by reducing the kinetic energy of the current flow from V_1 to V_2, where we can obtain

$$V_2 < V_1 \qquad (3-1).$$

Consequently, the cross-section of current stream increases from the upstream S_1 to the downstream location, and

$$S_2 > S_1 \qquad (3-2).$$

Here, the marine current is treated as incompressible, the conservation of mass can be expressed as:

$$\dot{m} = \rho S_1 V_1 = \rho S V = \rho S_2 V_2 = \text{constant} \qquad (3-3).$$

It shows that the mass flow rate is a constant along the current stream. Continuing with the derivation, Euler's Theorem give the force exerted by the marine current on the blade as

$$\begin{aligned} \mathrm{F} &= \mathrm{ma} \\ &= \mathrm{m}\frac{dV}{dt} \\ &= \dot{m}\Delta \mathrm{V} \\ &= \rho S V (V_1 - V_2) \qquad (3-4) \end{aligned}$$

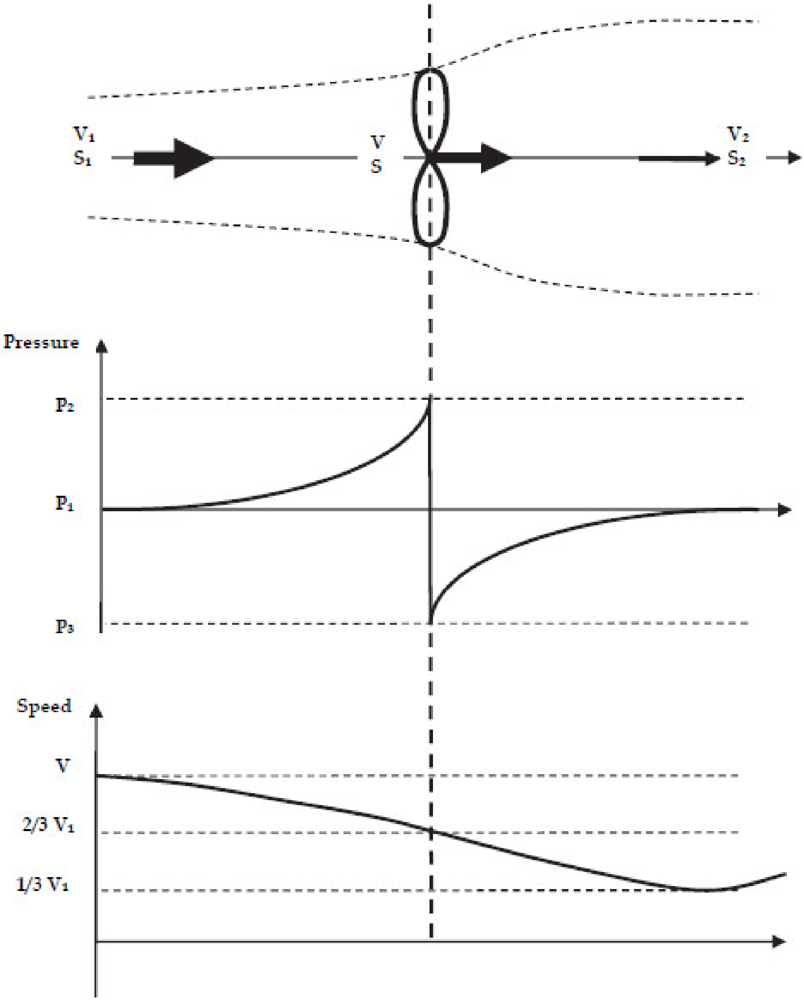

Figure 3-4. Pressure and speed variation in an ideal model of a marine current turbine generator.

The incremental energy in the marine current stream is given by

$$dE = F dx \qquad (3-5),$$

from which the power content of the marine current stream is

$$P = {}^{dE}/_{dt} = F\,{}^{dx}/_{dt} = FV \qquad (3-6).$$

Thus, we can get the extractable power from the current flow is

$$P = \rho S V^2 (V_1 - V_2) \qquad (3-7)$$

The power as the rate of change in kinetic energy from upstream to downstream is given by

$$\begin{aligned} P &\approx \frac{\Delta E}{\Delta t} \\ &= \frac{\frac{1}{2} m V_1^2 - \frac{1}{2} m V_2^2}{\Delta t} \\ &= \frac{1}{2} m (V_1^2 - V_2^2) \qquad (3-8) \end{aligned}$$

Hence, we can get

$$P = \frac{1}{2} \rho S V (V_1^2 - V_2^2) = \rho S V^2 (V_1 - V_2) \qquad (3-9)$$

which implies

$$\tfrac{1}{2}(V_1^2 - V_2^2) = \tfrac{1}{2}(V_1 + V_2)(V_1 - V_2) = V(V_1 - V_2), \qquad \forall \rho, S, V \neq 0 \;\; (3-10).$$

The above calculation suggests that the marine current speed at the blade part may be taken as the average of the V_1 and V_2. It also implies that the MCTG blades act to reduce the current speed but not make the V_2=0. In reality, the extract energy from the current energy, it marine current cannot be totally stopped.

We can rewrite the force F and power P in terms of V_1 and V_2 as

$$\begin{aligned} \mathrm{F} &= \rho S V (V_1 - V_2) \\ &= \frac{1}{2} \rho S V (V_1^2 - V_2^2) \qquad (3-11) \end{aligned}$$

$$\begin{aligned} P &= \rho S V^2 (V_1 - V_2) \\ &= \tfrac{1}{4} \rho S V (V_1 - V_2)(V_1 + V_2)^2 \\ &= \frac{1}{4} \rho S V (V_1^2 - V_2^2)(V_1 + V_2) \qquad (3-12) \end{aligned}$$

Here, an interference factor b can be employed to represent the ratio of the downstream V_2 to upstream V_1 as

$$\mathrm{b} = {}^{V_2}\!/_{V_1}.$$

Thus, the extractable power in terms of b can be expressed as:

$$\begin{aligned} \mathrm{P} &= \tfrac{1}{4} \rho S V (V_1^2 - V_2^2)(V_1 + V_2) \\ &= \tfrac{1}{4} \rho S V_1^3 (1 - b^2)(1 + b) \qquad (3-13) \end{aligned}$$

From the above calculations, we can conclude that the extractable power from the marine current is proportional to the cube of the marine current upstream speed V_1^3, and is a function of the interference factor b.

The power density of marine current energy per unit area can be defined as

$$E = \frac{P}{S}$$

$$= \frac{\frac{1}{2}\rho S V^3}{S} = \frac{1}{2}\rho V^3 \ \left({}^{W}\!/_{m^2}\right) \qquad (3-14)$$

The kinetic power content of the undisturbed upstream current with V=V_1 and over a cross-sectional area S is

$$W = \frac{1}{2}\rho S V^3 \ (W) \qquad (3-15).$$

The power coefficient is the dimensionless ratio of the extractable power P to the kinetic power W available in the undistributed current stream as

$$C_p = \frac{P}{W}.$$

Here, we can get

$$C_p = \frac{P}{W} = \frac{\frac{1}{4}\rho S V_1^3 (1-b^2)(1+b)}{\frac{1}{2}\rho S V^3}$$

$$= \frac{1}{2}(1-b^2)(1+b) \qquad (3-16)$$

To get the maximum C_p, the dC_p/db should be zero, where we can easily obtain that the C_p achieve the maximum value when b=1/3. The maximum C_p is around 0.5926. This is referred to the Betz law. It is the theoretical power fraction that can be extracted from an ideal marine current stream. In Fig. 3.5, the power coefficient C_p as a function of b is displayed. Generally, the b is close related to the hydrodynamic performance of the blades, with a range of 0.3 to 0.5. Till now, the maximum C_p for large-scale MCTG can reach 0.5 [13].

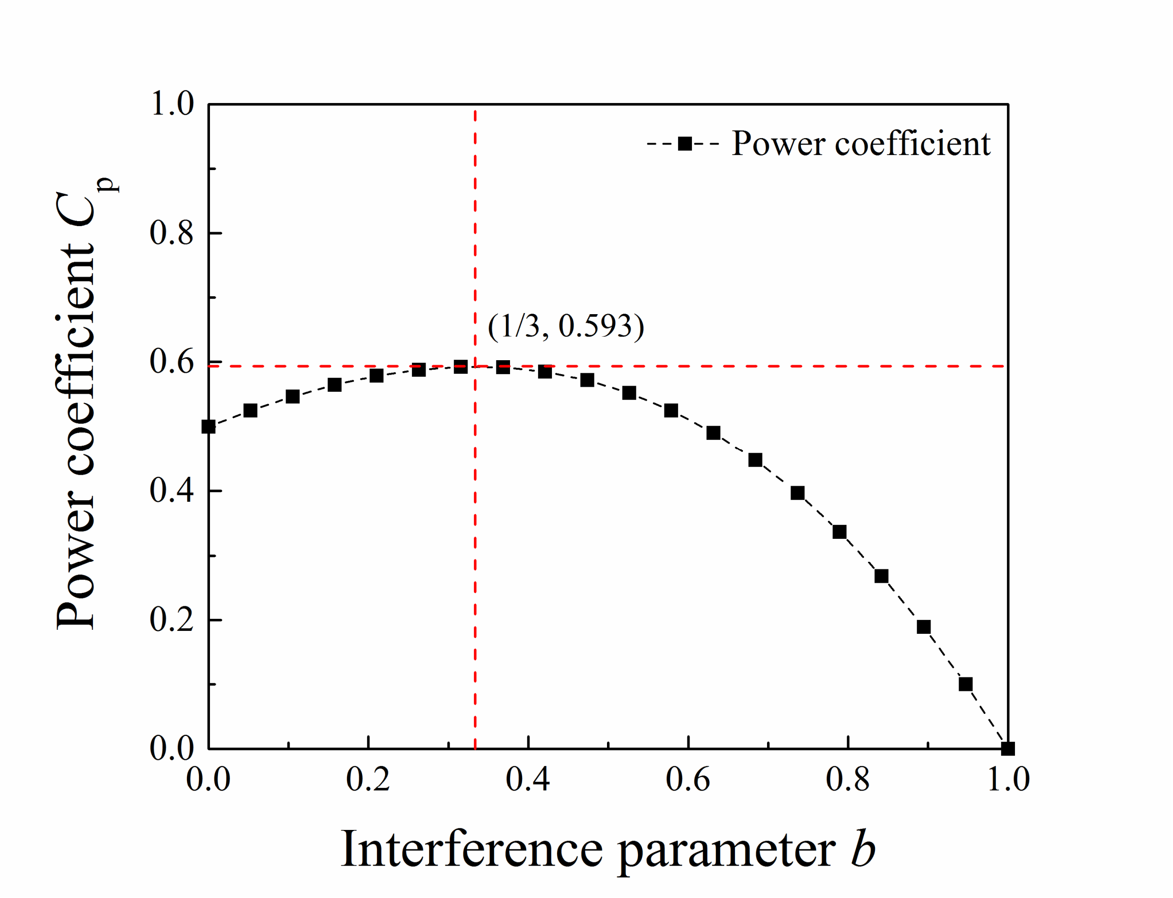

Figure 3-5 The power coefficient C_p as a function of the interference parameter b.

3.3.2 Optimal tip speed ratio

Another important issue for MCTG is related to the rotating speed during working. Normally, the optimal tip speed ratio λ is applied, which is defined as the ratio of the speed of the blade tip to the flowing marine current as

$$\lambda = \frac{speed\ \ of\ \ blade\ \ tip}{marine\ \ current\ \ speed} = \frac{v}{V} = \frac{\omega r}{V} \qquad (3-17)$$

where V (m/s), v (m/s) ω (rad/s) and r (m) represents the marine current speed, blade tip speed, angular velocity and the radius of the blade respectively.

If the blade rotates too slowly, the majority of the current will go through the MCTG without disturbed, which means small fraction of the kinetic energy will be extracted. On the other hand, if it rotates too fast, it will create a large amount of drag, which will degrade the performance of the MCTG.

The tip speed ratio, λ, depends on the blade airfoil profile, the number of blades and the type of MCTG. Till now, the λ falls in the range of 6 to 8 for installed MCTG [14].

3.4 Research and development of marine current turbine generators

In this section, attempts are made to present the relevant works that have been carried out focusing on the rotating marine current turbine generators and index some emerging technologies.

Turbine technology and concepts

The harnessing of the energy in a marine current flow requires the conversion of kinetic energy from a moving fluid, in this case sea water, into the motion of a rotating blades and then drive a generator.

Inspired by the great success achieved in wind energy conversion, not too surprising, many technologies which has been successfully utilized to harness the wind, are directly applied in marine current turbine generators. Based on the structures, most MCTGs can be characterized as belonging to three fundamental types [15]. These are horizontal axis systems, vertical axis systems and variable foil system. In this section, several representative marine current turbine generators are listed focusing on their working condition and structure.

A. Horizontal Axis Turbines

1) The Marine Current Turbine (MCT) Projects (UK) [16].

Fig. 3-6 shows hybrid illustrations of the *Seaflow* turbine. It has a single 11 m diameter rotor, with full span pitch control, and is installed in a mean depth of seawater of 25 m approximately 1.1 km off the nearest landfall at the Foreland Point lighthouse below Exmoor in North Devon, UK. It has exceeded its 300-kW rated power under favorable flow conditions with a 15-rpm rotor speed. It is not grid-connected but as an experimental test-rig dumps its power into resistance heaters capable of absorbing the maximum power. A key feature is that it is mounted on a steel tubular pile, 2.1 m in diameter, set in a hole drilled in the seabed and tall enough to always project above the surface of the sea.

The entire rotor and power system can be physically raised up the pile above the surface to facilitate maintenance or repairs from a boat, a vital requirement as the use of divers or any other form of underwater intervention is virtually impossible in locations with such strong currents. The second project of MCT was *Seagen*. The *Seagen* turbine has its rotors mounted at the outer ends of a pair of streamlined wing-like arms projecting either side of the supporting pile (Fig. 3-6). Each rotor drives a power-train consisting of a gearbox and generator each rated at around 500 kW. The total rated power is approximately 1 MW. Essentially the *Seagen* turbine produces three times the power of *Seaflow*. The *Seagen* project will be followed by an array of similar systems (farm) to be installed in an open sea location. Three turbines will be added to provide a total capacity up to 5 MW.

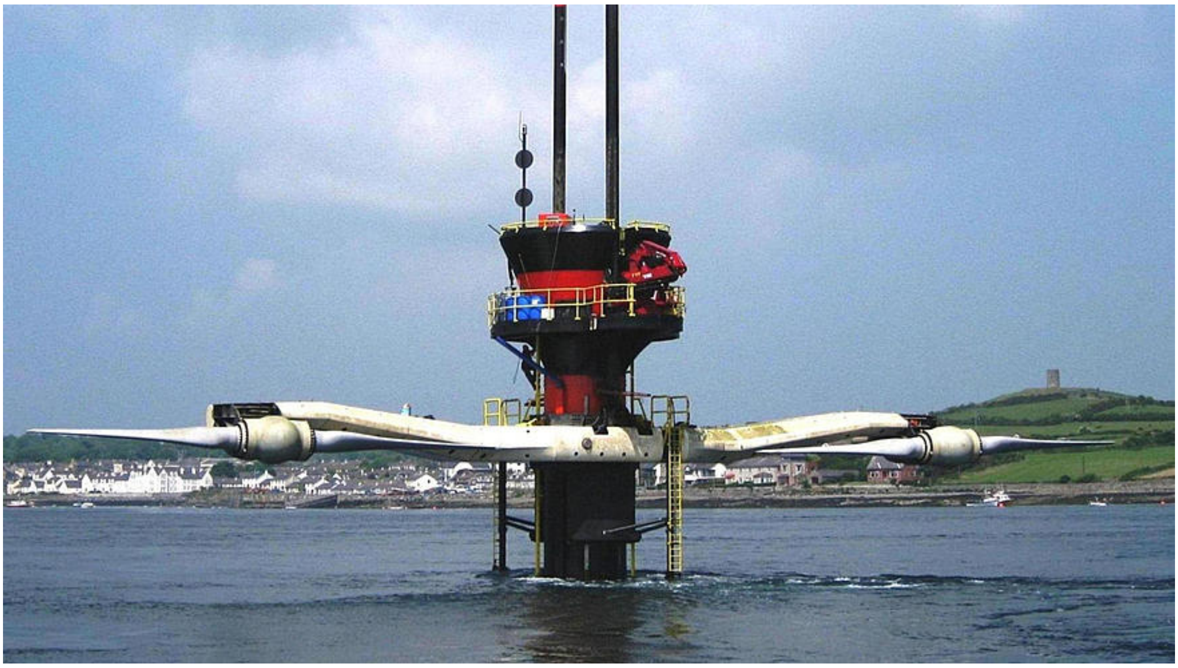

Figure 3-6. The SeaGen project in UK [© MCT].

2) TEC project (ALSTOM) [17]

The TEC is a three-blade horizontal-axis tidal turbine with Variable Speed Pitch Regulated (VSPR) control. The turbine yaws in each slack tide so that its energy extraction plane is perpendicular to the principal flow direction and upstream of the turbine nacelle. The turbine parameters are shown in Table 3-1 with an overview of the design in Fig. 3-7.

Table 3-1: Key parameters of the TEC

Manufacturer	Alstom
Type	Three blade horizontal axis tidal turbine
Serial number	DG4
Production year	2011
Blade radius	9.04 m
Equivalent diameter	18.08 m
Projected capture area	256.74 m^2
Distance above sea bed	9m (turbine centerline)
Foundation	Piled tripod

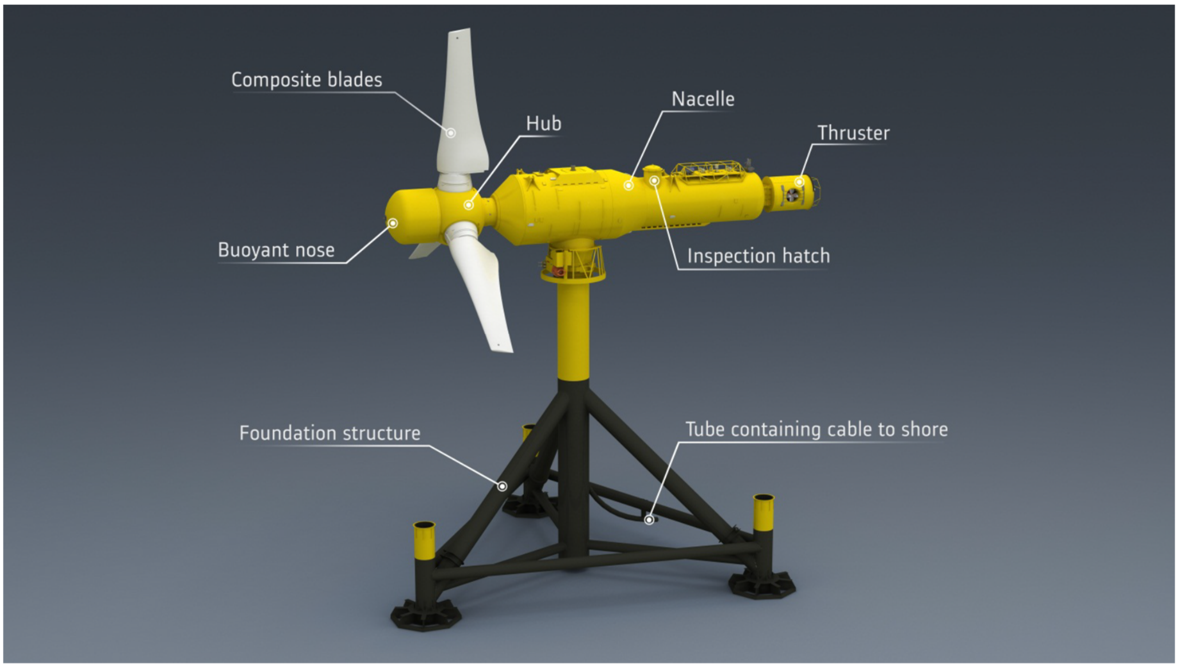

Figure 3-7. Overview of the TEC [© ALSTOM].

3) Rim-driven (Open-hydro) [18]

Open-centre Turbine is a shrouded, horizontal axis turbine, with four key components:

- a horizontal axis turbine,
- a direct-drive PM generator,
- a hydrodynamic duct
- a subsea gravity base support structure.

Table 3-2: Key parameters of the Rim-driven

Manufacturer	Open-hydro
Type	Rim-driven type
Production year	2011
Blade radius	9 m
Equivalent diameter	18 m
Projected capture area	254 m^2
Distance above sea bed 1	9m (turbine centerline)
Weight (including turbine and subsea gravity part)	850 t
Turbine part	350 – 400 t
Subsea gravity part	400 – 450 t

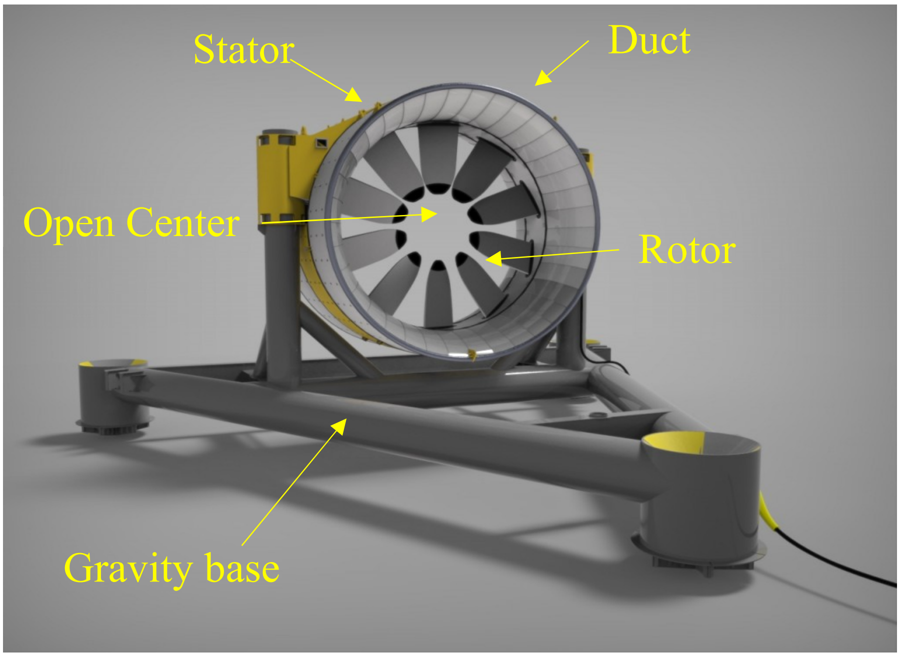

Figure 3-8. Overview of the Rim-driven marine current turbine generator [© Open-hydro].

It is notable that such structure as shown in Fig. 3-8 is novel and fit the characteristics of marine current. However, such structure may lead to heavy weight by putting the generator on the periphery of blades with diameter about 18 meters. Based on such background, this study proposes a novel structure as shown in the following chapter IV and chapter V.

References

[1] Renewables 2017 Global Status Report. *REN21*. Available: http://www.ren21.net/wp-content/uploads/2017/06/GSR2017_Full-Report.pdf. Accessed on: June 22, 2017.
[2] J. Huckerby, H. Jeffrey and B. Jay, "An international vision for ocean energy (Phase 1)," 2011.
[3] AbuBakr S. Bahaj. (2013, Jan.) "Marine current energy conversion: the dwan of a new era in electricity production," *Phil Trans Soc A*. Available: http://dx.doi.org/10.1098/rsta.2012.0500.
[4] M. Watchorn, T. Trapp and AAM. Sayigh, "Tidal Stream Renewable Offshore Power Generation (TS-Ropg)," *The Energy for the 21st Century World Renewable Energy Congress VI 1–7*, Brighton, UK. pp. 2664–2667, 2000.
[5] A. MacGillivray, H. Jeffrey, C. Hanmer, D. Magagna, A. Raventos and A. Badcock-Broe, "Ocean energy technology: gaps and barriers," 2013.
[6] C. Frid, E. Andonegi, J. Depestele, A. Judd, D. Rihan, S. I. Rogers and E. Kenchington, "The environmental interactions of tidal and wave energy generation devices," *Environ Impact Assess Rev*. vol. 32, no. 1, pp. 133–139, Jan. 2012, Available: http://dx.doi.org/10.1016/j.eiar.2011.06.002.
[7] A. Copping, H. Battey, J. Brown-Saracino, M. Massaua and C. Smith. "An international assessment of the environmental effects of marine energy development," *Ocean & Coast*

Manag. vol. 99, pp. 3–13, Oct. 2014, Available: http://dx.doi.org/10.1016/j.ocecoaman.2014.04.002.

[8] S. J. Wang, P. Yuan, D. Li and Y. H. Jiao, “An overview of ocean renewable energy in China,” Renew. Sustainable Energy Rev. vol. 15, no. 1, pp. 91-111, Jan. 2011, Available: https://doi.org/10.1016/j.rser.2010.09.040

[9] L. Drouen, J. F. Charpentier, E. Semail and S. Clenet, “A Global Approach for the Design of a Rim-Driven Marine Turbine Generator for Sail Boat,” Presented at 2012 XXth International Conference on Electrical Machines, Available: DOI: 10.1109/ICElMach.2012.6349923

[10] S. Xu, H.F. Wang and G.B. Hu, “Analysis of Temperature Distribution for the Electric Generator in Rim-Driven Marine Current Power System,” Presented at 2013 International Conference on Electrical Machines and Systems, Available: DOI: 10.1109/ICEMS.2013.6713141.

[11] M. Watchorn, T. Trapp and AAM. Sayigh, “Tidal Stream Renewable Offshore Power Generation (TS-Ropg),” *The Energy for the 21st Century World Renewable Energy Congress VI 1–7*, Brighton, UK. pp. 2664–2667, 2000.

[12] http://bbs.voc.com.cn/topic-5864956-1-1.html.

[13] C. Frid, E. Andonegi, J. Depestele, A. Judd, D. Rihan, S. I. Rogers and E. Kenchington, “The environmental interactions of tidal and wave energy generation devices,” *Environ Impact Assess Rev*. vol. 32, no. 1, pp. 133–139, Jan. 2012, Available: http://dx.doi.org/10.1016/j.eiar.2011.06.002.

[14] UK Renewable Energy Roadmap: 2013 Update. Department of Energy & Climate Change, 2013.

[15] J. Shankleman. “OpenHydro to Supply Japan’s First Commercial Tidal Project,” Jun. 2016, https://www.bloomberg.com/news/articles/2016-07-26/openhydro-to-supply-japan-s-first-commercial-tidal-project. Accessed on June 22, 2017

[16] https://www.atlantisresourcesltd.com/wp/wp-content/uploads/2016/08/SeaGen-Brochure.pdf

[17] http://www.andritzhydrohammerfest.co.uk/tidal-turbines/. Accessed on: June 22, 2017.

[18] http://www.openhydro.com/Technology/Open-Centre-Turbine. Accessed on: June 22, 2017.

CHAPTER IV

Electrical design of 1 MW HTS salient-pole marine current turbine generator

To utilize the marine current energy more efficiently, high rated output power for a unit generator is highly needed at MW level. HTS technology is treated as a promising solution thanks to the superior current-carrying ability and trapped flux performance. In the following chapters IV and V, the design study for marine current turbine generator (MCTG) is introduced. In chapter IV, a conceptual structure of 1 MW MCTG is proposed. The design and optimization procedures, models and specifications that facilitate the MCTGs using HTS windings as field poles are studied. The design starts from analytical equations and then optimizes the electromagnetism calculation based on 3D FEM simulation, where good agreements are achieved finally. Meanwhile, the influence of number of poles and the confinement of outer diameter, etc., on the generator performance are clarified. 32 have been adopt for the optimum number of poles when the outer diameter is confined to 4 m. It is concluded that multi-pole synchronous generator can provide a promising solution for the future MCTG.

4.1 Conceptual structure of HTS salient-pole generator

Increasing anxiousness about the shortage of fossil fuel are igniting the desire to explore sustainable energy such as wind power, solar photovoltaic, biomass energy, geothermal power, ocean energies [1,2]. Encouraged by the success achieved in wind power utilization, researchers and engineers aspire to duplicate the success to marine current energy utilization, one principal type of ocean energies, due to the similarities of the flowing medium - wind and sea water [3]. Furthermore, marine current is about 800 times the density of air and highly predictable up to 98% accuracy for decades, making it possible to utilize marine current energy in a more efficient and predictable form [4]. Whereas, marine current energy utilization possesses its own obstacles and difficulties such as bio-fouling, flow alteration, sedimentation and socio-economic impacts requiring interdisciplinary cooperation among oceanographers, electrical engineers and policy-makers etc. [5-8]. Under such backgrounds, R&D progress of marine current energy conversion are being busily carried out in many countries especially with long coastlines such as China, Japan, UK and France [9-11].

MCTG is an off-shore device to harness the kinetic energy carried by the current flow and then drive the turbine blades, which then supplies the input power to the connected generator. Till now, some wind turbine generator technologies have been directly applied to the MCTGs [12-14]. With deeper understanding of marine current energy characteristics, oscillating hydrofoil systems and rim-driven marine current technology have been developed and adopted recently [15,16]. Notably, the innovative design of direct-driven Open-Center Turbine® (OpenHydro) has won them the contract to supply Japan’s first commercial tidal array project [10], which illuminates the future development of MCTGs.

Due to the high energy-density and relatively low speed, direct-drive synchronous generator fully match the marine current and would become the future trend. In the 1MW Open-Center Turbine, low speed PM synchronous generator is adopted. The generator module locates at the periphery of the turbine blades with PM field pole is integrated with the turbine blade and the armature windings are fixed with the outside stationary support structure. With turbine blade diameters at 18~24 meters level, the weight of a 1 MW MCT unit is reported to be 300 to 450 tons without subsea base, which may bring difficulties during manufacture and assembling.

Here, this paper inspired from the OpenHydro proposes a new concept structure for MCTG and develops a design and optimization method for the generator module as shown in Figs. 4-1 and 4-8. The rotor is directly driven by the turbine blades and the stator is fixed to a stationary support structure. Notably, the generator is set in the inner side of the blade. Hence, significant reduction of generator weight and size can be expected compared with rim-driven technology.

Generally, the global design of a MCTG system should include the generator module, the turbine module, the thermal module, the anti-fouling module, the noise & vibration module, the environmental impacts module and the life cycle assessment module, etc. [3, 17-19]. Designers should utilize sufficient parameters to decide and evaluate the model based on analytical methods, including the size, weight, electrical load, leakage coefficient, power loss etc. [20]. Next, different optimization algorithm can be employed to achieve the specific design targets. Different optimizations based on varied objectives are studied and published. To minimize the costs and losses, low speed permanent magnet machines are analysis in [21]. In [22], an optimization tool is proposed from the aspects of electromagnetic and structural design of wind turbines. Surface mounted and flux-concentrating ferrite PM generators were analyzed and compared integrated with multi-objective functions in [23]. To save the usage of PM materials, the design and optimization algorithm was proposed considering varied rotor structures in [24].

To design a generator, it is often necessary to perform iterations to meet specifications, involving changing some key parameters. Parametric sweep method has been regarded as an efficient and reliable method of solving such problems. Although parametric sweep is efficient at searching optimal combinations of generator parameters over the target region, the credibility can be low if particular parameters cannot be defined accurately. Meanwhile, FEM method is powerful to calculate the magnetic flux distribution including non-linear material properties. Here, to improve the accuracy and reliability of generator design, a combination of parametric sweep and FEM is employed. Firstly, a global search is conducted using parametric sweep analytically. Then, the best candidate is used as initial parameters for FEM simulation to obtain the accurate key parameters. Also, the confinement related to the generator size are included.

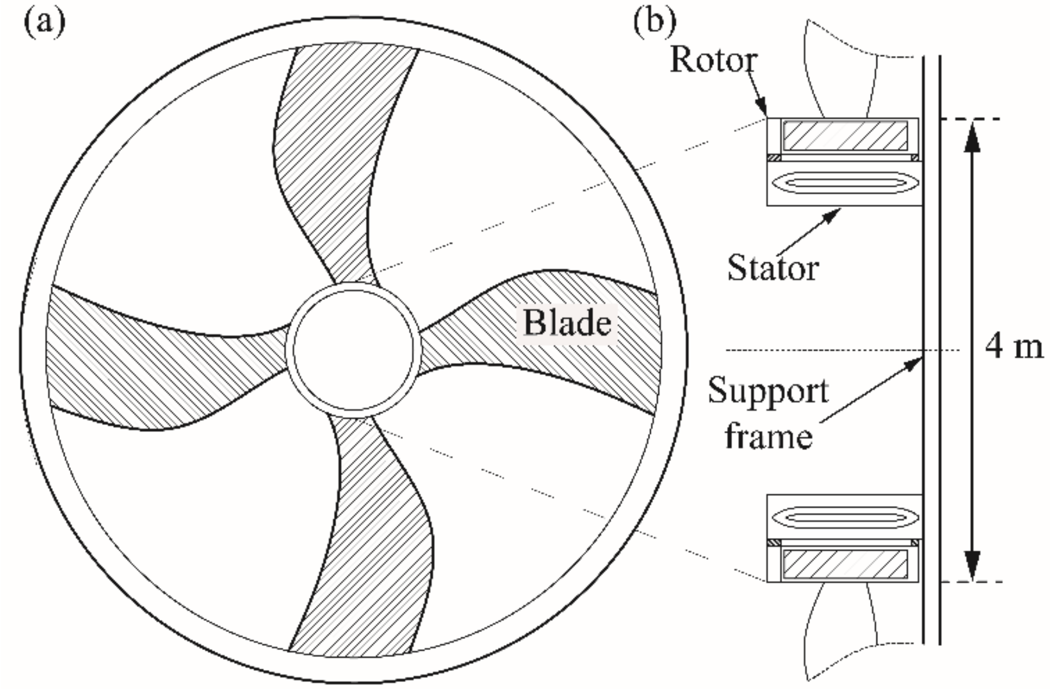

Figure 4-1. Schematic model the proposed MCTG. The generator unit is located at the center of the blades. The outer diameter of the generator unit is decided at 4 meters.

In this chapter, the design and optimization algorithms are studied for a 1 MW HTS MCTG.

A thorough analysis is conducted on the variations of key generator parameters related to the electromagnetism characteristics. The main dimension parameters, including pole numbers, HTS winding parameters are discussed in details. It can be concluded that the proposed generators are promising for the future MCTGs.

4.2 Working conditions of marine current turbine generator

Marine current source characteristics

The MCTG aims to convert the kinetic energy of current into electric energy and the extractable power through the closed surface A_{T} by the turbine blades, namely maximum input power for the generator, can be ideally given by

$$P_T = \frac{1}{2}\rho A_T V^3 C_p \qquad (4-1)$$

where the ρ is the density of marine current and V is the average marine current speed, $A_T = \pi\ r_{blade}^2$ is the swept area by turbine blades and C_P is the power coefficient determined on the hydrodynamic performance of turbine blades and the generator efficiency. To calculate the blade rotation speed, generally, tip ratio speed (TSP) λ is introduced as

$$\lambda = \frac{v_T}{v} = \frac{r_{blade}\ \omega}{v} \qquad (4-2)$$

where v_T is the blade tip speed, v is the average current speed and ω is the angular speed. Referring to the available data for v and λ in [26,27], the design conditions are determined for 1 MW generator design as shown in Table 4-1. Thanks to the development of AC/DC converter technology, it makes possible that the frequency of generator can be decoupled from the electric grid, which fits the requirement of MW level low speed direct driven synchronous generator for wind power and ocean energy converters [28].

Table 4-1 Design Condition of 1 MW 3-Phase MCTG

Output power (kW)	1000
Rated current speed (m/s)	2.5
Rated speed of turbine blade (RPM)	16
Turbine diameters	18
Outer diameter (mm)	4000 ± 100
Terminal voltage (V)	660
Power factor	1

4.3 Design and optimization of electromagnetic model

In this section, the design method of the electromagnetic model for HTS generator is introduced step by step and summarized in Fig. 4-8. Next, the optimization process and post-process are described.

Determination of magnetic flux for one pole

The output power P_0 of a 3-phase synchronous generator can be ideally expressed as $P_0 = 3V_{ph}I_{ph}cos\theta$, where V_{ph}, I_{ph} and $cos\theta$ represents phase voltage, phase current and power factor, respectively. Here, it is assumed the generators run at unity power factor at rated marine current speed to simplify the design and optimization process. The electromotive force induced per phase is given by the equation shown below [24]

$$V_{ph} = 4.44Kf N\Phi_{Armature} \qquad (4-3)$$

where K is the synthetic factor for the generator, including winding factor and magnetic field in air-gap wave form factor, f is the electrical frequency, N is the number of conductors in series per phase and $\Phi_{Armature}$ is the interlinkage of magnetic flux in armature part for one pole, respectively. In equation 4-3, if the V_{ph}, K, f, N are determined, the flux linkage $\Phi_{Armature}$ can be calculated. Under constant flux linkage $\Phi_{Armature}$, the needed Φ_{Field} provided by the field pole is influenced by the flux leakage and depends on the flux leakage coefficient.

To analytically find out the magnetic flux linkage in field pole and air-gap, two leakage coefficients are employed as σ_1 and σ_2. Here, $\sigma_1 = \Phi_{Field}/\Phi_{Armature}$ and $\sigma_2 = \Phi_{Air-gap}/\Phi_{Armature}$, where Φ_{Field} and $\Phi_{Air-gap}$ represents the average flux linkage in field pole and air-gap, respectively. The initial assumed value of leakage coefficient will be defined as $\sigma_{1,0}$ and $\sigma_{2,0}$ and will be modified based on FEM simulations.

Outer diameter confinement of 4m

To accommodate the generator at the inner side of turbine blades, in this study, the outer diameter of the generator is predetermined as 4000 ± 100 mm. Here, the outer diameter of air-gap $R_{air-gap}$ is chosen as the starting point to calculate the radial geometry parameters. Pole pitch τ is defined at the outer diameter of the air-gap expressed as $\pi R_{air-gap} = P\tau$, where P represents the number of poles. Consequent to that, the following target is to find out the optimum combination of the P and τ.

Assuming suitable magnetic flux density in rotor iron-yoke and stator iron-core, integrated with σ_1 and σ_2, the thickness of the stator iron-core, t_{core}, and rotor iron-yoke t_{yoke} can be deduced.

Hence, the governing equations for radial dimensions are expressed as (4-4) for HTS MCTG with the rotor is in the outside part:

$$R_{HTS} = R_{Air-gap} + 2t_{teeth} + 2t_{core} \leq 4000 \pm 100 \ \ (mm) \quad (5-4).$$

where R_{ag}, t_{teeth} and represents the diameter of the outside air-gap and the height of iron-teeth, respectively. The parameters of iron-tooth and slots will be given in the following part.

Parameters of stator tooth and slots

The two generators topologies both adopt laminated iron-core for stator with conventional two-layer distributed copper windings as shown in Fig. 4-2.

In general, the working current density in copper winding will be influenced by the working temperature and cooling efficiency. Here, to make a balance between the copper loss and the usage of copper wires, 3 A/mm^2 is employed. Based on the above parameters and a suitable electric loading of 1000 A/cm, the needed cross-section of armature windings can be calculated. Further, integrated with the insulation materials, the cross-section of teeth and slot can be deduced.

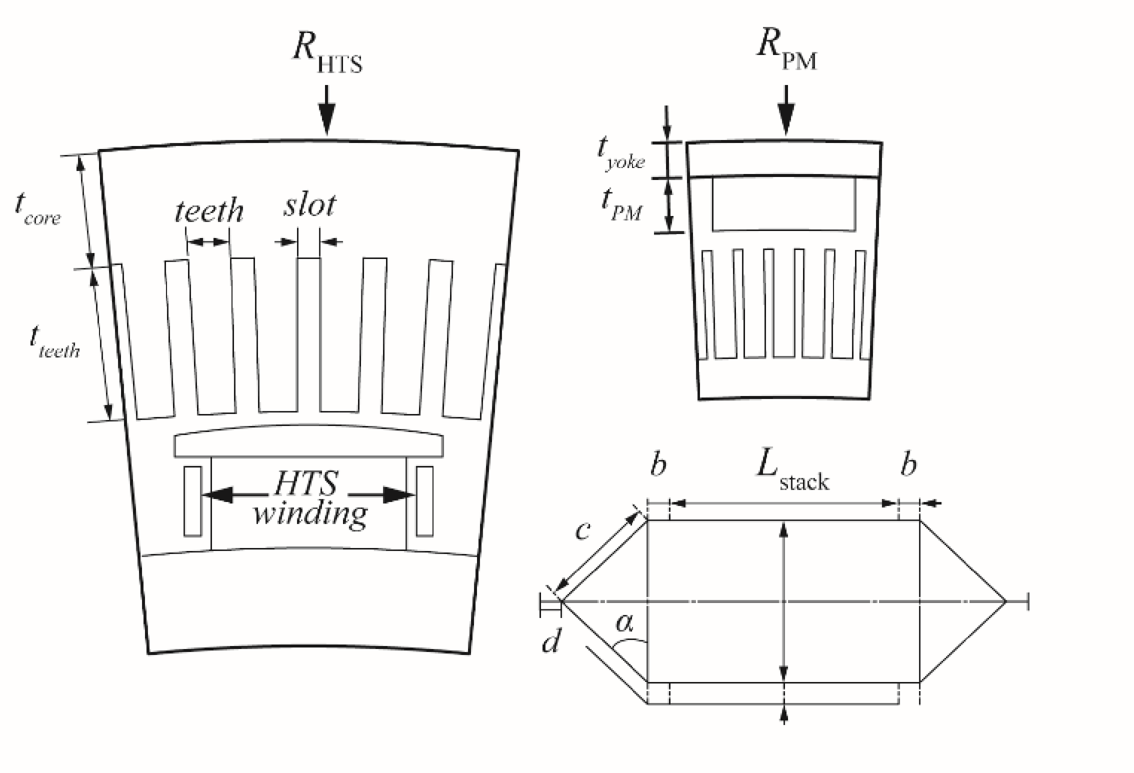

Figure 4-2. Cross section and dimensional parameters of generator rotor and stator. (a) Cross section and corresponding parameters of HTS generator. (b) Cross section and corresponding parameters of PM generator.

Parameters of copper armature winding

To calculate the armature loss, the total length of the armature windings is necessary. For each turn, it is calculated including the linear part, curve part and the edge shape in the following equations

$$L_{one-turn} = 2L_{stack} + 4b + 4c + 4d \qquad (4-5)$$

$$a = (teeth + slot) \times (mN_{pp} - 1) \qquad (4-6)$$

$$\sin\alpha = \frac{w_{coil}}{w_{slot} + w_{teeth}} \qquad (4-7)$$

where L_{stack}, a, b, c, d, α are shown in Fig. 4-2 (c). The resistance of armature windings can be also deduced.

According to the geometry parameters of armature windings and particular known parameters, the leakage reactance can be calculated. Further, the armature reaction reactance under load-condition is estimated.

Magnetomotive force under no-load and load condition

With the above determined parameters, the required *MMF* for stator iron-core, stator teeth, air-region and rotor is calculated considering the *B-H* characteristic of laminated iron-core materials under no-load condition.

Also, the armature reaction is introduced to compensate the required MMF under load condition. The interlinkage of $\Phi_{Armature}$ under load condition and no-load condition is emphasized for the further comparison with the FEM simulation results.

HTS magnetic field pole parameters

To supply the required *MMF*, magnetic field pole with HTS tapes is adopted here. One core problem is to decide the operating condition of HTS tapes. Here, the pole arc/pole pitch for the HTS MCTG employ a same value of 0.73. Therefore, the influence of pole arc to pole pitch ratio is not analyzed.

For HTS winding, cryostat is necessary for the cooling [29]. To reach a balance between the cooling power consumption and cooling time, warm iron-rotor topology is employed at the present step [30]. As shown in Fig. 4-2(a), the gap between HTS winding and the field pole is preset for the future study of the cryostat structure. Here, the electromagnetism and thermal characteristics of the winding are studied to obtain optimized HTS winding parameters. In HTS MCTG, to fully use the merits of HTS winding, the magnetic field density in the field pole is set as the saturation level 2.1 T.

The $J_c(B, \theta, T)$ characteristics of the adopted 2-G HTS tapes can be found in [31]. It is considered the HTS winding is operating at 77K and the maximum rated current density is 460 A/mm^2. Considering the degradation of HTS wires in long length, 300 A/mm^2 is adopt as J_c for the present analysis. Based on the $J(B)$ and $J(\theta)$ variation at 77K, the $J(B,\theta,77K)$ performance is expressed as $J(B,\theta,77K)= J(B,77K)\times J(\theta,77K)$ as shown in Fig. 4-3. The 3D model of the field pole with HTS winding is shown in Figs. 4-9 and 4-10.

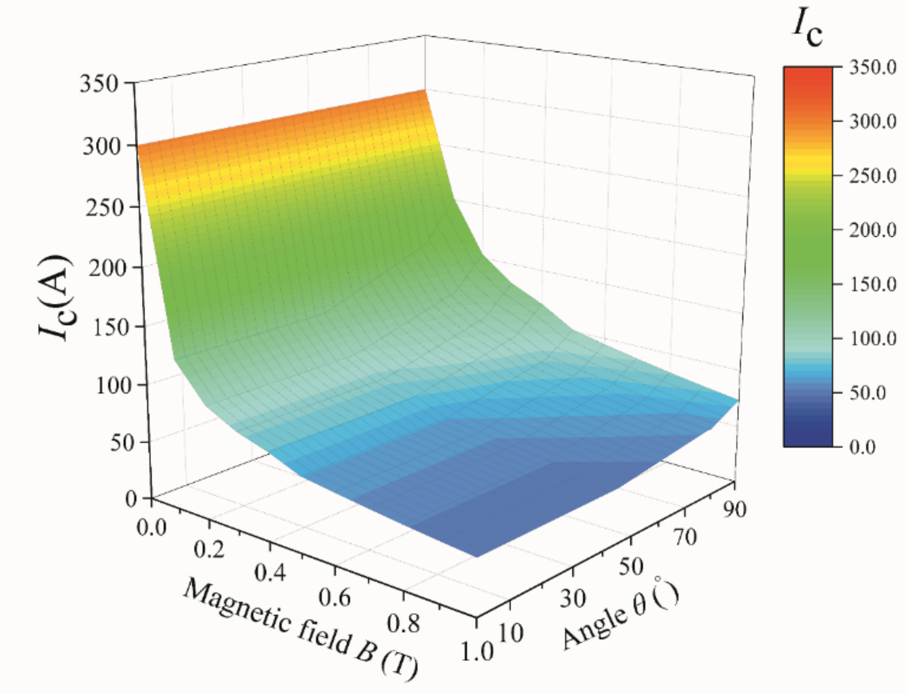

Figure 4-3. At 77K, the J_c (B, θ) variation as a function of the magnitude of B and the orientation of θ with respect to the crystallographic c-axis, where 90° represent the B vector is perpendicular to the c-axis.

Determination of working current and heat generation for HTS field poles

In present HTS application designs, HTS tapes are popularly formed in race-track coil structures, where the magnitude and orientation of local magnetic field varies from point to point. Due to the intrinsic structural characteristics, critical current I_c and n values of HTS, HTS materials show a strong anisotropy. I_c of superconductors continuously decreases with the increasing of magnetic field and temperature. The so-called anisotropy of superconducting materials means that its critical current depends not only on the magnitude of the magnetic field but also on its orientation when the temperature is a constant. HTS has strong anisotropy because it is an oxide ceramic materials with granularity. Thus, the anisotropy of practical superconducting materials is an important parameter which should be carefully considered in the superconducting electrical applications design.

The anisotropic parameter mainly refers to the anisotropy of the critical current I_c under the magnetic field with varying magnitudes and orientations. In addition, transition from a superconducting state to a normal state in a superconductor is generally described by fitting the voltage-current relationship with the power-law relation, in which the power index *n* is called the *n* value, which is used to indicate the transition degree. The larger the *n* value, the more abrupt the transition. The *n* value is generally calculated by fitting current-voltage current of superconductors with the power law model within the range of 0.1 μV/cm $\leq E \leq$ 1 μV/cm as

$$E = E_c \left(\frac{1}{I_c(B,T)}\right)^{n(B,T)} \qquad (4-8)$$

where E_c = 1 μV/cm is the criterion defining the critical current I_c. Critical current $I_c(B,T)$ and *n* value $n(B,T)$ suggests that both are functions of magnetic field *B* and temperature *T*.

As we know, the *n* value of the HTS is much lower than that of the conventional LTS. In general, superconductivity of superconductors with higher *n* values are superior to those with lower *n* value. However, the former quench more easily than the latter. Unlike the LTS, the critical current of the HTS cannot exclusively reflect its current-carrying characteristics; therefore, the *n* value must be considered to evaluate completely the current-carrying properties with zero resistivity. Hence, the critical parameters describing HTS tapes should include the *n* value as well as the critical current or critical current density.

The *n* value is a power index obtained by fitting the voltage-current relationship into magnetic field, the *n* value relates not only to the magnitude but also to the orientation of the magnetic field. Compared with the anisotropy of the critical current in HTS tapes, there are few reports concerning anisotropy of n values of 2G tapes. In the range of a magnetic field lower than 0.5 T, the *n*-value of a 2G tape is nearly independent of magnitude and orientation of the magnetic field verified by experiments. However, it significantly depends on magnitude and orientation of the magnetic field if it is higher than 0.5 T, and there is also no simple analytical and empirical formula in this respect.

In practical applications with HTS coils as magnetic field poles, the main concern during design is not only the spatial magnetic field distribution in the motor/generator frame, but also the vicinity of the field pole which have more serve influence on the current-carrying performance of HTS tapes. Using MagNet 7.7 to simulate in the present study.

HTS tapes parameters used in the present study

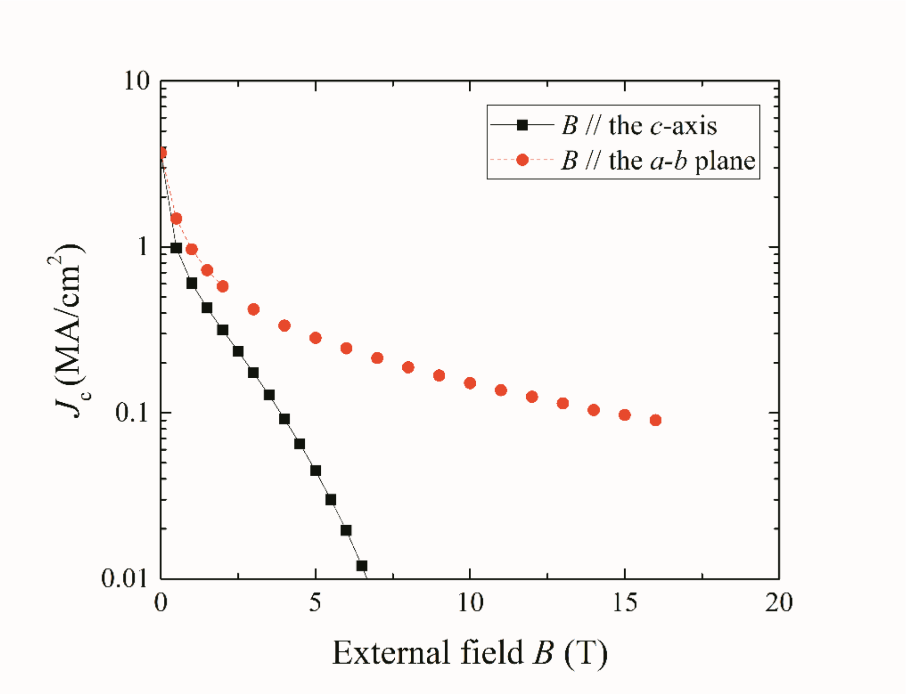

Figure 4-4. Anisotropy of critical current in HTS tapes (YBCO) at 77K.

Fig. 4-4 shows the J_c values as a function of external magnetic field B magnitude when B is parallel to the crystallographic c-axis (B // the c-axis) and B is parallel to the tape surface (B // the a-b plane).

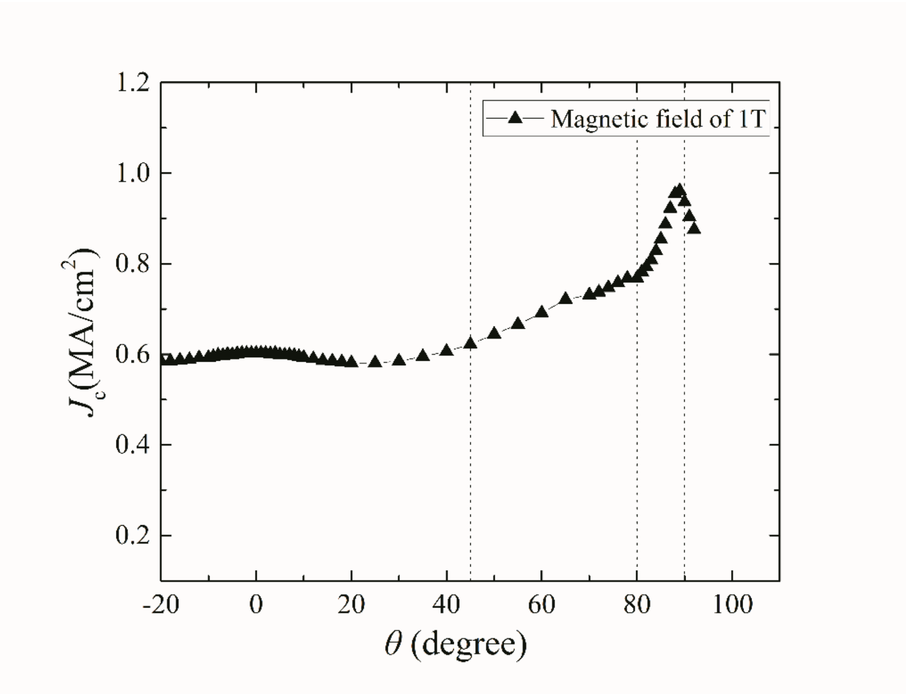

Figure 4-5. Angular dependence of J_c at 1 T under 77K. Here, 0° represent the magnetic field is perpendicular to the tape plane (parallel to the YBCO c-axis), and 90° means the field is parallel to the YBCO tape plane.

Fig. 4-5 shows the J_c variation as a function of the orientation of magnetic field. In the design steps, the current value was divided into three linear changing regions as emphasized in Fig. 4-5, namely, 0º ~ 45º, 45º ~ 80º, 80º ~ 90º. Three critical values $J_c(\theta)$ were chosen for the following characterization (0º, 6.0×10^5 A/cm^2), (45º, 6.0×10^5 A/cm^2), (80º, 7.7×10^5 A/cm^2) and (90º, 9.4×10^5 A/cm^2). Then, the current value was extrapolated as bellows:

$$J_c = \begin{cases} 6.0\times 10^5 \dfrac{A}{cm^2}, & (0^\circ \le \theta \le 45^\circ) \\ (0.04857\times\theta + 3.814)\times 10^5 \dfrac{A}{cm^2}, & (45^\circ \le \theta \le 80^\circ) \\ (0.17\times\theta - 5.9)\times 10^5 \dfrac{A}{cm^2}, & (80^\circ \le \theta \le 90^\circ) \end{cases} \qquad (4-9)$$

Fig. 5-6 shows the J_c dependence of applied field varying from 0T to 1T at 77K. With the increasing of external magnetic field, the current carrying performance will be

In this study, the $J_c(T,\ \theta, B)$ was considered as the following:

$$J_c(T,\ \theta, B) = J_c(T)\times J_c(\theta)\times J_c(B) \qquad (4-10)$$

Basically, the current carrying performance decreases with the increasing of external field and the angle between external field and tape plane. Thus, the J_c (77K, 90º, 0T) can be regarded as the highest value for current carrying ability at 77K.

Under 77K, the magnetic field dependence of I_c can be fitted as

$$I_c = \begin{cases} 446 - 1968.9\times B + 5827.8\times B^2 - 7814.8\times B^3 + 3333.3\times B^4, \\ \qquad (0T \le B \le 0.5T) \\ 216 - 163.2\times B + 72.2\times B^2 - 17.2\times B^3 + 1.6\times B^4, \\ \qquad (0.5T \le B \le 1T) \end{cases} \qquad (4-11)$$

where B is the magnetic field density.

Base on the above analysis, we can deduce the I_c values as a function of varied magnetic field density and the orientation at 77K as shown in Fig. 4-3.

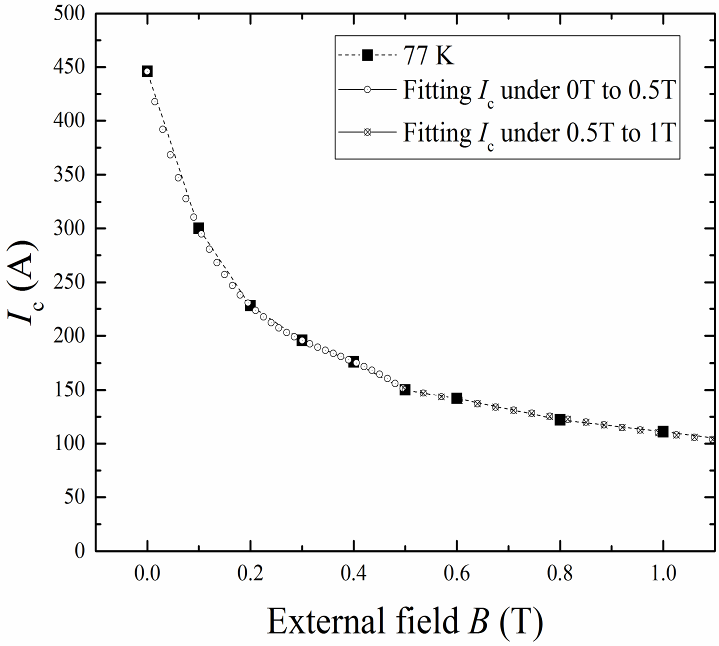

Figure 4-6. Magnetic field density dependence of I_c at 1T under 77K. The magnetic field is applied parallel to the YBCO tape plane.

Generator weight, loss and efficiency

Following the determined parameters, the weight of each part of the generator can be calculated. Also, loss of generator is also estimated including the iron loss, armature resistance loss, stray loss, mechanical loss, and the cooling loss. Thus, the total loss and efficiency of HTS MCTG can be obtained.

Determination of machines parameters

Based on the above analytical analysis, the preliminary parameter scanning can be finished and the parameters scanning results for HTS MCTG are shown in Fig. 4-7. Then, the best individual is selected for the following FEM optimization as shown in Fig. 4-8.

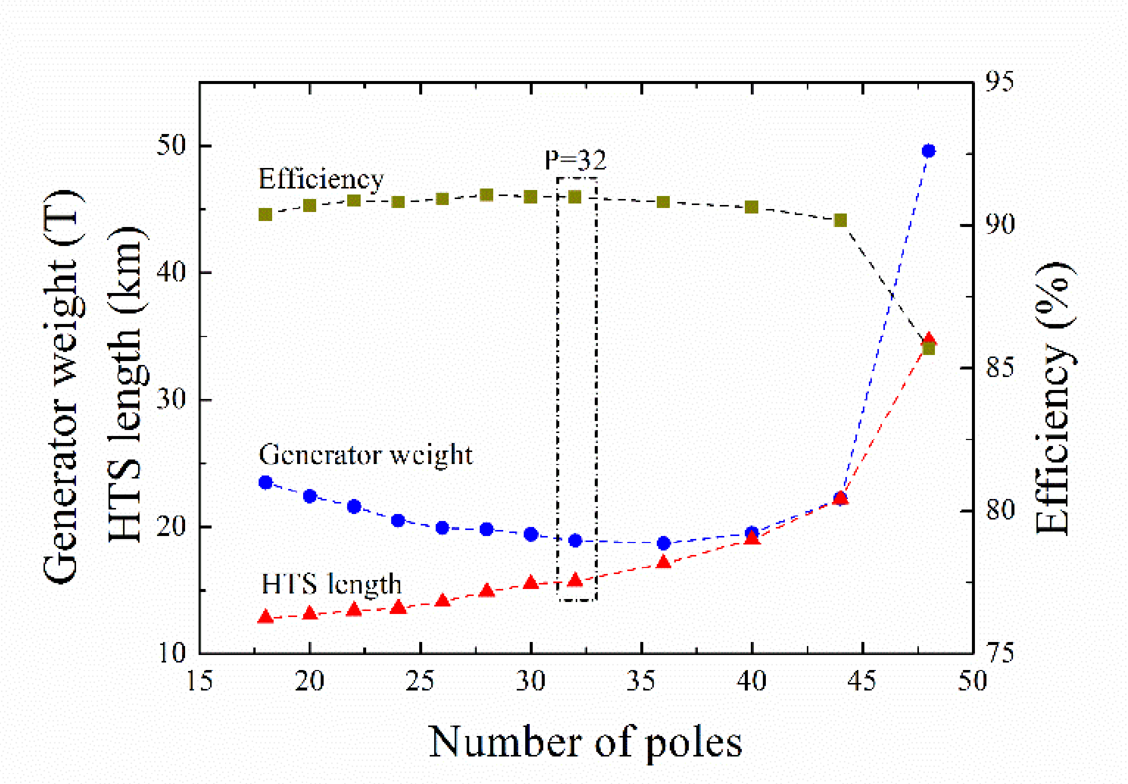

Figure 4-7. Generator weight, efficiency, HTS length as a function of the number of poles.

Since the outside diameter is confined, the increasing number of poles will result in reduced pole pitches and shorten magnetic circuit within the adjacent pair of magnetic poles. Then, it can reduce the usage of the iron-core materials and reduce the generator weight, which is well agreed with the design results. In this study, warm rotor structure is adopted and the distance between HTS windings and the field pole is predetermined for each case, if the pole pitch is too small, it makes the HTS race-track winding thin in x direction and tall in y direction as shown in Fig. 4-9. Thus, to some extent, the generator weight will increase with the increasing of P, which can be explain the sharp increasing when P is larger than 44. Meanwhile, it can be seen, the HTS length also increases gradually due to the increasing of end winding length, which causes a waste of HTS wires. Thanks to the superior current-carrying performance and low DC heat loss, the efficiency is over 90% in nearly the whole range, which shows the advantage over PM MCTGs. Hence, based on the weight, efficiency and HTS length, 32 is chosen for the following optimization.

Parameters of best candidate based on analytical model

Till now, the best candidates among two generator topologies for further optimization can be decided. The geometrical parameters for the 3D modeling are listed in Table 5-2.

Optimization

In the optimization process, a commercial software of MagNet (Infolytica Inc.) is utilized to calculate the spatial magnetic flux distribution. Through simulation, the magnetic flux vector B_x, B_y and B_z as shown in Figs. 4-8 and 4-9, which represents the magnetic flux density in x, y and z direction, can be obtained and are used to calculate the flux leakage coefficient.

Table 4-2 Basic Parameters and Operation Characteristics of 1 MW Class HTS MCTG

Physical Dimensions and Design Parameters	HTS Type
Number of poles	32
Initial leakage coefficient $\sigma_{1,0}$	1.26
Initial leakage coefficient $\sigma_{2,0}$	1.12
Outer diameter [mm]	4021
Inner diameter [mm]	2987
Generator effective axial length [mm]	380

As shown in Fig. 4-8, the main function of the FEM is to determine the accurate leakage coefficient σ. Meanwhile, the magnetic flux vector in the HTS winding region is used to calculate the heat loss and determine the working current of HTS windings.

Modification of leakage coefficient

In the simulation, the B-H curve of the laminated iron material are the same with [32]. The generators are modelled in steady states under no-load condition to get the optimum geometries. Two critical conditions are defined as teeth center condition and slot center condition, where the centerline of one teeth and one slot coincides with the centerline of the corresponding field pole along the radially direction, respectively. The average value of calculated σ under slot center case and teeth center case were chosen as the calculated leakage coefficient.

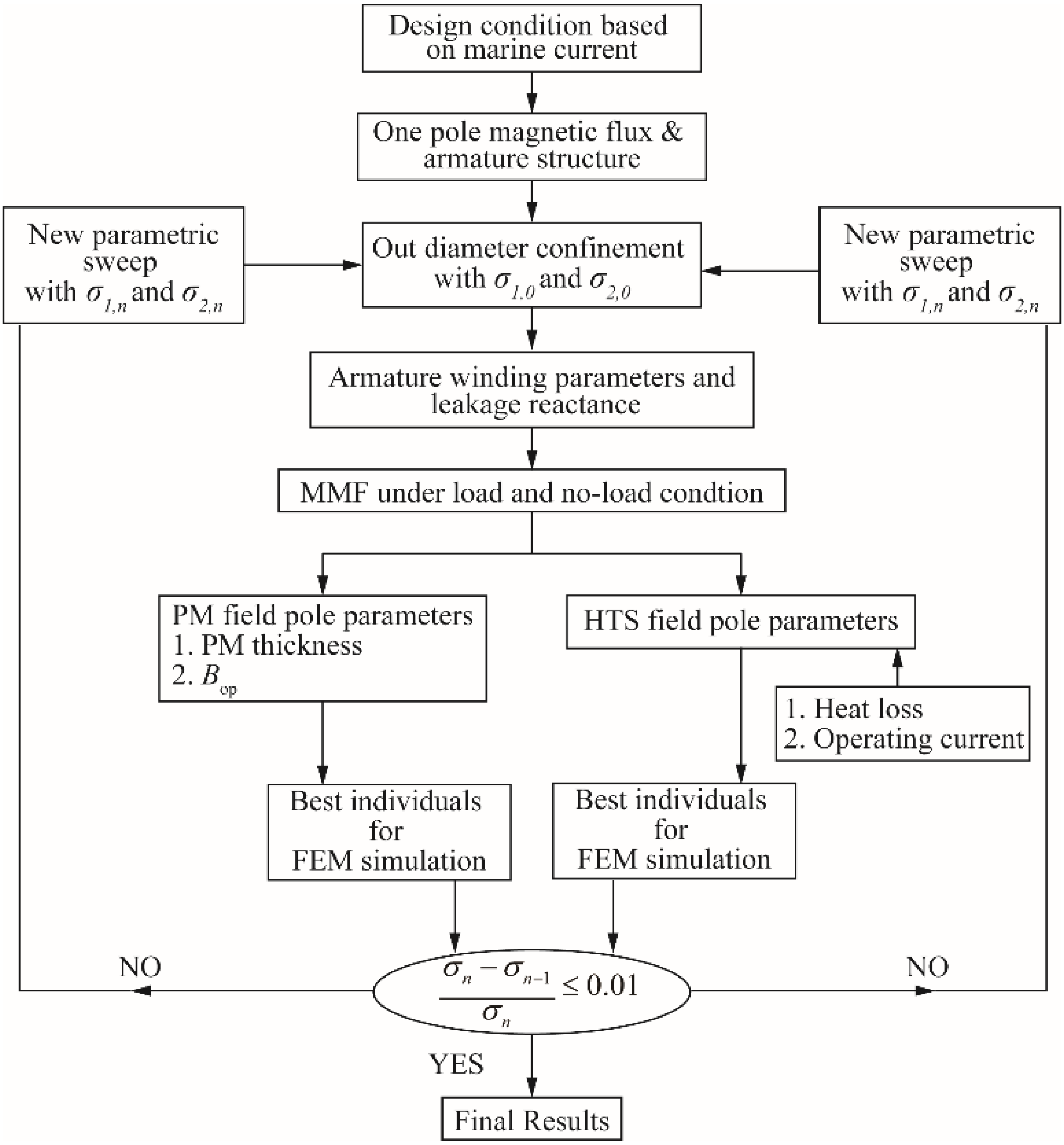

Figure 4-8. Design and optimization flow chart for the MCTG generator with PM and HTS magnetic field poles.

In Figs. 4-9, (a) and (b) represent the slot center case and the teeth center case of the HTS MCTG. Thanks to the utilization of iron-core, the magnetic flux is mainly confined in the iron materials. Y-axis is along the generator radial direction. To calculate the flux linkage in field pole and stator pole, they are divided into 5 equal segments along the Y-axis, then Φ is the integration of local B_y and the corresponding cross-section area.

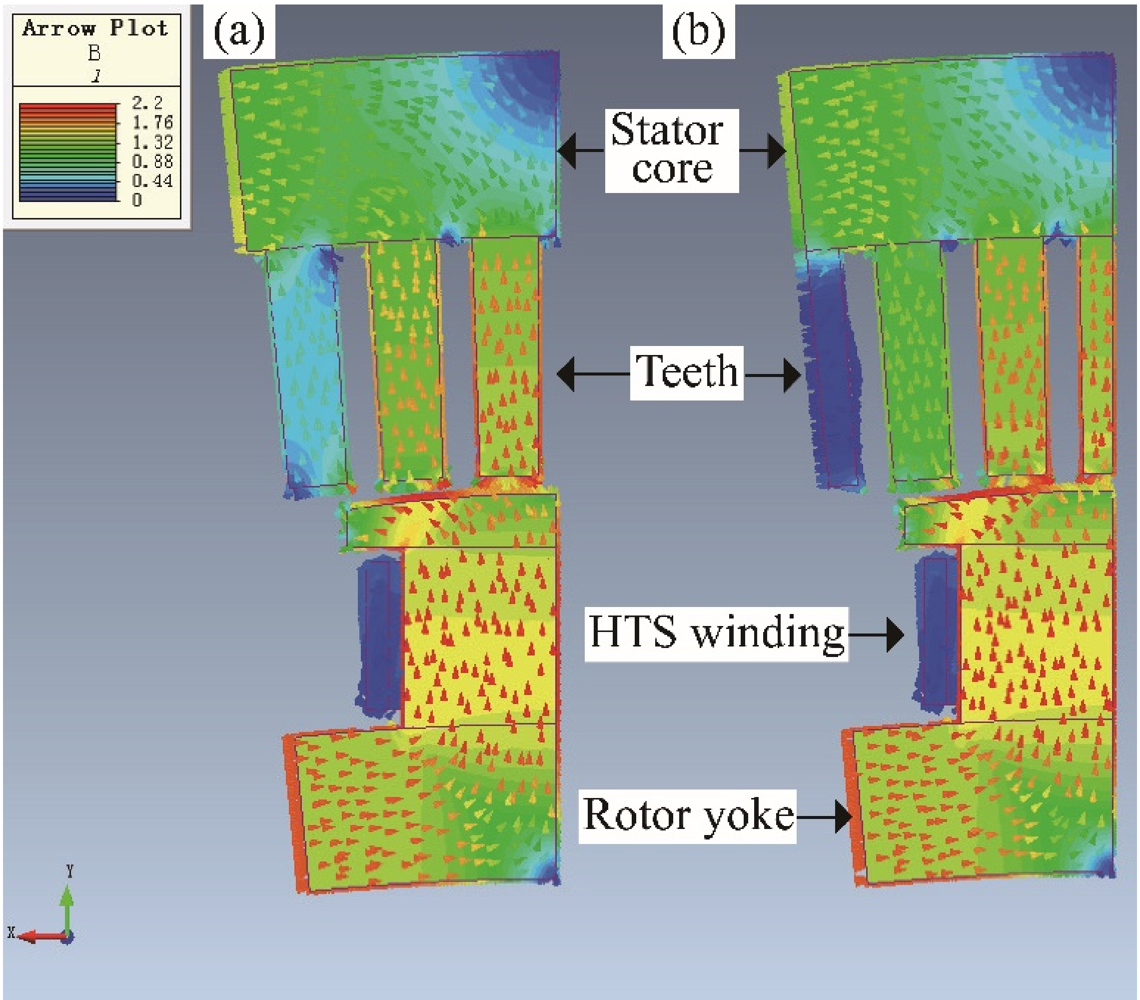

Figure 4-9. Magnetic flux distribution in the cross section of the proposed HTS MCTG (Half-model of one magnetic pole). (a) The steady case of slot center case. (b) The steady case of teeth center case.

Calculation of DC heat loss

In a HTS generator, rotating coils as field poles, cooled below typical critical temperature, are normally excited with direct current to magnetize the generator at a field current level which varies with the working load. The dominating operational limits on a superconducting generator coil current are related to thermal issues. Under steady-state, the coil heat generation from electromagnetic effects must be not drive the heat load over the cryogenic refrigeration capacity and cooling system must assure a return to a stable post-transient operating condition. Specifically, the HTS coil heat generation is expected to include the flux flow regime losses, as described by the *n* value of the HTS material. One of key considerations for HTS generator design concerns the magnitude and nature of coils heat losses under steady state. A DC loss model is using the current-carrying characteristics, YBCO critical surface data, and the race-track coil magnetic field profiles. YBCO critical surface data under 77K are illustrated in the above section. Here, the calculation algorithm of heat loss and 3-D simulation of magnetic flux distribution using MagNet is explained. The DC loss under different working current is the integration of the dissipation power density *J•E* in the whole superconducting field coil volume, where *J* is the current density and *E* is the electrical field.

For practical superconducting wires, the transition is not infinitely sharp but gradual. In this case, I_c is defined as the current where the voltage across the wire becomes greater than a specific electric field (E_c), usually 1.0 μV/cm in self-field at 77K.

$$E(I) = E_c\left(\frac{I}{I_c}\right)^n \qquad (4-12),$$

where $E(I)$ is the longitudinal voltage drop across the superconductor, E_c is the electric field criterion at 1.0 μV/cm, I is the current in the conductor, I_c is the critical current and n is the exponent.

The electric loss along the HTS coils can be expressed as the following:

$$P = EI \qquad (4-13),$$

where I is the operating current, E is the longitudinal voltage drop along the HTS coils length. Thus, based on equations 4-12 and 4-13, the DC heat loss can be defined as

$$Q = EI = E_c\left(\frac{I}{I_c(B,\theta)}\right)^{n(B,\theta)} I \qquad (4-14).$$

Here, I is the operating current, $I_c\ (B, \theta)$ and $n\ (B, \theta)$ are the critical current and n vale at local magnetic field density B and magnetic field orientation θ. E_c is the criterion electric field of 1.0 μV/cm.

Total DC electric loss Q_{total} of the HTS field winding can be calculated by integrating the local heat loss along the total length of HTS wires using equation 4-14. Thus, for the total heat loss of race-track coils is expressed in the following equation 4-15.

$$Q_{total} = \sum_{x,y,z}\left\{E_c\left(\frac{I}{I_c(B,\theta)}\right)^{n(B,\theta)} I\Delta x\Delta y\Delta z\right\}$$
$$+ \sum_{y,r,\varphi}\left\{E_c\left(\frac{I}{I_c(B,\theta)}\right)^{n(B,\theta)} Ir\Delta x\Delta y\Delta z\right\} \qquad (4-15)$$

Here, x, y and z are width, thickness and length of the HTS coil; r and φ are the radius and angle of the HTS coil.

The dominating operational limits on a HTS winding are related to thermal issues. Under steady-state, the coil heat generation from electromagnetic effects must be not drive the heat load over the cryogenic refrigeration capacity and cooling system must assure a return to a stable post-transient operating condition. The heat loss under DC model is analyzed based on the YBCO critical current data and the magnetic field profiles of race-track winding as shown in Figs. 4-9 and 4-10. Here, $E_c = 1.0\mu V/cm$ is set as the critical electric field and 21 is adopt to represent the n-value.

The current-carrying performance will be degraded influence by the external magnetic field. Here, iron-core magnetic pole is adopted and the magnetic flux is mainly confined in the iron region. Thus, the local magnetic flux density within the HTS winding is assumed below 0.5 T to determine the initial $I_0 = 300\text{A}\times 0.35 = 105\text{A}$. Another limitation comes from the cooling power consumption, where 100W is chosen as the maximum heat loss in DC mode for HTS winding. As shown in the Fig. 40, the magnetic flux nearly parallel to the HTS tape in the center part along y direction, whereas the orientation of magnetic flux tends to perpendicular to the HTS tape surface in the edge of y direction, where the degradation of current-carrying performance more obviously.

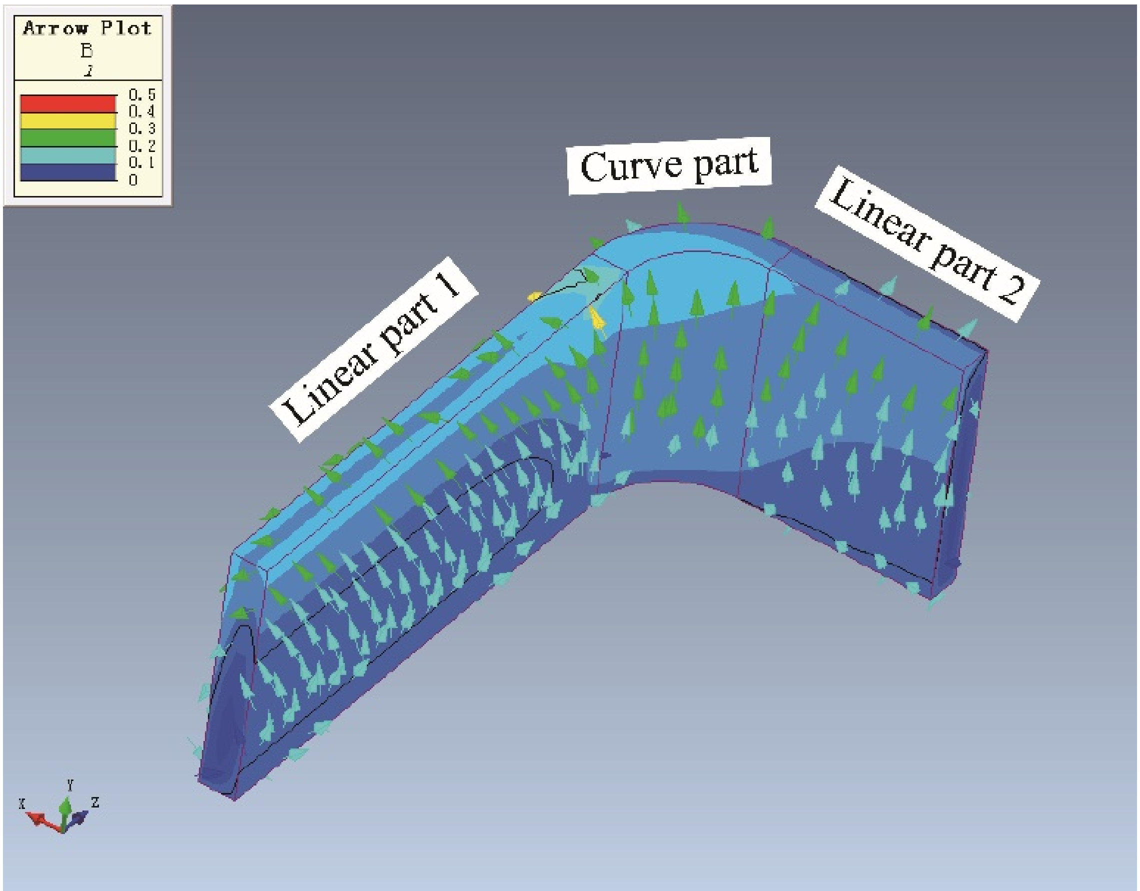

Figure 4-10. Magnetic flux distribution for the HTS winding

It can be seen from Fig. 4-10, HTS windings are divided into linear part 1, linear part 2 and curve part, where the B_x, B_y and B_z are extracted using Cartesian and cylindrical coordinate, respectively. Δx Δy Δz $\Delta\varphi$

Meanwhile, the magnetic flux density is less than 0.5 T, which verifies our assumption for the setting of I_0 is acceptable. The heat loss can be obtained by the following equation:

$$Q_{total} = \sum_{x,y,z} \left\{ E_c \left(\frac{I}{I_c(B,\theta)} \right)^{n(B,\theta)} I\Delta x \Delta y \Delta z \right\}$$

$$+ \sum_{y,r,\varphi} \left\{ E_c \left(\frac{I}{I_c(B,\theta)} \right)^{n(B,\theta)} Ir\Delta x \Delta y \Delta \varphi \right\} \qquad (4-16)$$

As seen from Fig. 4-11, the maximum allowable current is 88 A to satisfy the heat generation limitation. Also, safety margin is introduced as a load factor of 0.85. Thus, the working current is determined as 74.8 A.

In the analytical calculation, the needed $\Phi_{Armature}$ is 0.1043 Wb and reached 0.1101 Wb, which shows good agreements and verify the accuracy of the present design algorithm.

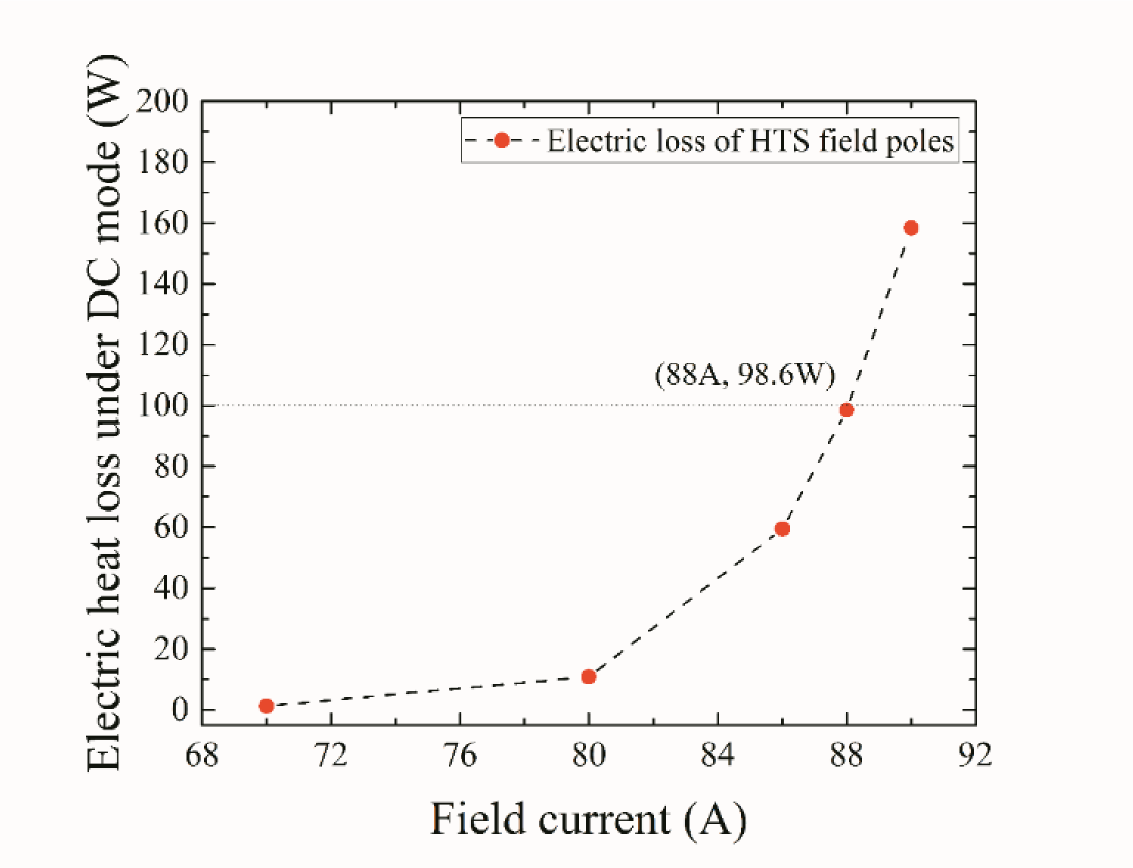

Figure 4-11. Electrical heat loss of HTS field poles as a function of working current.

4.4 Design results of HTS generator

The proposed generator topology is verified to be feasible for MCTGs. The final design results for HTS MCTGs are listed in Table 5-3, which can be mainly summarized as following. At the rated output power of 1 MW, HTS topology is promising for the future MCTG. The comparison of HTS and PM generators will be given in following chapter.

Table 4-3 Generator Parameters for HTS MCTG

Final design results	HTS MCTG
Number of poles	32
Pole pitch [mm]	340
Mean air gap length [mm]	12
Outer diameter of generator (R_o) [mm]	4012
Inner diameter of generator (R_i) [mm]	2995
Generator effective axial length (L) [mm]	358
No-load MMF/Field pole [kA/Field pole]	22.6
Load MMM/Field pole [kA/Field pole]	27.8
Rotor weight [t]	4.9
Armature loss [kW]	60.2
Iron loss [kW]	5.6
Total loss [kW]	87.9
Efficiency [%]	91.9
Weight [t]	16.1

4.5 Conclusions

In this chapter, the electromagnetic design and optimization of 1 MW level MCTGs with HTS field windings was studied. The proposed design models were presented and the generator characteristics were studied based on analytical method and then optimized with FEM simulation. It is considered that multi-pole ring-type MCTGs are feasible form the point of the electromagnetic design. Meanwhile, with high efficiency, such type generators can provide a promising solution for the future MCTGs. 32 has been adopt for the optimum number of poles when the outer diameter is confined to 4 m. Lastly, the hugely reduction in weight compared with MCT is attractive.

References

[1] Renewables 2017 Global Status Report. *REN21*. Available: http://www.ren21.net/wp-content/uploads/2017/06/GSR2017_Full-Report.pdf. Accessed on: June 22, 2017.

[2] J. Huckerby, H. Jeffrey and B. Jay, “An international vision for ocean energy (Phase 1),” 2011.

[3] AbuBakr S. Bahaj. (2013, Jan.) “Marine current energy conversion: the dwan of a new era in electricity production,” *Phil Trans Soc A*. Available: http://dx.doi.org/10.1098/rsta.2012.0500.

[4] M. Watchorn, T. Trapp and AAM. Sayigh, “Tidal Stream Renewable Offshore Power

Generation (TS-Ropg)," *The Energy for the 21st Century World Renewable Energy Congress VI 1–7*, Brighton, UK. pp. 2664–2667, 2000.

[5] A. MacGillivray, H. Jeffrey, C. Hanmer, D. Magagna, A. Raventos and A. Badcock-Broe, "Ocean energy technology: gaps and barriers," 2013.

[6] C. Frid, E. Andonegi, J. Depestele, A. Judd, D. Rihan, S. I. Rogers and E. Kenchington, "The environmental interactions of tidal and wave energy generation devices," *Environ Impact Assess Rev*. vol. 32, no. 1, pp. 133–139, Jan. 2012, Available: http://dx.doi.org/10.1016/j.eiar.2011.06.002.

[7] J. Abanades, D. Greaves and G. Iglesias, "Wave farm impact on beach modal state," *Mar. Geol.*, vol. 361, no. 1, pp. 126–135. Mar. 2015, Available: http://dx.doi.org/10.1016/j.margeo.2015.01.008.

[8] A. Copping, H. Battey, J. Brown-Saracino, M. Massaua and C. Smith. "An international assessment of the environmental effects of marine energy development," *Ocean & Coast Manag*. vol. 99, pp. 3–13, Oct. 2014, Available: http://dx.doi.org/10.1016/j.ocecoaman.2014.04.002.

[9] S. J. Wang, P. Yuan, D. Li and Y. H. Jiao, "An overview of ocean renewable energy in China," *Renew. Sustainable Energy Rev.* vol. 15, no. 1, pp. 91-111, Jan. 2011, Available: https://doi.org/10.1016/j.rser.2010.09.040

[10] J. Shankleman. "OpenHydro to Supply Japan's First Commercial Tidal Project," Jun. 2016, https://www.bloomberg.com/news/articles/2016-07-26/openhydro-to-supply-japan-s-first-commercial-tidal-project. Accessed on June 22, 2017

[11] UK Renewable Energy Roadmap: 2013 Update. Department of Energy & Climate Change, 2013.

[12] http://www.andritzhydrohammerfest.co.uk/tidal-turbines/. Accessed on: June 22, 2017.

[13] http://www.andritzhydrohammerfest.co.uk/tidal-turbines/. Accessed on: June 22, 2017.

[14] http://www.tidalstream.co.uk/. Accessed on: June 22, 2017.

[15] http://www.eel-energy.fr/en/eel-tidal-energy-convertor/. Accessed on: June 22, 2017.

[16] http://www.openhydro.com/Technology/Open-Centre-Turbine. Accessed on: June 22, 2017.

[17] L. Drouen, J. F. Charpentier, E. Semail and S. Clenet, "A Global Approach for the Design of a Rim-Driven Marine Turbine Generator for Sail Boat," Presented at 2012 XXth International Conference on Electrical Machines, Available: DOI: 10.1109/ICElMach.2012.6349923

[18] L.D. Chambers, K.R. Stokes, F.C. Walsh and R.J.K. Wood, "Modern approaches to marine antifouling coatings," *Surface & Coatings Technology.* vol. 201, no. 6, pp. 3642–3652, Dec. 2006, Available: https://doi.org/10.1016/j.surfcoat.2006.08.129.

[19] S. Xu, H.F. Wang and G.B. Hu, "Analysis of Temperature Distribution for the Electric Generator in Rim-Driven Marine Current Power System," Presented at 2013 International Conference on Electrical Machines and Systems, Available: DOI: 10.1109/ICEMS.2013.6713141.

[20] D.C. Aliprantis, S.D. Sudhoff and B.T. Kuhn, "Genetic algorithm-based parameter identification of a hysteretic brushless exciter model," *IEEE Trans. Energy Convers.*, vol. 21, no. 1, pp. 148-154. Mar. 2006, Available: DOI: 10.1109/TEC.2005.847967.

[21] S. Alshibani, V. G. Agelidis and R. Dutta, "Lifetime Cost Assessment of Permanent Magnet Synchronous Generators for MW Level Wind Turbine," *IEEE Trans. Sustain. Energy*, vol. 5, no. 1, pp 10-17, Jan., 2014, Available: DOI: 10.1109/TSTE.2013.2271781.

[22] T. Bazzo, J. F. Kolzer, R. Carlson, F. Wurtz and L. Gerbaud, "Optimum design of a high-efficiency direct-drive PMSG," Presented at Energy Conversion Congress and Exposition, 2015, Available: DOI: 10.1109/ECCE.2015.7309921.

[23] A. Zavvos, A. Mcdonald and M. Mueller “Optimization tools for large permanent magnet generators for direct drive wind turbines,” *IET Renewable Power Generation*, vol. 7, no. 2, pp. 163-171, May 2013, Available: http://dx.doi.org/10.1049/iet-rpg.2012.0135.

[24] A. McDonald and N. A. Bhuiyan, “On the optimization of generators for offshore direct drive wind turbines,” *IEEE Trans. on Energy Convers*., vol. 32, no. 1, pp. 348-358, Mar. 2017, Available: DOI: 10.1109/TEC.2016.2624219.

[25] H. W. Fang and D. Wang, “A novel design method of permanent magnet synchronous generator from perspective of permanent magnet material saving,” *IEEE Trans. on Energy Convers*., vol. 32, no. 1, pp. 48-54, Mar. 2017, Available: DOI: 10.1109/TEC.2016.2621133.

[26] J. McNaughton, S. Harper, R. Sinclair and B. Sellar, “Measuring and modelling the power curve of a Commercial-Scale tidal turbine,” in *Proc. 11th EWTEC*, pp. 09A2-1-(1-9), 2015.

[27] S. Nasha and A. Phoenixa, “A review of the current understanding of the hydro-environmental impacts of energy removal by tidal turbines,” *Renew. Sustainable Energy Rev*., vol. 80, pp. 648-662, Dec. 2017, Available: https://doi.org/10.1016/j.rser.2017.05.289.

[28] F. Blaabjerg, R. Teodorescu, M. Liserre and A.V. Timbus, “Overview of control and grid synchronization for distributed power generation systems,” *IEEE Trans. on Ind. Electron.*, vol. 53, no. 5, pp. 1398-1409, Oct. 2006, Available: DOI: 10.1109/TIE.2006.881997.

[29] D.F. Zhou, M. Izumi, M. Miki, B. Felder, T. Ida and M. Kitano, “An overview of rotating machine systems with high-temperature bulk superconductors,” *Supercond. Sci. and Technol.*, vol. 25, no. 10, pp. 103001 (12pp), Aug. 2012, Available: doi:10.1088/0953-2048/25/10/103001.

[30] G. Klaus, M. Wilke, J. Frauenhofer, W. Nick and H. W. Neumuller, “Design challenges and benefits of HTS synchronous machines,” Presented at Power Engineering Society General Meeting, July 2007, Available: DOI: 10.1109/PES.2007.385756.

[31] S. Fujita, M. Daibo, T. Takeuchi, N. Nakamura, R. Suzuki, Y. Iijima, M. Itoh and T. Saitoh, “Evaluation of Rare-earth-based Coated Conductors,” *J. Cryo. Super. Soc. Jpn*. vol. 48, no. 4, pp. 172-177, 2013, Available: http://doi.org/10.2221/jcsj.48.172.

[32] Y. Xu, N. Maki and M. Izumi, (2015, Apr.) “Study of Key Parameters and cryogenic vessel structure of 10-MW Salient-pole Wind Turbine HTS Generator,” *IEEE Trans. Appl. Supercond.*, vol. 25, no. 2, pp. 5200406 (6), Apr. 2015, Available: DOI: 10.1109/TASC.2014.2368118.

[33] Y. Koshiba, S. Yuan, N. Maki, M. Izumi, K. Umemoto, K. Aizawa, Y. Kimura and M. Yokoyama, “Critical Current and Electric Loss Under Magnetic Field at 30 K on Bi-2223 Superconducting Coil for Ship Propulsion Motor,” *IEEE Trans. Appl. Supercond.*, vol. 21, no. 3, pp. 1127-1130, Feb., 2011, Available: DOI: 10.1109/TASC.2011.2106750.

CHAPTER V

Electrical design of 1 MW PM salient-pole marine current turbine generator

In this chapter, a conceptual structure of 1 MW marine current turbine generator (MCTG) using permanent magnets (PM) as field poles is proposed. The design and optimization procedures, models and specifications of the generator part are studied. The design starts from analytical equations and then is optimized based on 3D FEM simulation, where good agreements are achieved finally. Meanwhile, the influence of number of poles and the confinement of outer diameter, etc., on the generator performance are clarified. 66 has been adopt for the optimum number of poles when the outer diameter is confined to 4 m. It is found multi-pole synchronous generator with PM field pole can provide a promising solution for the future MCTG. Since the HTS bulks can supply magnitude higher magnetic flux density than PM, it is attractive to start the design of HTS generator using bulks. At this stage, a key machine structure concerning the *in-situ* magnetization is proposed integrated with the off-axis magnetization geometry.

5.1 Conceptual structure of PM salient-pole generator

A new concept structure for MCTG is proposed and the design and optimization method for the generator module is explained as shown in Figs. 5-1 and 5-8. The rotor is directly driven by the turbine blades and the stator is fixed to a stationary support structure. Notably, the generator is set in the inner side of the blade. Hence, significant reduction of generator weight and size can be expected compared with rim-driven technology.

With rated output power of 1 MW, a thorough analysis is conducted based on the variations of key generator parameters related to the electromagnetism characteristics. The main dimension parameters, including pole numbers, PM thickness are discussed in details. Based on the design results, it can be concluded that the proposed generator is promising for future MCTGs.

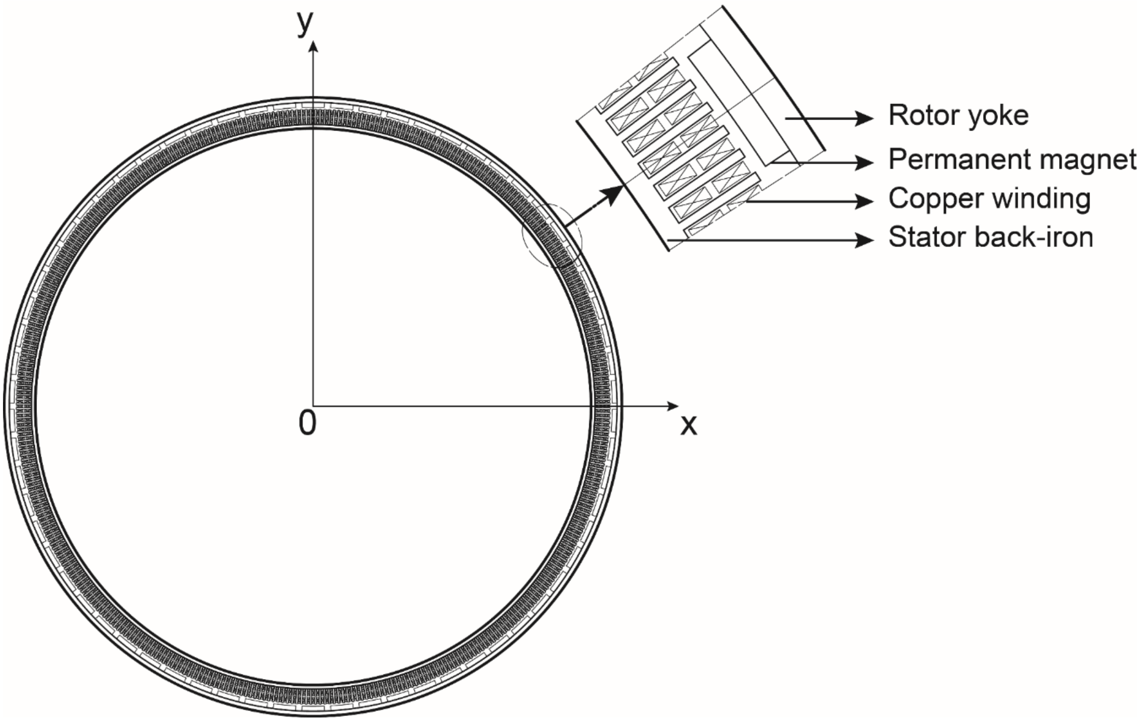

Figure 5-1. Schematic model the proposed MCTG. The expanded view shows the structure of single magnetic field, where the rotor is directly connected with the blades and the stator part is fixed to the stationary support structure.

5.2 Working conditions of marine current turbine generator

Integrated with the marine current characteristics, the working conditions are decided as following, where the calculation method is explained in Chapter IV:

Table 5-1 DESIGN CONDITIONS OF 1 MW 3-PHASE MCTG

Output power (kW)	1000
Rated current speed (m/s)	2.5
Rated speed of turbine blade (RPM)	16
Turbine outer diameters (m)	18
Outer diameter (m)	4 ± 0.1
Terminal voltage (V)	660
Power factor	1

5.3 Design and optimization of electromagnetic model

In this section, the design method of electromagnetic models for PM and HTS generators are introduced step by step and summarized in Fig. 5-6. Next, the optimization process and post-process are described.

Determination of magnetic flux for one field pole

The output power P_0 of a 3-phase synchronous generator can be ideally expressed as $P_0 = 3V_{ph}I_{ph}cos\theta$, where V_{ph}, I_{ph} and $cos\theta$ represents phase voltage, phase current and power factor, respectively. Here, it is assumed the generators run at unity power factor at rated marine current speed to simplify the design and optimization process. The electromotive force induced per phase is given by the equation shown below [1]:

$$V_{ph} = 4.44KfN\Phi_{Armature} \qquad (5-1)$$

where K is the synthetic factor for the generator, including winding factor and magnetic field in air-gap wave form factor, f is the electrical frequency, N is the number of conductors in series per phase and $\Phi_{Armature}$ is the interlinkage of magnetic flux in armature part for one pole, respectively. In equation 5-1, if the V_{ph}, *K*, *f*, *N* are determined, the flux linkage $\Phi_{Armature}$ can be calculated. Under constant flux linkage $\Phi_{Armature}$, the needed Φ_{Field} provided by the field pole is influenced by the flux leakage and depends on the flux leakage coefficient.

To analytically find out the magnetic flux linkage in field pole and air-gap, two leakage coefficients are employed as σ_1 and σ_2. Here, $\sigma_1 = \Phi_{Field}/\Phi_{Armature}$ and $\sigma_2 = \Phi_{Air-gap}/\Phi_{Armature}$, where $\Phi_{Field}$and $\Phi_{Air-gap}$ represents the average flux linkage in field pole and air-gap, respectively. The initial assumed value of leakage coefficient will be defined as $\sigma_{1,0}$ and $\sigma_{2,0}$ and will be modified based on FEM simulations.

Outer diameter confinement of 4m

In this study, the outer diameter of the generator is determined as 4000±100 mm, without degrading the effective sweeping areas of the turbine blades. The outer diameter of air-gap $R_{air-gap}$ is chosen as the starting point, where the Pole pitch τ is expressed as $\pi R_{air-gap} = P\tau$ and the P represents the number of poles. Consequently, the target is to find out the optimum combination of the P and τ.

Assuming suitable magnetic flux density in rotor iron-yoke and stator iron-core, integrated with σ_1 and σ_2, the thickness of the stator iron-core, t_{core}, and rotor iron-yoke t_{yoke} can be deduced.

Hence, the governing equations for radial dimensions are expressed as equation 5-2 for PM-MCTG.

In the PM-MCTG, the rotor is in the outside region, the governing equation is

$$R_{PM} = R_{Air-gap} + 2t_{PM} + 2t_{yoke} \leq 4000 \pm 100 \ \ (mm) \qquad (5-2) \quad .$$

where t_{teeth} and t_{PM} represents the height of iron-tooth and the thickness of PM, respectively. The parameters of iron-tooth and slots will be given in the following part.

Parameters of stator tooth and slots

The two generators topologies both adopt laminated iron-core for stator with conventional two-layer distributed copper windings as shown in Fig. 5-2. The armature windings are not drawn in the slots.

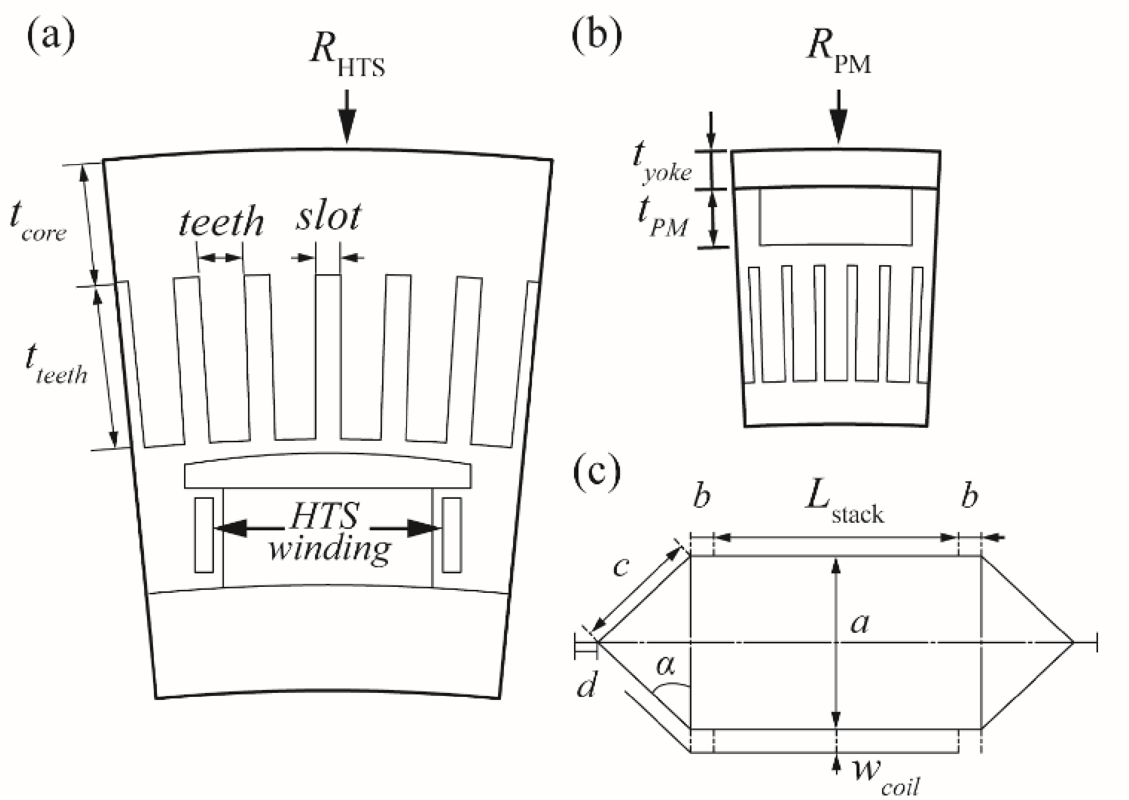

Figure 5-2. Cross section and dimensional parameters of generator rotor and stator for HTS MCTG and PM MCTG. (a). Cross section and corresponding parameters of HTS generator. (b). Cross section and corresponding parameters of PM generator. (c). The structure of armature winding.

In general, the working current density in copper winding will be influenced by the working temperature and cooling efficiency. Here, to make a balance between the copper loss and the usage of copper wires, 3 A/mm^2 is employed. Based on the above parameters and a suitable electric loading of 1000 A/cm, the needed cross-section of armature windings can be calculated. Further, integrated with the insulation materials, the cross-section of teeth and slot can be deduced.

Parameters of copper armature winding

To calculate the armature loss, the total length of the armature windings is necessary. For each turn, it is calculated including the linear part, curve part and the edge shape in the following equations

$$L_{one-turn} = 2L_{stack} + 4b + 4c + 4d \qquad (5-3)$$

$$a = (teeth + slot)\times\left(mN_{pp} - 1\right) \qquad (5-4)$$

$$\sin\alpha = \frac{w_{coil}}{w_{slot} + w_{teeth}} \qquad (5-5)$$

where L_{stack}, a, b, c, d, α are shown in Fig. 5-2 (c). The resistance of armature windings can be also deduced.

According to the geometry parameters of armature windings and particular known parameters, the leakage reactance can be calculated. Further, the armature reaction reactance under load-condition is estimated.

Magnetomotive force under no-load and load condition

With the above determined parameters, the required *MMF* for stator iron-core, stator teeth, air-region and rotor is calculated considering the *B-H* characteristic of laminated iron-core materials under no-load condition.

Also, the armature reaction is introduced to compensate the required MMF under load condition. The interlinkage of $\Phi_{Armature}$ under load condition and no-load condition is emphasized for the further comparison with the FEM simulation results.

Field pole parameters

To supply the required *MMF*, PM magnet pole are adopted. The parameters are described focusing on the operating condition of PM materials. To make the comparisons fair, the PM width/pole pitch for all the PM MCTG models employ a same value of 0.73. Therefore, the influence of pole arc to pole pitch ratio is not analyzed in this paper.

In the PM MCTG, Nd-Fe-B magnets (HS-40AH, Hitach Metal Co., Ltd.) are adopted, with a residual magnetic flux density B_r of 1.22T and coercive force H_c of 895 kA/m at 50°C. The thickness of Nd-Fe-B magnet is a key parameter which influences the generator efficiency, cost and weight. Here, PM MCTGs with varied PM thickness from 20 mm to 60 mm are studied and compared.

To determine the operating point of PMs with different thickness, the calculated MMF under load condition is employed to calculate the *B-H* values of the PM materials. Consequently, the operating point of PM, B_{op}, can be obtained from the intersections of the H_c of 895 kA/m and the demagnetization line as shown in Fig. 5-3.

It is found that thicker PM can sustain higher B_{op}, which is promising to make the generator compact and efficient. From the respect of economic cost, the choose of PM should achieve a balance between the thickness and amount of PM.

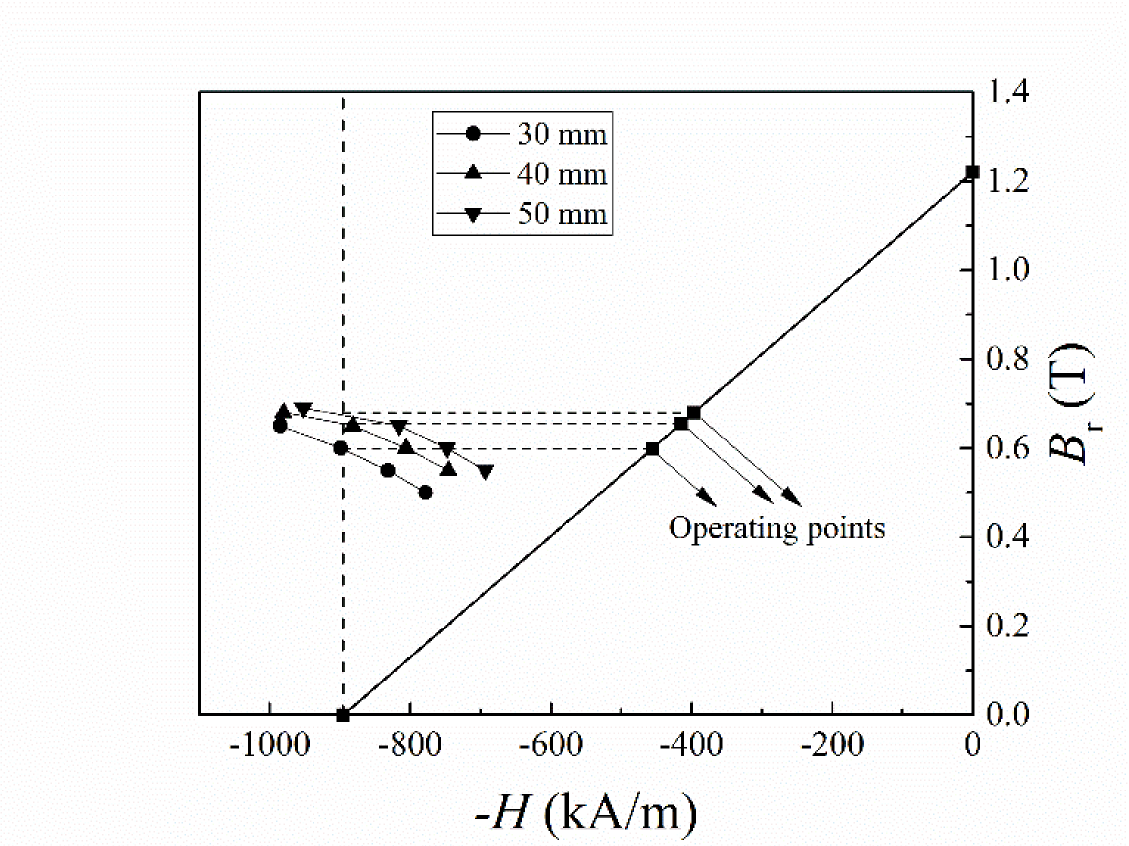

Figure 5-3. Operating point determination of Nd-Fe-B magnet (HS-40AH, Hitach Metal Co., Ltd.) with varied thickness of 30, 40, 50 mm.

Generator weight, loss and efficiency

Following the determined parameters, the weight of each part of the generator can be calculated. Also, loss of generator is also estimated including the iron loss, armature resistance loss, stray loss, mechanical loss, and the cooling loss. Thus, the total loss and efficiency of PM MCTG can be obtained.

Determination of machines parameters

Based on the above analytical analysis, the preliminary parameter scanning can be finished and the best individual are selected for the following FEM optimization as shown in Fig. 5-6. The results of PM MCTG are shown in Figs. 5-4 and 5-5.

For PM MCTG in Fig. 5-4, it is found the efficiency increasing sharply in the range between 20 mm to 30 mm and gradually reaches a saturation over 40 mm. Also, the usage of PM materials increases in the whole range from 20 mm to 60 mm. To make a balance between efficiency and PM weight, 30 mm is chosen as the optimum thickness for the present study.

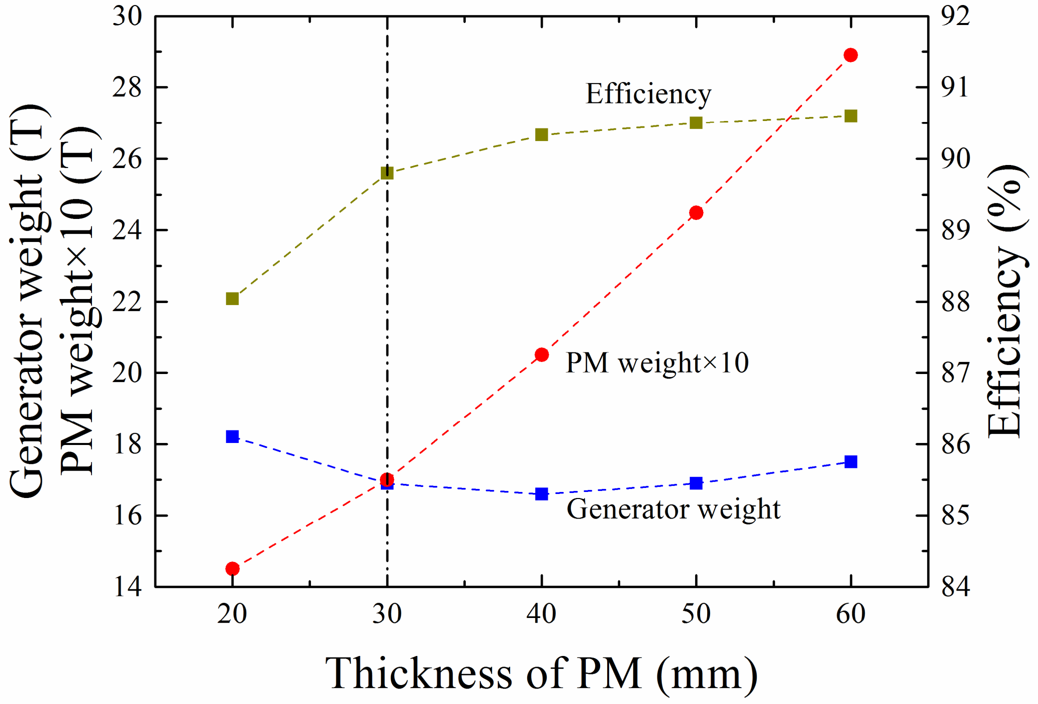

Figure 5-4. Generator weight, efficiency, PM weight as a function of the PM thickness from 20mm to 60 mm.

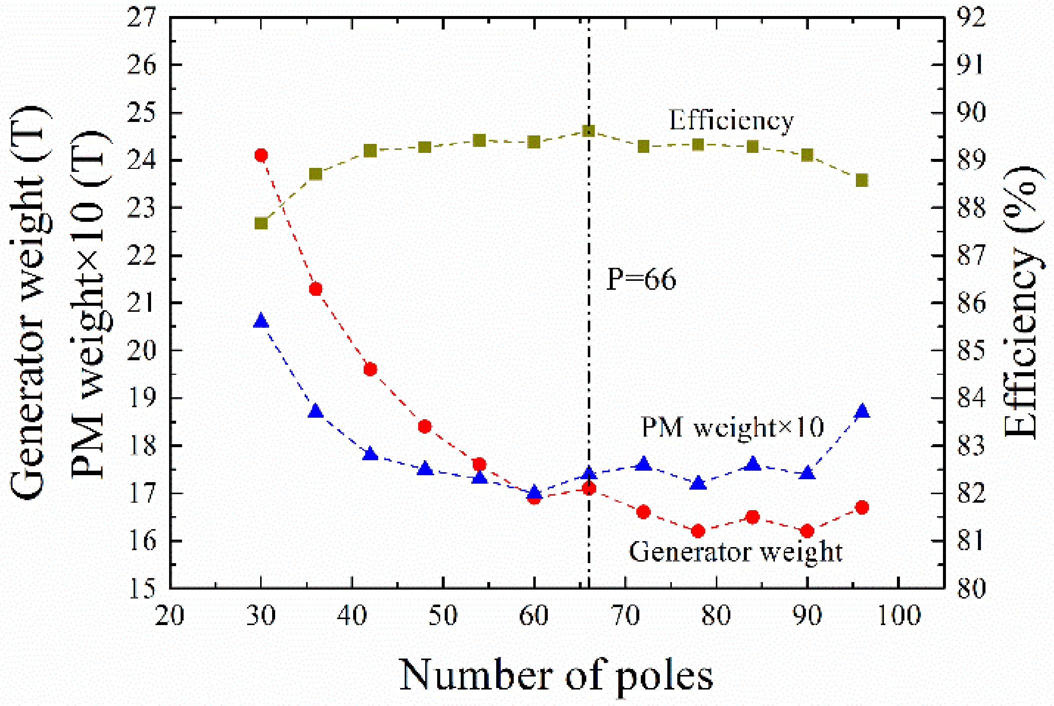

Figure 5-5. Generator weight, efficiency, PM weight as a function of the number of poles.

It can be seen from the Fig. 6-5, as the increase of number of poles, the generator weight decreases in the beginning and stabilizes gradually. It is because with increasing of number of poles, the pole pitch is reduced and the magnetic circuit for each field pole pair is shorten. Consequently, the usage of iron materials is reduced and the magnetic flux is mainly confined within the iron-core. Meanwhile, the PM weight decreases in the beginning and re-increase gradually after P is larger than 60. Combing with the efficiency, 66 is considered as the candidate for the following optimization.

Modeling and simulation of single magnetic pole

Till now, the best candidates among two generator topologies for further optimization can be decided. The geometrical parameters for the 3D modeling are listed in Table III.
Optimization
In the optimization process, a commercial software of MagNet 7.4.1 (Infolytica Inc.) is utilized to calculate the spatial magnetic flux distribution. Through simulation, the magnetic flux vector B_x, B_y and B_z as shown in Figs. 6-7, which represents the magnetic flux density in x, y and z direction, can be obtained and are used to calculate the flux leakage coefficient.

Table 5-2 Basic Parameters and Operation Characteristics of 1-MW-Class PM MCTGs

Physical Dimensions and Design Parameters	PM Type (30 mm)
Number of poles	66
Initial leakage coefficient $\sigma_{1,0}$	1.44
Initial leakage coefficient $\sigma_{2,0}$	1.26
Outer diameter [mm]	3924
Inner diameter [mm]	3525
Generator effective axial length [mm]	812

As shown in Fig. 5-6, the main function of the FEM is to determine the accurate leakage coefficient σ. Then the calculated σ is utilized to modify the design values.

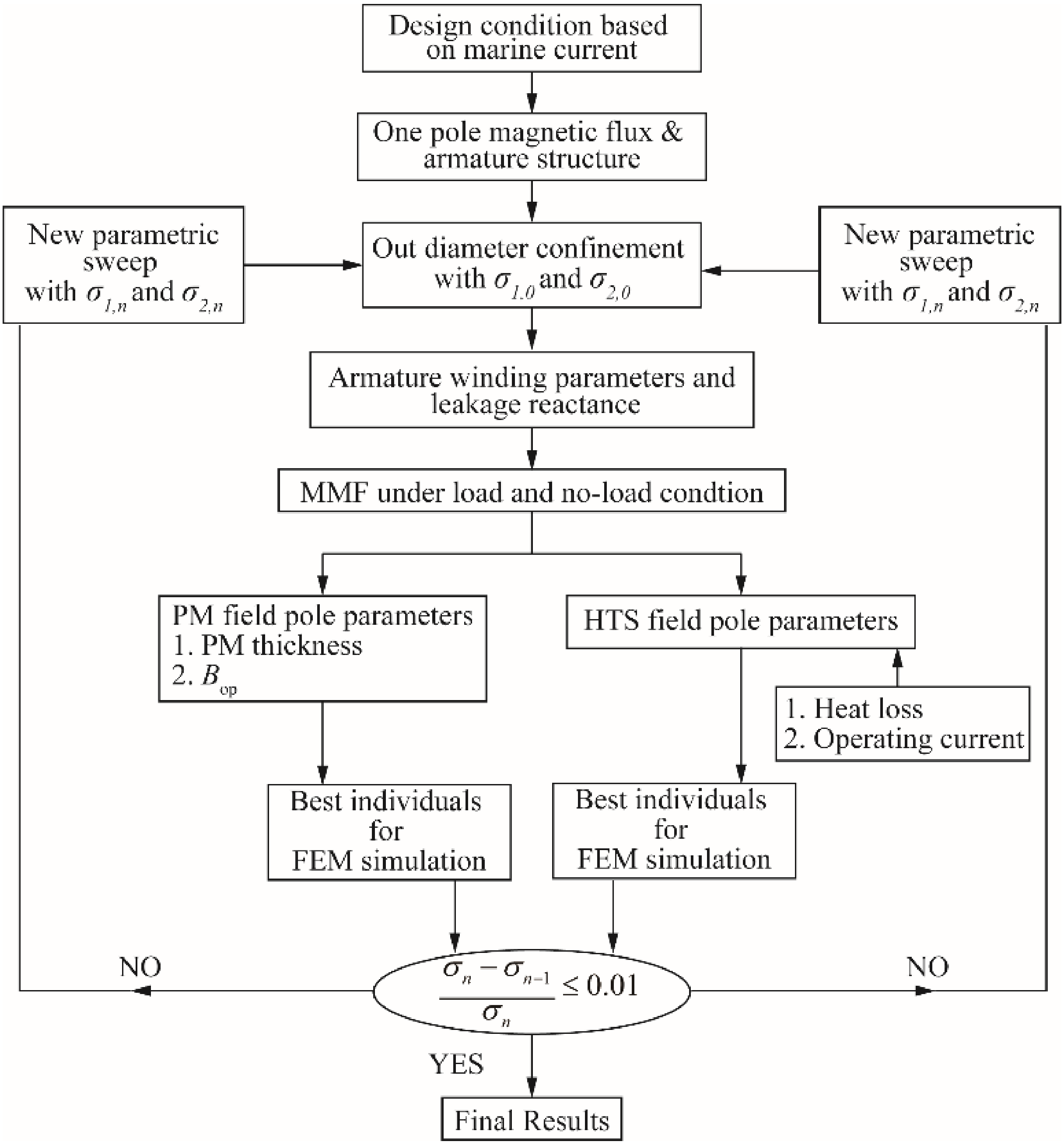

Figure 5-6. Design and optimization flow chart for the MCTG generator with PM and HTS magnetic field poles.

Determination of single magnetic pole

In the simulation, the *B*-*H* curve of the laminated iron material are the same with [2]. The generators are modelled in steady states under no-load condition to get the optimum geometries. Two critical conditions are defined as teeth center condition and slot center condition, where the centerline of one teeth and one slot coincides with the centerline of the corresponding field pole along the radially direction, respectively. The average value of calculated σ under slot center case and teeth center case were chosen as the calculated leakage coefficient.

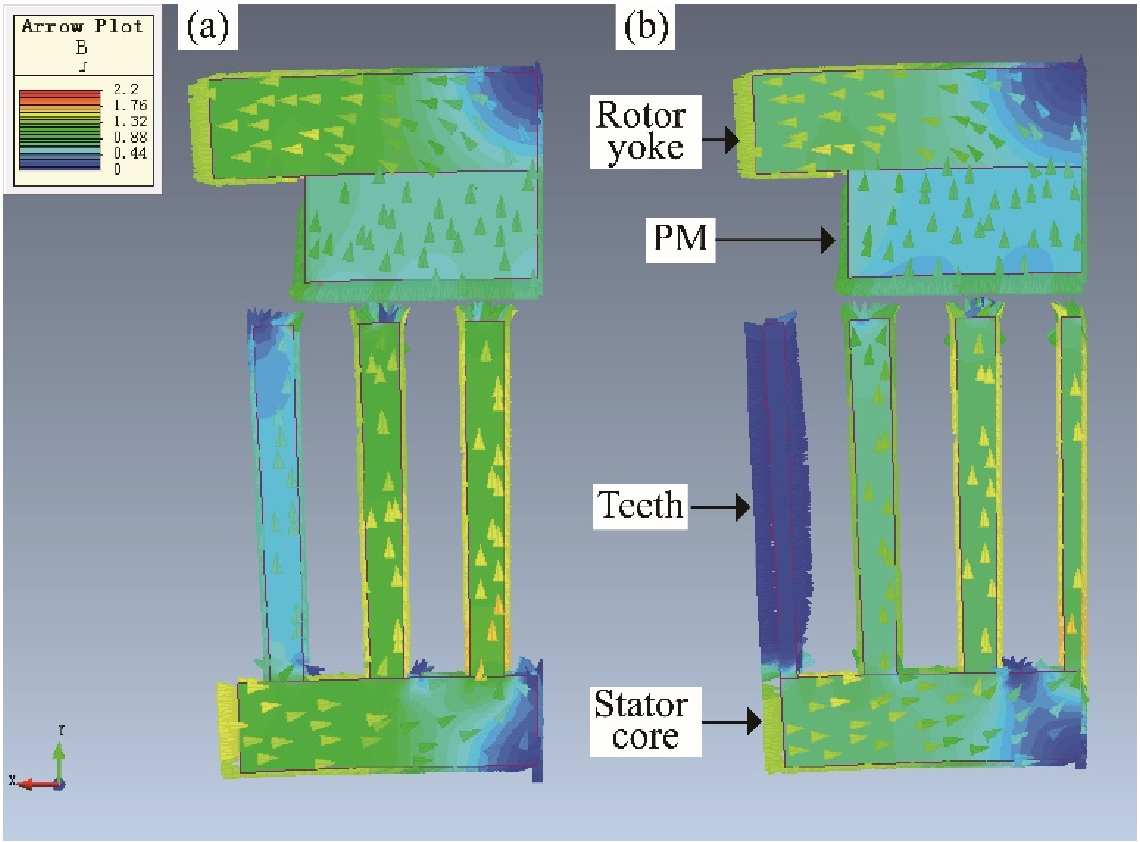

Figure 5-7. Magnetic flux distribution in the cross section of the proposed PM-MCTG (Half-model of one magnetic pole). (a) The steady case of slot center case. (b) The steady case of teeth center case.

5.4 Design results of PM generator

The proposed PM topologies are verified to be feasible for MCTGs. The final design results for PM MCTGs are listed in Table 5-3. From the view of electromagnetic design, it can be concluded that the multi-pole ring-type MCTG is also feasible.

Both HTS and PM topologies provide promising solution for future 1 MW marine current turbine generators. Combing the design results in Chapters IV and V, it can be mainly summarized as the following:

- Due to the limitation of magnetic flux saturation of PM materials, larger number of poles are needed to satisfy the output power such as 1 MW in this study. 66 and 32 are chosen for PM MCTG and HTS MCTG, respectively.
- HTS topology shows several advantages over PM topology. One aspect comes from the efficiency, HTS topology is over 2% higher compared with PM MCTG. Referring to the weight of generator module, HTS topology is lighter compared with PM MCTG.

- At the rated output power of 1 MW, HTS and PM topologies are both promising for the future MCTG.

Table 5-3 GENERATOR PARAMETERS FOR PM MCTG

Final design results	PM MCTG
Number of poles	66
Pole pitch	181
Mean air gap length [mm]	12
Outer diameter of generator (R_o)	3917
Inner diameter of generator (R_i)	3493
Generator effective axial length (L) [mm]	902
No-load MMF/Field pole [kA/Field pole]	19.8
Load MMM/Field pole [kA/Field pole]	26.8
Rotor weight [t]	4.9
Armature loss [kW]	91.9
Iron loss [kW]	7.2
Total loss [kW]	115.9
Efficiency [%]	89.6
Weight [t]	17.1

Generally, HTS bulk magnet is made of high density HTS materials and can work as more intensified field pole than HTS field windings and PM in limited space. To further improve the efficiency and reduce the generator dimension, air-core HTS generator with HTS bulk magnets is required. Based on the present study, the magnetization geometry is outlined here. As shown in Fig. 5-2 (b) and Table 5-4, the dimensions for the magnetic pole of 1 MW PM generator is listed as a reference. From the study in Chapters II, it is found that disk-shaped HTS bulks show significant trapped flux performance compared with the cubic shape bulks regarding to the $B_{\max}\cos\theta$ relationship. Thus, the disk-shaped HTS bulks is preferred for further HTS machine design. Normally, due to the quench melt growth characteristics, two types of bulks size 60 mm in diameter and 20 in thickness and 45 mm in diameter and 15 in thickness are popular used. Consequently, these two size bulks are employed for the initial magnetization geometry design as shown in Figs. 5-8 and 5-9.

Table 5-4 Dimensions of PM field pole for 1 MW MCTG

Physical Dimensions	PM Type (30 mm)
Pole pitch	181
PM width	132
Outer diameter [mm]	3924
Inner diameter [mm]	3525
Generator effective axial length [mm]	812

As seen from Table 5-4, the PM width is 132 mm which can be satisfied with two rows of Φ 60 mm bulks or three rows of Φ 45 mm bulks as shown in Figs. 5-8 and 5-9. In generator/motor applications, the working points of permanent magnets are degraded by armature reaction. As calculated in Chapter V, the working point of magnet material is only at 0.65 T level. When it comes to the HTS bulks, 17.6 T at 29 K and 3 T at liquid N_2 have been achieved, which is much higher and can lead to improved power density and weight density dramatically. More important, the trapped flux performance is rarely influenced by armature reaction at low frequency to our knowledge.

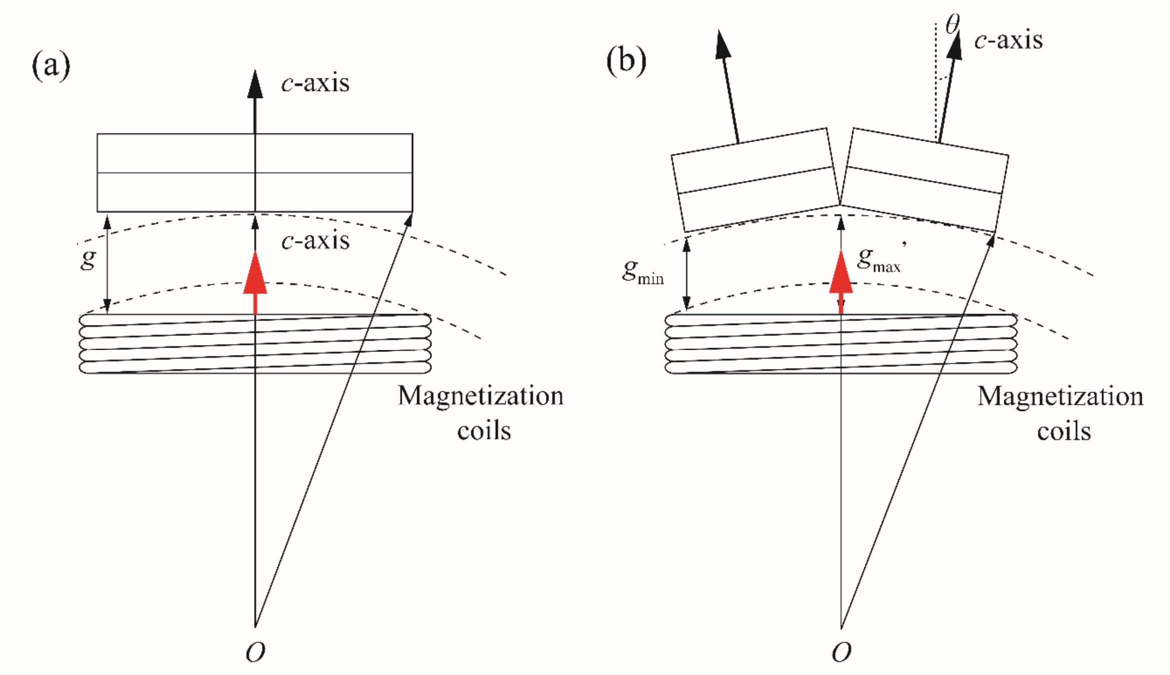

Figure 5-8. Concept design of on-axis and off-axis arrangement of HTS bulks with 60 mm diameters of 1 MW marine current turbine generator. (a) The magnetization field generated by the magnetization coils is parallel to the crystallographic *c*-axis. (b) Off-axis magnetization field can be applied with respect to the crystallographic *c*-axis, which can lead to an enhancement of magnetic flux density in air gap region.

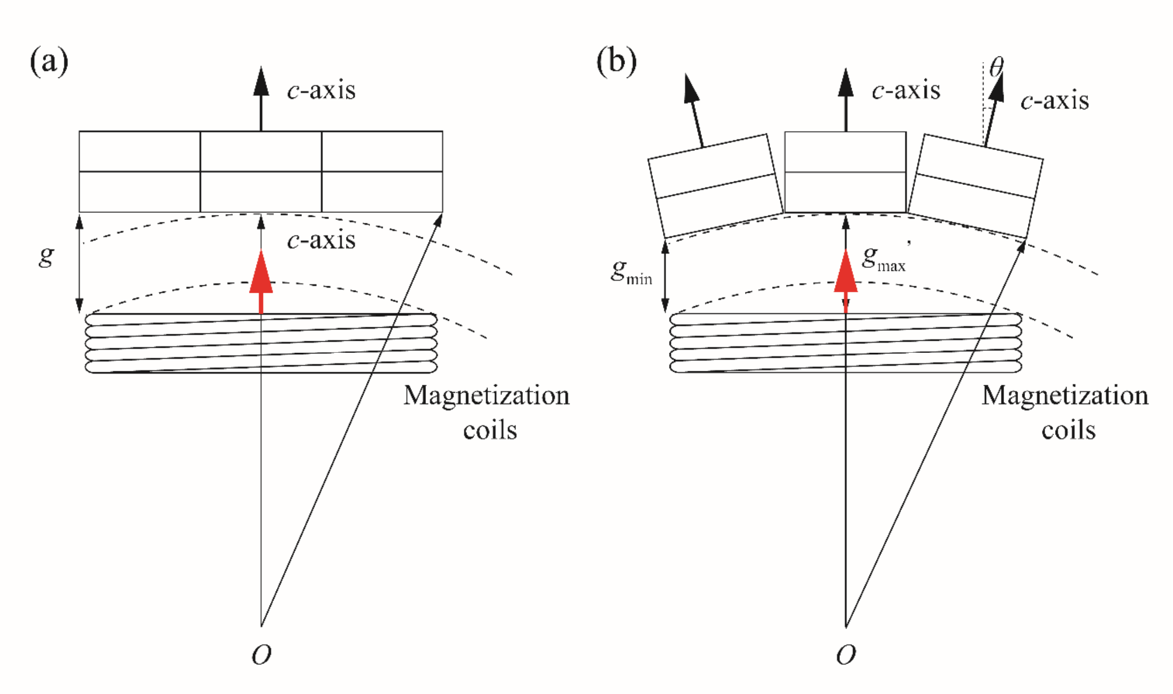

Figure 5-9. Concept design of on-axis and off-axis arrangement of HTS bulks with 45 mm diameters of 1 MW marine current turbine generator. (a) The magnetization field generated by the magnetization coils is parallel to the crystallographic *c*-axis. (b) Off-axis magnetization field can be applied with respect to the crystallographic *c*-axis, which can lead to an enhancement of magnetic flux density in air gap region.

5.5 Conclusions

In this chapter, the electromagnetic design and optimization of 1 MW MCTG using PM materials were studied. The proposed design models were presented and the generator characteristics were studied based on analytical method and then optimized with FEM simulation. Meanwhile, with high efficiency, such type generators can provide a promising solution for the future MCTGs. 66 have been adopt for the optimum number of poles when the outer diameter is confined to 4 m. Huge reduction in weight compared with MCT is attractive. For next step, considering the superior trapped magnetic flux performance 17.6 T at 26 K and 3 T at 77K, the forthcoming prototype HTS MCTG with HTS bulks as field poles is regarded as a better choice for the future marine current turbine generator.

References

[1] A. McDonald and N. A. Bhuiyan, “On the optimization of generators for offshore direct drive wind turbines,” *IEEE Trans. on Energy Convers*., vol. 32, no. 1, pp. 348-358, Mar. 2017, Available: DOI: 10.1109/TEC.2016.2624219.

[2] Y. Xu, N. Maki and M. Izumi, (2015, Apr.) “Study of Key Parameters and cryogenic vessel structure of 10-MW Salient-pole Wind Turbine HTS Generator,” *IEEE Trans. Appl. Supercond.*, vol. 25, no. 2, pp. 5200406 (6), Apr. 2015, Available: DOI: 10.1109/TASC.2014.2368118.

CHAPTER VI

Conclusions and future work

This dissertation focus on the improvement and design of HTS machines. From one aspect, off-axis field cooled magnetization is proposed and the trapped flux performance is confirmed which makes it possible to immediately employ off-axis magnetization geometry besides the on-axis magnetization geometry as shown in Fig. 2-14. Meanwhile, the feasibility of employing HTS technology into marine current turbine generator is also investigated. In this chapter, an overall summary is given and the future work of employing off-axis magnetization geometry into generator design is outlined.

6.1 Conclusions

Nowadays, HTS electrical machines using field poles with BSCCO/1G or REBCO/2G wires are more developed than those using HTS bulks. Thus, researches on HTS bulks are in highly demand to support the design and manufacture of electric machines in power applications. HTS bulks are continuous medium of superconductors and can provide potentially higher flux density than HTS coils with the same dimension. In this dissertation, the trapped flux behavior under off-axis FCM for HTS bulk superconductor GdBCO is experimentally investigated and the trapped flux distribution using 2D scanning by Hall sensor and 3D viewer with steel wires at liquid N_2 temperature is also conducted. With the inclination angle increases up to 30° - 45°, the sample provides superior trapped flux component parallel to the *c*-axis comparable with those obtained by the on-axis FCM. As well, the magnetization after FCM is almost parallel to the applied external field B_{app}. For large inclination angle, trapped flux lines are meaningful to understand the pinning behaviour of bulk materials in which the trapped flux behaviour is a collection of anisotropic flux pinning and the effect of microstructure on the deformed circulation of supercurrent.

Generally, there is no simple scaling law can successfully describe the trapped flux behaviour in $REBa_2Cu_3O_{7-\delta}$ under off-axis magnetization. However, the obtained results appear to support that $REBa_2Cu_3O_{7-\delta}$ can sustain sufficient trapped flux performance under finite off-axis angle. For engineering applications, the off-axis FCM may open up the possibility of future designs with *in-situ* magnetization systems in HTS electric machines as shown in Fig. 2-14.

As for the marine current turbine generators, the proposed two generator topologies were verified to be feasible. The present study for HTS and PM MCTGs can be summarized as following:

(1) A conceptual structure of a 1 MW salient-pole MCTG with race-track-shaped HTS field coils was proposed, and a novel electrical design algorithm is also proposed for the MCTG. The electrical design method derivation was explained step by step in chapter V. The influence of some main machine parameters, e.g. pole pitch, stator outer diameter, magnetic flux density in the stator teeth, and electric loading, on HTS generator performance were clarified, and the optimal parameters are determined.

(2) A conceptual structure of a 1 MW salient-pole MCTG with PM field poles was proposed, and a novel electrical design algorithm is proposed for the MCTG. The electrical design method derivation was explained step by step in chapter VI. The influence of some main machine parameters, e.g. pole pitch, stator outer diameter, magnetic flux density in the stator teeth, and electric loading, on PM generator performance were clarified, and the optimal parameters are determined.

(3) For the comparison of 1 MW HTS and PM MCTG, the main generator parameters are studied and compared. Due to the limitation of magnetic flux saturation of PM materials, larger number of poles are needed to satisfy the output power such as 1 MW in this study. 66 and 32 are chosen for PM MCTG and HTS MCTG, respectively. HTS topology shows several advantages over PM topology. One aspect comes from the efficiency, HTS topology is over 2% higher compared with PM MCTG. Referring to the weight of generator module, HTS topology is lighter compared with PM MCTG.

Following the design study of HTS and PM marine current turbine generators, the employment of HTS field poles has shown enhancement of efficiency and reducing weight, i.e. higher output density. Near future stage of intensive design studies of marine current turbine with HTS bulks is expected and the forthcoming prototype is regarded as a better choice for the future marine current turbine generator.

6.2 Future Work

The inclined bundle trapped vortex is one manifestation of the complex behaviour of the trapped flux in GdBCO under off-axis field cooled magnetization. In contrast to higher anisotropic materials, such as $Bi_2Sr_2CaCu_2O_8$, the angularly dependence of trapped flux performance is difficult to quantitatively model. One prerequisite to further work in this field is further study of the growth of GdBCO bulks. The experimental evidence discussed in the thesis show that the trapped flux behavior does not show obvious anisotropic characteristics as the materials itself. In the string/pancake regime the vortex strings are more weakly pinned, the evidence suggests that this is not the case when a high off-axis angle is present. In this dissertation, it has been assumed that, at the relatively large fields used, the microscopic direction of the flux lines is near parallel to the applied field. As has been discussed in chapter II. It would therefore be interesting to investigate whether the trapped flux behavior seen in this thesis, also exits in sphere GdBCO samples. Meanwhile, for pulse magnetization, off-axis geometry would be interesting to investigate the trapped flux behavior, where large local heat generation may influence the bundle flux vortex structure.

For the engineering applications, the present off-axis magnetization geometry is feasible to be adopt in HTS application design. To expand the variation of HTS applications using REBCO bulks, relatively study would be urgently required.

For next step design using HTS bulks, the major modification of electromagnetism design method focus on the utilization of air-core for stator and armature parts. When iron materials are employed, the magnetic flux is mainly confined in iron teeth and iron field pole. Hence, the magnetic flux distribution is treated as one-dimensional problem in the present calculation method. If non-magnetic material is used due to the high magnetic flux density provided by HTS bulks, magnetic flux distribution in armature region should be considered as two-dimensional problem, which will influence the induced voltage.

Also, the cooling structure for the HTS MCTG for the HTS field winding should be carefully considered, especially for such marine applications.

Cost comparison should be conducted for the future manufacture of MCTGs with HTS and PM field poles.

Acknowledgements

During the past three years of my Ph.D. study, there are lots of people who have contributed, either directly or indirectly, to build my academic career. Sincerely, I am extremely thankful for their contributions.

My acknowledgments must, naturally, start with expressing my profound thanks to my supervisor Professor Izumi Mitsuru. Four years ago, I registered his lecture, Advanced Materials, and everything just happened so suddenly for me to determine to follow him in my Ph.D. course. Without his guidance, good humor and vision, the present work would not exist. I am grateful for having had the opportunity to work under his leading in such a world-class research group with full of edging-technologies.

When I started my study in applied physics laboratory here, Professor Izumi and Dr. Miki introduced me to the experimental techniques required and helped considerably with my understanding of all things high temperature superconductivity related. Their passion, most importantly, stoicisms in the face of experimental adversity proved invaluable.

Dr. Zhou Di-fan recommended me to this lab and gave me tremendous advice when I felt mixed-up. Although he is no longer a member of the group, I owe a significant debt to him, both for his attention to details and willingness to provide technical discussions on the occasions when all seemed lost. Within the group, I would like to thank Professor Ida Tetsuya, Maki Naoki, Xu Yuan-yuan, Erasmus Shaanika, Jing Hai-lian, Matsuumi Ryo, Yamaguchi Kota and Tsubochi for their support and welcoming me into this group.

Outside our group, I owe a significant debt to the Dr. Mitsuru Morita for providing high quality QMG samples. Without the high-quality samples, all the experiments and analysis cannot exist.

Besides, I also owe a significant debt of gratitude to my beloved family. Thank you for my sister Li Miao to accompany with our parents during my past absent. Last but not least, I am grateful to my parents for their indulgence and unstinting support over the past three expensive years!

List of publications

- **LI Zhi**, Ida Tetsuya, Miki Motohiro and Izumi Mitsuru, “Significant flux trapping in single grain GdBCO bulk superconductor under off-axis field cooled magnetization,” *Superconductor Science and Technology*, 30, 035019 (8pp), 2017.
- **LI Zhi**, Ida Tetsuya, Miki Motohiro and Izumi Mitsuru, “Trapped Flux Behavior in Melt-Growth GdBCO Bulk Superconductor Under Off-Axis Field Cooled Magnetization,” *IEEE Transactions on Applied Superconductivity*, 27, 6800604 (4pp), 2016.
- Ida Tetsuya, **Li Zhi**, Zhou Difan, Miki Motoshiro, Zhang Yufeng, and Izumi Mitsuru, “Materials preparation and magnetization of Gd-Ba-Cu-O bulk high-temperature superconductors,” *Superconductor Science and Technology*, 29, 054005 (8pp), 2015.
- Liu Y., Pan B., **Li Z.**, Xiang H., Qian J., Du G., Huang S., Yao X., Izumi M. and Wang Y., “$YBa_2Cu_3O_{7-\delta}$ superconductor bulks composited by Y_2BaCuO_5 nanoparticles derived from homogeneous nucleation catastrophe,” *Journal of the American Ceramic Society*, 100, 3858-3864, 2017.
- **Li Zhi**, Maki Naoki, Tetsuya Ida and Mitsuru Izumi, “Design of 1MW Synchronous Marine current turbine generator within Confined Space,” (Under Review).
- **Li Zhi**, Maki Naoki, Ida Tetsuya, Miki Motohiro and Mitsuru Izumi, “Comparative study of 1 MW PM and HTS synchronous generators for marine current turbine,” EUCAS 2017, (Poster accepted).
- Ida Tetsuya, **Li Zhi**, Miki Motohiro, Watasaki Masahiro and Mitsuru Izumi, “Waveform control pulse magnetization for HTS bulk with flux jump,” EUCAS 2017, (Poster accepted).